Title
Deterministic Control of Individual Nanomagnets in Strain-mediated Multiferroic Heterostructures

Author
Cui, Jizhai

Publication Date
2016

Peer reviewed|Thesis/dissertation

UNIVERSITY OF CALIFORNIA

Los Angeles

Deterministic Control of Individual Nanomagnets in Strain-mediated Multiferroic Heterostructures

A dissertation submitted in partial satisfaction of the

requirement of the degree Doctor of Philosophy

in Mechanical Engineering

by

Jizhai Cui

2016

ABSTRACT OF THE DISSERTATION

Deterministic Control of Individual Nanomagnets

in Strain-mediated Multiferroic Heterostructures

by

Jizhai Cui

Doctor of Philosophy in Mechanical Engineering

University of California, Los Angeles, 2016

Professor Christopher S. Lynch, Chair

Controlling magnetism on the nanoscale has attracted considerable research interest for the high potential in non-volatile memory and logic applications. Using strain to control magnetization in strain-mediated multiferroic heterostructures is considered the most energy efficient approach, reducing energy dissipation by orders of magnitude. The strain-mediated multiferroic heterostructure has a ferromagnetic element on a ferroelectric substrate. Applying voltage to the ferroelectric substrate induces piezoelectric strain, which manipulates the magnetization of the ferromagnetic element through magnetoelastic effect. Nanomagnets, as information storage bits for non-volatile memory applications, need to be both individually and deterministically controlled. In the present work, two concepts are developed for this aim, one uses an electrode pattern design on a piezoelectric substrate to produce localized strain, and the other consists of architecting the shape of nanomagnets to take advantage of magnetic shape

anisotropy. Patterned electrodes are designed and their effect is modeled using finite element simulations. By selectively applying voltage to electrode pairs, various strain configurations are produced between the electrodes, creating localized strain that controls individual nanomagnets. The modeling results were confirmed by experiments that used magnetization characterization techniques including magneto-optical Kerr effect (MOKE) and magnetic force microscopy (MFM). By architecting the geometric shape, “peanut” and “cat-eye” shaped nanomagnets were engineered on piezoelectric substrates. These nanomagnets undergo repeated deterministic 180° magnetization rotations in response to individual electric-field-induced strain pulses. The designs were modeled using micromagnetics simulations. Both concepts provide significant contributions for next generation strain-mediated magnetoelectric memory research. This work opens a broad design space for next generation magnetoelectric spintronic devices.

The dissertation of Jizhai Cui is approved.

Gregory P. Carman

Nasr M. Ghoniem

Qibing Pei

Christopher S. Lynch, Committee Chair

University of California, Los Angeles

2016

For my grandfather,

Cui Tianmo

TABLE OF CONTENTS

LIST OF FIGURES

LIST OF TABLES

VITA

Education

2012	M.S., Mechanical Engineering *University of California, Los Angeles*
2011	B.S., Mechanical Engineering *University of Science and Technology Beijing, China*

Employment History

2012-2016	Graduate Student Researcher *University of California, Los Angeles*
2014	Summer Research Internship *Johannes Gutenberg-Universität Mainz, Germany*

Honors and Awards

2016	Best Student Presentation Award Finalist *13th Joint MMM/Intermag Conference at San Diego, CA, USA*
2013	Summer School Travel Grant *ICMR Summer School on Materials in 3D: Modeling and Imaging at Mutiple Length Scales* *University of California, Santa Barbara*

PUBLICATIONS

Jizhai Cui, Scott M. Keller, Cheng-yen Liang, Gregory P. Carman, Christopher S. Lynch, "Nanoscale Magnetic Ratchets Based on Shape Anisotropy", in preparation for publication (2016)

Jizhai Cui, Cheng-Yen Liang, Elizabeth A. Paisley, Abdon Sepulveda, Jon F. Ihlefeld, Gregory P. Carman, Christopher S. Lynch, "Generation of localized strain in a thin film piezoelectric to control individual magnetoelectric heterostructures", Applied Physics Letters, 107, 092903 (2015).

K. Liang, A. Buditama, D. Chien, **J. Cui**, P. L. Cheung, S. Goljahi, S. H. Tolbert, J. P. Chang, C. S. Lynch, "The conductivity mechanism and an improved C−V model of ferroelectric PZT thin film", Journal of Applied Physics, 117, 174107 (2015).

Cheng-Yen Liang, Scott M. Keller, Abdon E. Sepulveda, Wei-Yang Sun, **Jizhai Cui**, Christopher S. Lynch and Gregory P. Carman, "Electrical control of a single magnetoelastic domain structure on a clamped piezoelectric thin film—analysis", Journal of Applied Physics, 116, 123909 (2014).

Jizhai Cui, Joshua L. Hockel, Paul K. Nordeen, David M. Pisani, Gregory P. Carman, Christopher S. Lynch, "Giant electric-field-induced magnetic anisotropy reorientation with patterned electrodes on a Ni thin film/lead zirconate titanate heterostructure", Journal of Applied Physics, 115, 17C711 (2014).

Jizhai Cui, Joshua L. Hockel, Paul K. Nordeen, David M. Pisani, Cheng-yen Liang, Gregory P. Carman, Christopher S. Lynch, "A method to control magnetism in individual strain-mediated magnetoelectric islands", Applied Physics Letters, 103, 232905 (2013).

PRESENTATIONS

Jizhai Cui, Cheng-yen Liang, Elizabeth Paisley, Abdon Sepulveda, Jon Ihlefeld, Greg P. Carman, Christopher S. Lynch, "Controlling Individual Magnetoelectric Heterostructure by Localized Strain in a Thin Film Piezoelectric", 13th Joint MMM-Intermag Conference, January 11-15, 2016, San Diego, California, USA.

Jizhai Cui, Joshua L. Hockel, Paul K. Nordeen, David M. Pisani, Christopher S. Lynch, "Giant electric-field-induced magnetic anisotropy reorientation with patterned electrodes on a Ni thin film/PZT heterostructure", 58th Conference on Magnetism and Magnetic Materials (MMM), November 4-8, 2013, Denver, Colorado, USA.

PATENTS

Christopher S. Lynch, **Jizhai Cui**, Joshua Hockel, Gregory P. Carman, "Devices and Methods for Controlling Magnetic Anisotropy With Localized Biaxial Strain in a Piezoelectric Substrate." U.S. Patent Application Ser. No. 14/740,147

Chapter 1. Introduction

1.1.Motivation

We currently live in the Information Age, a period in human history where the economy is based on computerized information. Information that used to be delivered as a physical media, such as music on vinyl records and photos on photographic paper, are now digitized, stored and processed in electronic devices. Random access memory (RAM) plays a vital role in electronic devices. It is a type of data storage taking the form of integrated circuits. Traditional RAM, like dynamic random access memory (DRAM), stores a bit of information as capacitive charges in a miniaturized circuit with a metal–oxide–semiconductor field-effect transistor (MOSFET) switch and a capacitor. However DRAM is a volatile memory, meaning the information is lost when power is removed. Hence DRAM requires a continuous power supply for information storage. Flash memory improves DRAM design by introducing an oxide layer in the MOSFET that can store electric charge as a type of non-volatile memory. However flash memory is significantly slower in reading and writing a bit of information, compared to DRAM. Both DRAM and flash memory are not energy efficient memory designs. The bit information is stored as electric charge. Reading and writing of the bit information requires electric current that produces heat. This is one of the reasons that a smart phone gets warm after it operates for a while.

Researchers have proposed a type of RAM based on magnetic materials. This magnetic RAM, i.e., MRAM, stores bit information as magnetization. One key advantage of MRAM is that this is a non-volatile memory, because the form of information storage is intrinsic magnetization from magnetic materials. In order to achieve a high feature density, MRAM design requires the ability of controlling magnetism at the nanoscale.

The conventional approach of controlling magnetism is by application of magnetic field. To apply a magnetic field, electric current is required based on Ampere's Law, $\oint_C B \cdot dl = \mu_0 I$ where B is the magnetic field and I is the total current passing through the surface enclosed by C. This technique fails at the nanoscale. An electrical current is required to apply a localized magnetic field. However by decreasing the cross section of a conducting wire, there is a huge increase in resistance $R = \rho \frac{l}{A}$ where A is the cross section area. The use of conducting coils is inefficient in the small scale due to Joule heating.

Magnetization can also be manipulated by spin-polarized current through spin-transfer torque (STT). One memory design based on this method uses a magnetic strip as a "racetrack".[1] In racetrack memory design, magnetic domains act as bits of information for memory and can be "pushed" forward and backward by pumping spin-polarized current through the magnetic strip. Clearly, this technique still involves electric current on the microscopic scale and produces Joule heating. Hence it does not have very good energy efficiency.

In multiferroic material systems, magnetization can be controlled by voltage (instead of current) avoiding resistive heat. Multiferroic material displays more than one ferroic order parameter simultaneously. These can include ferromagnetism, ferroelectricity and ferroelasticity.[2], [3] Single phase multiferroic materials have very low coupling coefficients and usually only exhibit multiferroic properties at cryogenic temperatures. Multiferroic heterostructures have a ferromagnetic layer on a piezoelectric substrate. By applying voltage, or electric field, to this piezoelectric substrate, piezoelectric strain can alter the magnetization of the magnetostrictive ferromagnetic layer. This is called the strain-mediated magnetoelectric (ME) effect. Multiferroic heterostructures attract considerable research interest due to high coupling

coefficient at room temperature and wide range of material choices. Controlling magnetism at the nanoscale using the strain-mediated ME effect also has extraordinary energy efficiency. A comparison between different room temperature non-volatile designs is presented in table 1.1. The strain-mediated magnetoelectric RAM (SME-RAM) has energy consumption several orders of magnitude lower than other non-volatile memory technologies. Magnetic anisotropy determines the degree to which the magnetization has a preferred direction. Previous research has both computationally and experimentally demonstrated that piezoelectric strain can alternate magnetic anisotropy of magnetic thin films and nanomagnets (nanoscale magnetic structures) through the magnetoelastic effect.

Table 1.1. Comparison of room temperature non-volatile memory technologies. (data from [4])

	Flash-NAND	FeRAM	MRAM	STT-RAM	SME-RAM
Storage capacity	>1Gb	>10 Mb	16 Mb*	1Gb†	>>1Gb
Write time	1ms	10 ns	20 ns	3-10 ns	<10 ns
Read time	50 ns	45 ns	10 ns	10 ns	10 ns
Write energy (pJ per bit)	>0.01	0.03	70	0.1	1.6×10^{-4}

Conventional multiferroic heterostructures do not have the ability to control individual nanomagnets. An important work from Buzzi et al [5] demonstrated strain-mediated control of elliptical shaped nanomagnets on a single crystal piezoelectric substrate, as shown in figure 1.1. In this work, all nanomagnets on top electrodes were switched at once by applying a voltage through the thickness of the piezoelectric. This is due to the full top electrode and bottom electrode on either side of the piezoelectric creating uniform strain on the whole substrate. In order to make a memory device, the ability to control individual nanomagnets is needed.

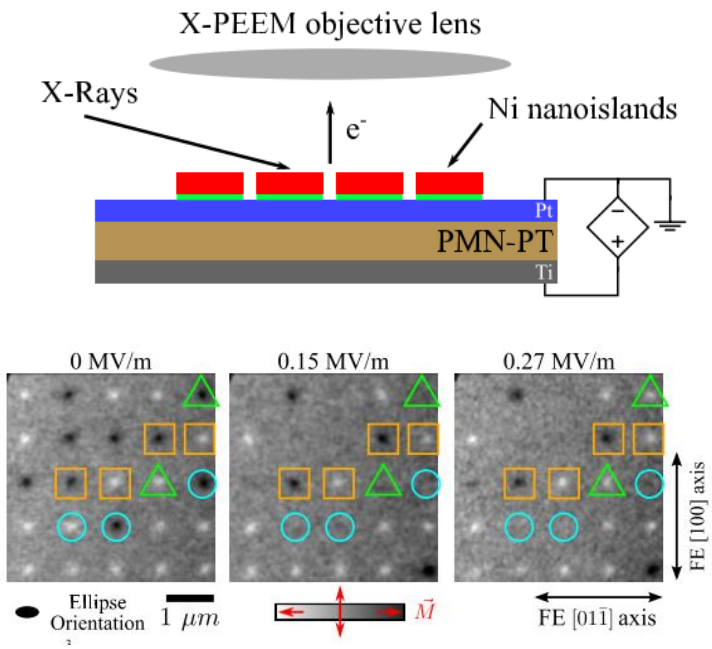

Figure 1.1. Schematic of experiment and photoemission electron microscopy (PEEM) characterization result of Ni nanoislands with application of 0 MV/m, 0.15 MV/m and 0.27 MV/m applied on the PMN-PT substrate. (Figure from [5])

Manipulating magnetization through the strain-mediated ME effect also presents challenges when the goal is to achieve 180° magnetization rotation. Magnetic field, a directional effect, can induce 180° magnetization switching of a single domain nanomagnet when applied opposite to the original magnetization direction. However, strain cannot easily induce such 180° full magnetization switching. Considering solely strain-induced magnetic anisotropy, strain, a uniaxial effect, can induce at most a 90° reorientation of magnetization (a directional vector).[6] Achieving a full 180° magnetization rotation using strain has been considered a "fundamental challenge".[7] For strain-mediated MRAM applications, 180° deterministic magnetization control is required.

In this dissertation, two concepts are presented for deterministic control of individual nanomagnets in strain-mediated multiferroic heterostructures. The concept of patterned

electrodes to produce localized strain on a piezoelectric was developed using multiphysics finite element simulations. This concept enables the ability of controlling individual nanomagnets in multiferroic heterostructures. Experiments on a bulk piezoelectric substrate with Ni thin film were conducted. This showed that by selectively applying voltage on different electrode pairs, localized strain was produced that switched the magnetic easy and hard axes. Further experiments on a lead zirconate titanate (PZT) thin film with a micron-sized Ni ring structure demonstrated deterministic control of the magnetization rotation. Magnetization behavior in response to strain was simulated using a micromagnetics code that coupled the Landau-Lifshitz-Gilbert (LLG) equation with magnetoelastic terms. This work provided the first demonstration of deterministic control of individual nanomagnets on a thin film piezoelectric, and is considered a technical breakthrough.

The second concept presented in this dissertation is architecting the geometric shape of nanomagnets to tailor the magnetic anisotropy. Based on this concept, deterministic 180° control of magnetization by strain is achieved with nanomagnets in properly designed shapes. The geometric shape of nanomagnets influences the magnetization distribution through magnetic shape anisotropy. This effect can be used to create a controllable magnetic domain pattern that dominates the dynamic magnetic response. Prior work on magnetic shape anisotropy focused on nanomagnets with highly symmetric shapes like disks, ellipses, squares and rings, etc. Optimizing the shape of nanomagnets provides an opportunity to significantly improve their functionality. Novel “peanut” and “cat-eye” shaped nanomagnets that undergo repeated deterministic 180° magnetization rotations in response to individual strain pulses were designed on piezoelectric substrates by breaking the symmetry using shape anisotropy. The design principles start from a target device function and proceed to the identification of shapes that

produce the desired function. This approach opens a broad design space for next generation magnetoelectric spintronic devices.

The two concepts developed in this dissertation, the electrode pattern design and the nanomagnet shape design, have the potential to lead to highly efficient strain-mediated magnetoelectric RAM with the ability of achieving individual and deterministic magnetization control.

1.2. Strain-mediate multiferroic heterostructures

In multiferroic materials, magnetoelectric coupling enables controlling magnetism by application of an external electric field, but without an electric current. This will potentially enable increasing the density of computer memories while simultaneously reducing energy dissipation by orders of magnitude. Although single-phase multiferroic materials have been available for many years, the coupling behavior is limited at room temperature; therefore, strain-mediated multiferroic heterostructures with coupled piezoelectric layers and ferromagnetic layers are of interest. A brief review of the history of both single phase multiferroic materials and strain-mediated multiferroic heterostructures shows their increasing technological importance.

A multiferroics material is one that possesses at least two ferroic properties: ferroelectricity, ferromagnetism and ferroelasticity.[3] In multiferroic materials, the coupling interaction between the different order parameters can produce new effects, such as the magnetoelectric effect. Figure 1.2 demonstrates the three ferroic phases of a multiferroic material system and their interactions. The green arrow indicates that in a material system, electric field E can directly control magnetization M while magnetic field H can alternate electric polarization P. This is the magnetoelectric effect. Single phase multiferroics have an intrinsic magnetoelectric effect. Examples that attract considerable research interest are $HoMnO_3$ and $BiFeO_3$.

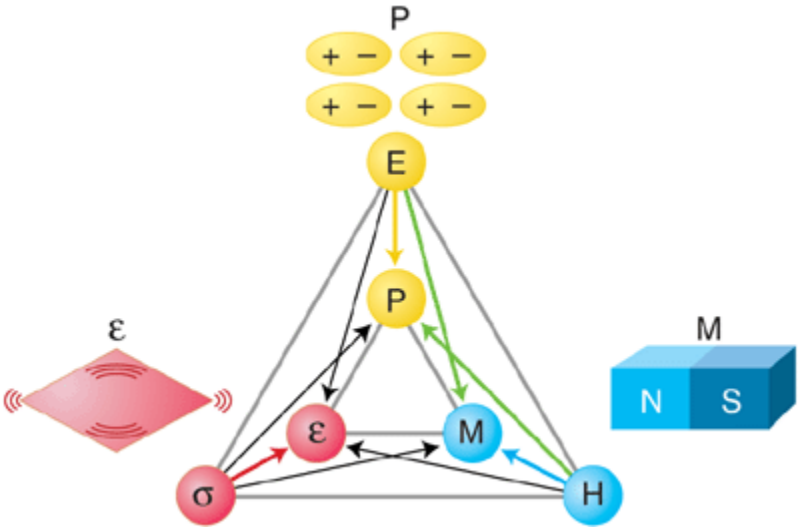

Figure 1.2 Three ferroic phases of a multiferroic material system. In a conventional materials, the electric field E, magnetic field H, and stress σ control the electric polarization P, magnetization M and strain ε, respectively. In a ferroic material, P, M and ε produce ferromagnetism, ferroelectricity, or ferroelasticity, respectively. In a multiferroic, the coexistence of at least two ferroic forms of ordering leads to additional interactions. In a magnetoelectric multiferroic, a magnetic field may control P or an electric field may control M (green arrows). (Figure from [8])

The history of the magnetoelectric effect starts from 1894, when Curie predicted that a body with asymmetric molecular structure might become polarized when placed in a magnetic field and vice versa.[9] However little additional progress was made until 1958 when Landau and Lifshitz proved the possibility of a magnetoelectric effect based on crystal symmetry.[10] Dzyaloshinskii first predicted that magnetoelectric coupling could exist in chromium oxide Cr_2O_3 [11], which was substantially confirmed experimentally by Astrov [12] in the Soviet Union in the 1960s, though the coupling was too small to be of practical significance. Although single-phase magnetoelectric materials have been extensively studied [13]–[16], few natural materials have been observed with an intrinsic magnetoelectric effect, and the coupling strength is usually low at room temperature. Why there are so few magnetic ferroelectric materials? Nicola Hill (now Spaldin) showed that, based on her density functional calculations, the usual

atomic-level mechanisms driving ferromagnetism and ferroelectricity are mutually exclusive.[13] To be specific, the transition metal d-electrons, which are essential for magnetism, reduce the tendency for off-center ferroelectric distortion. Hence, in general, ferroelectricity and ferromagnetism do not co-exist in a single material. Interestingly, antiferromagnetism and ferroelectricity do coexist. Both $HoMnO_3$ [16] and $BiFeO_3$ [15] are multiferroic materials with antiferromagnetism and ferroelectricity. The ferroelectric mechanism of these materials is different than conventional ferroelectric materials like $BaTiO_3$ or lead zirconate titanate (PZT). The atomic structure of $HoMnO_3$ is illustrated in figure 1.3.

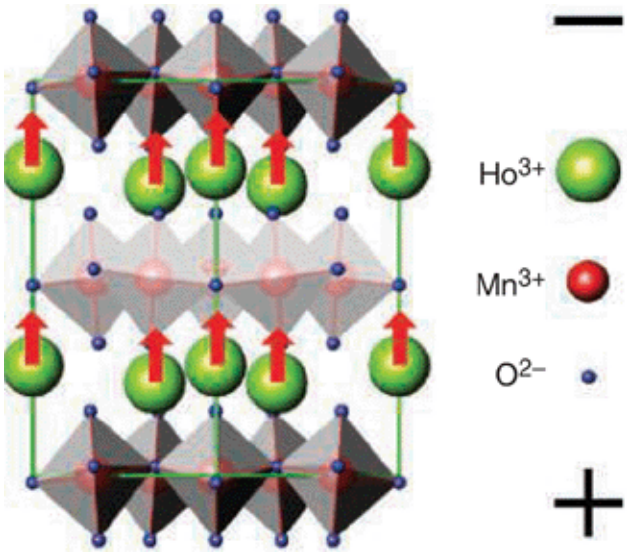

Figure 1.3. Structure of multiferroic HoMnO3. Hexagonal $HoMnO_3$ is ferroelectric because the oxygen bipyramids surrounding each Mn^{3+} ion are tilted and shifted relative to the Ho^{3+} ions. It is also magnetic, with ferromagnetic alignment of the Ho^{3+} magnetic moments combined with antiferromagnetic Mn^{3+} ordering. Therefore, hexagonal $HoMnO_3$ is multiferroic. (Figure from [16])

In addition to the small number of single phase multiferroic materials, magnetoelectric multiferroic composites composed of ferroelectric materials and ferromagnetic materials attract considerable research interest due to their high magnetoelectric coefficients at room temperature. The ferroelectric phase can produce piezoelectric strain ε in response to applied electric field E,

and the induced strain ε can change the magnetization M of the ferromagnetic phase. Early work on magnetoelectric composites was produced by van Suchtelen at Phillips Laboratories in Netherlands in the 1970s.[17] He and his coworkers prepared $BaTiO_3$-$CoFe_2O_4$ ceramic composites by solidification of eutectic compositions in the Fe-Co-Ti-Ba-O form.[18], [19] At that time, magnetoelectric multiferroic composites did not attract significant attention, and few research efforts were put in this area. Bulk magnetoelectric composites research surged at the beginning of the 21st century, when $Tb_{1-x}Dy_xFe_2$ (Terfenol-D) was developed as a magnetic material with giant magnetostriction. In 2001, Ryu et al reported the first 2-2 type structured Pb(Zr, Ti)O_3 (PZT) and Terfenol-D disks showing the magnetoelectric effect [20], [21] as shown in figure 1.4. In 2003, Dong reported magnetoelectric devices based on Terfenol-D and piezoelectric ceramics bulk composites. [22]

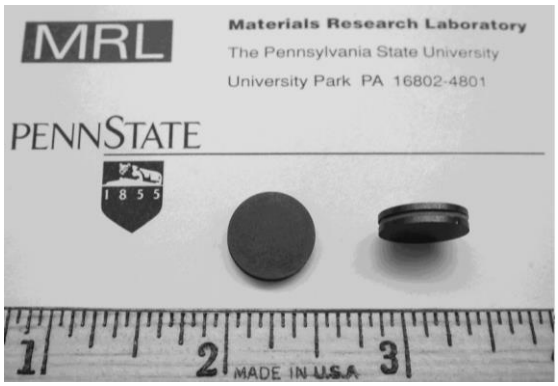

Figure 1.4. Magnetoelectric lamina composite using Terfenol-D and PZT disks. (Figure from [21])

Researchers started investigating thin film ferromagnetic/bulk piezoelectric multiferroic heterostructures starting from 2007, when Eerenstein et al reported strain-mediated magnetization manipulation in a multiferroic $La_{0.67}Sr_{0.33}MnO_3/BaTiO_3$ heterostructure.[23] Further research includes magnetic anisotropy change in response to piezoelectric strain in $Ni/Pb(Zr_xTi_{1-x})O_3$ [24] and $CoFe_2O_4/Pb(Mg_{1/3}Nb_{2/3})_{0.7}Ti_{0.3}O_3$ [25]. This effect was proposed to

tune the ferromagnetic resonance frequency.[26] In 2011, Wu et al first reported piezoelectric strain induced remnant magnetization reorientation in magnetic thin film based on a non-linear ferroelectric effect in Ni/$[Pb(Mg_{1/3}Nb_{2/3})O_3]_{(1-x)}$–$[PbTiO_3]_x$ (PMN-PT) (x≈32%) [27], [28] as shown in figure 1.5. The demonstrated reorientation of remnant magnetization in Ni thin films is ideal for strain-mediated magnetoelectric memory applications. Later in the same year, Hu et al published phase-field simulation results on high-density magnetoresistive random access memory operating at ultralow voltage at room temperature in Ni/PMN-PT heterostructures.[4] Calculations indicated that strain-mediated magnetic memory is several orders of magnitude more efficient than conventional flash-NAND and MRAM. In 2012, Hockel et al reported magnetization rotation in a micron-sized Ni ring structure controlled by bulk PMN-PT substrate.[29] This is the first experimental investigation of magnetic behavior of the nanoscale magnetic structures on a bulk piezoelectric substrate. Buzzi et al presented 180° magnetization switching in single domain Ni elliptical shaped nanomagnets (150nm × 100nm × 10nm) on bulk PMN-PT substrate in 2013.[5] Since nanomagnets have been proposed as the building block of next generation MRAM systems, this paper paved the pathway towards magnetoelectric MRAM devices with ultra-low power consumption. In 2015, Sohn et al experimentally demonstrated manipulation of magnetic particles on a Ni micron-sized ring structure/PMN-PT multiferroic structure.[30] This research is leading to future multiferroic-based lab-on-a-chip applications. Prior work has studied magnetization behavior of magnetic thin film and nanostructures in response to piezoelectric strain, however all magnetic elements are switched at once due to full electrodes on the piezoelectric producing uniform piezoelectric strain. For MRAM applications, a method is needed to control magnetism in individual strain-mediated magnetoelectric islands. This motivates the work presented in chapter 2 of this dissertation, a method using electrode

pattern design producing localized piezoelectric strain on a piezoelectric substrate to control individual magnetic elements.

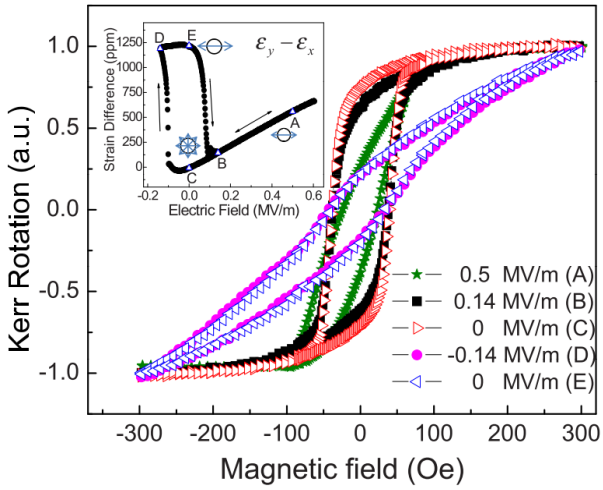

Figure 1.5. Normalized Kerr rotation hysteresis curves (M-H) of a Ni thin film along the y direction under different electric fields (letters are the representatives of the labeled strain states in the inset). The inset shows in-plane strain difference (ε_y-ε_x) as a function of electric field. The drawings indicate the magnetization state: (c) permanent easy plane, [(a) and (b)] temporary easy axis along x, and [(d) and (e)] permanent easy axis along x. (Figure from [27])

Multiferroic heterostructures with thin film ferroelectrics/thin film piezoelectrics have the advantage of miniaturized device volume and low operation voltage. Chung et al first demonstrated reversible magnetic domain wall motion in a 10nm thick Ni thin film/1.28um PZT thin film heterostructure [31] in 2008, and magnetization reorientation of 35nm thick single domain Ni elements on a 1.28um PZT thin film multiferroic heterostructure [32] in 2009. Prior work confirmed magnetization change of nanoscale magnetic elements on top of a thin film piezoelectric, however such magnetization manipulation is not deterministic. For MRAM applications, in order to accurately store information, it is required to achieve deterministic control of magnetization. This motivates the work presented in chapter 3 of this dissertation, a

method using electrode pattern design producing localized strain in three different configurations for deterministic control of a micron-sized Ni ring structure on a thin film PZT substrate.

Coupled ferromagnetic and ferroelectric behavior of materials is significantly impacted by geometry. For example, at reduced thickness of ferroelectric thin films, ferroelastic domain walls are more extensively pinned, resulting in a reduction of the electromechanical response of the films. [33] At smaller length scales, formation of domain walls is not energetically favorable and therefore the resulting electromechanical response of the sample is reduced to only the intrinsic lattice contributions.[34] Similarly, as a magnetic material's dimensions are reduced, it undergoes a transition from a multi domain (MD) to a single domain (SD) state and at smaller length scales from a SD state to a super paramagnetic (SP) state, i.e. without permanent magnetization. Magnetoelectric coupling near the MD-SD and SD-SP transition length scales is of scientific interest and of practical importance, yet little literature exists in this regime and it remains a relatively unexplored area. In 2013, Kim et al. [35] reported an electric anisotropy in multiferroic system capable of electrically switching between SP and SD state on 16 nm diameter Ni nanocrystals. This is known as the first system that successfully used electric field to switch on and off a ferromagnetic magnetic moment. The dynamic magnetic behavior of SD nanomagnets is dictated by their geometry shape through magnetic shape anisotropy. Cowburn et al studied the influence of shape on the properties of nanomagnets in sizes smaller than 500nm in the SD state. [36] Nanomagnets in various shapes, such as elliptical, triangular, square, pentagonal and circular geometries were mainly considered, as shown in figure 1.6. Considering an elliptical shaped nanomagnet as an example, its geometric major and minor axes are its magnetic easy and hard axes, respectively. For the work in this dissertation, nanomagnets were fabricated on top of piezoelectric substrates as strain-mediated multiferroic heterostructures.

Unlike directional magnetic field that can easily induce a 180° magnetization switching in nanomagnets, the piezoelectric strain, as a uniaxial effect, can at most induce a 90° magnetization reorientation when acting alone.[6] The shape of the nanomagnets can be optimized for strain-mediated control of magnetization in order to achieve deterministic 180° magnetization reorientation. This motivates the research in chapter 4 of this dissertation, the design of novel "peanut" and "cat-eye" shaped nanomagnets for 180° deterministic control of magnetization in response to piezoelectric strain.

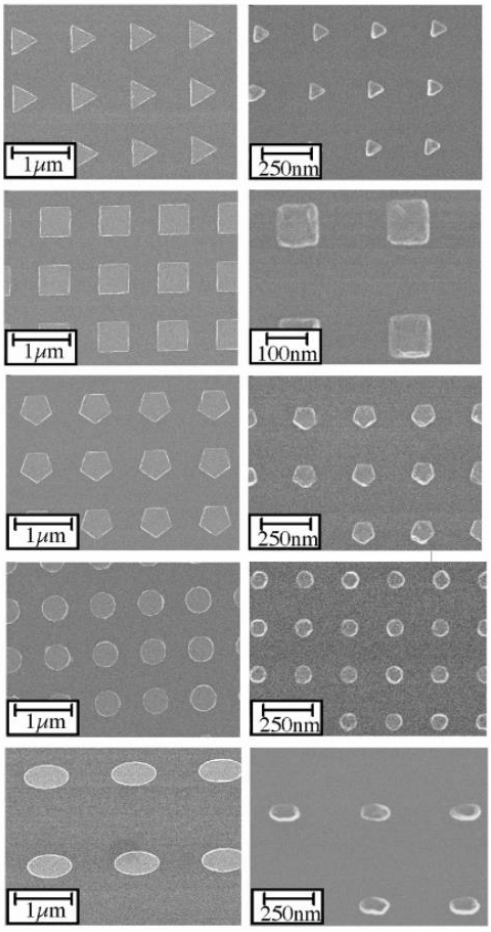

Figure 1.6. SEM images of nanomagnets in different shapes fabricated during this study [36]. The sizes are 500 nm (left-hand column) and <100 nm (right-hand column). (Image from [36]).

1.3. Micromagnetics

Micromagnetics is a physical theory that predicts magnetic behavior at sub-micrometer scales. This length scale is considered large enough for material's atomic structure to be neglected in favor of average properties, but small enough to simulate magnetic domain structures. In this section, basic micromagnetic concepts are introduced, followed by a brief description of a fully-coupled model based on Landau-Lifshitz-Gilbert equations. Micromagnetic calculations presented in this dissertation are based on this model.

Micromagnetic simulations aim to solve for the spatial distribution of magnetization for micro and nanoscale magnetic structures. The equilibrium state of magnetic system is determined by the minimum total free energy density E_{tot} in the form [37]

$$E_{tot} = E_{zm} + E_{ex} + E_{anis} + E_{demag} + E_{el} \tag{1.1}$$

including Zeeman energy density E_{zm} (i.e., magnetostatic energy density), exchange energy density E_{ex}, magnetocrystalline anisotropy energy density E_{anis}, demagnetization energy density E_{demag} and elastic energy density E_{el}.

Zeeman energy density E_{zm} arises when applying magnetic field to a magnetic moment. The Zeeman energy density is proportional to the magnitude of applied magnetic field. The expression is

$$E_{zm} = -\mu_0 M_s (\underline{\mathrm{m}} \cdot \underline{H}_{ext}) \tag{1.2}$$

where μ_0 is the permeability of the free space, $\underline{\mathrm{m}}$ is the magnetization normalized by the saturation magnetization M_s and $\underline{H}_{ext}$ is the applied magnetic field. Clearly Zeeman energy density E_{zm} is minimized when $\underline{\mathrm{m}}$ aligns with $\underline{H}_{ext}$.

Exchange energy density E_{ex} arises from exchange interaction between neighboring magnetic moments. The expression [37] is

$$E_{ex} = A_{ex}(\nabla \underline{\mathrm{m}})^2 \tag{1.3}$$

where A_{ex} is the exchange stiffness constant. $\nabla \underline{\mathrm{m}}$ is the normalized magnetization gradient and $\nabla \underline{\mathrm{m}} = 0$ when all $\underline{\mathrm{m}}$ vectors are pointing along the same direction without a magnetization gradient. For ferromagnetic materials like Ni and Fe, A_{ex} is a positive constant. E_{ex} is minimized when $\nabla \underline{\mathrm{m}}$ is minimized as neighboring magnetic moments being parallel to each other. Hence, in ferromagnetic materials like Cr and NiO, exchange interaction favors neighboring magnetic moments pointing along the same direction. For antiferromagnetic materials, however, A_{ex} is a negative constant. Hence E_{ex} is minimized when $\nabla \underline{\mathrm{m}}$ is minimized as neighboring magnetic moment being antiparallel to each other. Hence in antiferromagnetic materials, exchange interaction favors magnetic moments pointing opposite to each other. For the work in this dissertation, ferromagnetic materials with positive exchange stiffness constant are mainly modeled.

The anisotropy energy density E_{ansi} describes the angular dependence of the free energy for a crystal of a given symmetry. This is also called magnetocrystalline anisotropy. The physical origin of magnetocrystalline anisotropy is spin-orbit interaction. The outcome is that it takes

more energy to magnetize it along certain crystalline directions than along others. Hence there are intrinsic magnetic easy and hard axes in a magnetic crystal. For example, in face-center-cubic Nickel structures, [111] directions are easy axes; [100] directions are hard axes. In single crystal materials, E_{ansi} is minimized when magnetization is along the magnetic easy axes. For a polycrystalline magnetic material, the net magnetocrystalline anisotropy is zero on average. Hence when simulating polycrystalline materials, the anisotropy energy density E_{ansi} is assumed zero. The general expression for anisotropy energy density as a power series in even orders of magnetization is

$$E_{ansi} = K_0 + K_1(m_1^2 m_2^2 + m_2^2 m_3^2 + m_3^2 m_1^2) + K_2(m_1^2 m_2^2 m_3^2) + \ldots \tag{1.4}$$

where K_0, K_1, K_2…are material dependent anisotropy constants. [38]

The demagnetization energy density E_{demag} is a magnetostatic energy term from the demagnetizing field, which is the magnetic field generated by the magnetic sample upon itself. The demagnetizing field acts on magnetic structures so as to reduce the total magnetic moment. The expression of the demagnetizing energy density is

$$E_{demag} = -\frac{1}{2}\mu_0 M_s(\underline{\mathrm{m}} \cdot \underline{H}_d) \tag{1.5}$$

where $\underline{H}_d$ is the demagnetizing field. $\underline{H}_d$ is determined from Ampere's law ($\nabla \times \underline{H}_d = 0$)and Gauss's law ($\nabla \cdot \underline{B} = 0$) with the constitutive relation

$$\underline{B} = \mu_0(\underline{H}_d + M_s \underline{m}) \tag{1.6}$$

From the curl of $\underline{H}_d$ equal to zero we obtain a magnetic potential ϕ such that,

$$\underline{H}_d = -\nabla\phi \tag{1.7}$$

Equations (1.6), (1.7) and the divergence of B satisfy the Poisson equation

$$\nabla^2\phi = \nabla\cdot(\mathrm{M_s}\,\underline{\mathrm{m}}) \tag{1.8}$$

which is solved and then used to determine $\underline{H}_d$. [39]

The magnetoelastic effect characterizes magnetization change of magnetostrictive materials in response to an applied mechanical stress. The elastic energy density term E_{el} in equation (1.1) can be written as

$$E_{el} = \frac{1}{2}\underline{\underline{\varepsilon}}^{el} : \underline{\underline{\underline{\underline{C}}}} : (\underline{\underline{\varepsilon}}^{el}) \tag{1.9}$$

where $\underline{\underline{\underline{\underline{C}}}}$ is the elastic stiffness tensor and $\underline{\underline{\varepsilon}}^{el}$ is the elastic strain tensor of the material. In magnetostrictive materials, magnetic moments and displacements are coupled. Therefore, the total strain $\underline{\underline{\varepsilon}}$ in a ferromagnetic material is composed of a magnetic eigenstrain, $\underline{\underline{\varepsilon}}^{\mathrm{m}}(\underline{\mathrm{m}})$, and the elastic strain, $\underline{\underline{\varepsilon}}^{el}$, contributions with total strain

$$\underline{\underline{\varepsilon}} = \underline{\underline{\varepsilon}}^{\mathrm{m}}(\underline{\mathrm{m}}) + \underline{\underline{\varepsilon}}^{el} \tag{1.10}$$

where $\underline{\underline{\varepsilon}}^{m} = \underline{\underline{\underline{\underline{\lambda}}}}^{m}\,\underline{m}\underline{m}^{T}$ is the strain associated with local magnetization changes and $\underline{\underline{\underline{\underline{\lambda}}}}^{m}$ is the magneto-mechanical coupling tensor.[40] In the case of a cubic crystal, $\underline{\underline{\varepsilon}}^{m}$ is given by

$$\varepsilon_{ij}^{m} = \begin{cases} \frac{3}{2}\lambda_{100}(m_i m_j - \frac{1}{3}) & i = j \\ \frac{3}{2}\lambda_{111} m_i m_j & i \neq j \end{cases} \tag{1.11}$$

where λ_{100} and λ_{111} are the magnetostriction constants along the <100> and <111> directions.

The total strain $\underline{\underline{\varepsilon}}$ is related to the displacement $\underline{u}$ by

$$\underline{\underline{\varepsilon}} = \frac{1}{2}(\nabla \underline{u} + (\nabla \underline{u})^{\mathrm{T}}) \tag{1.12}$$

and the stress tensor $\underline{\underline{\sigma}}$ is related to the strains as

$$\underline{\underline{\sigma}} = \underline{\underline{\underline{\underline{C}}}}\,\underline{\underline{\varepsilon}}^{el} = \underline{\underline{\underline{\underline{C}}}}[\underline{\underline{\varepsilon}} - \underline{\underline{\varepsilon}}^{m}(\underline{m})] \tag{1.13}$$

where the stress distribution is governed by the elastodynamic equation

$$\rho \frac{\partial^2 \underline{u}}{\partial t^2} - \nabla \cdot \underline{\underline{\sigma}} = 0 \tag{1.14}$$

and ρ is the mass density. Substituting (1.11) and (1.12) into (1.13) leads to

$$\rho \frac{\partial^2 \underline{u}}{\partial t^2} - \nabla \cdot \underline{\underline{\underline{\underline{C}}}}\left[\frac{1}{2}(\nabla \underline{u} + (\nabla \underline{u})^{\mathrm{T}})\right] + \nabla \cdot \underline{\underline{\underline{\underline{C}}}}\left(\underline{\underline{\underline{\underline{\lambda}}}}^{m}\, \underline{m}\underline{m}^{T}\right) = 0 \tag{1.15}$$

For dynamic simulations, the magnetic domain structure is described by the spatially distributed magnetization M = M_s (m_x, m_y, m_z), where M_s and m_i (i = x, y, z) represent the saturation magnetization and the direction cosines, respectively. The equation of motion describing the evolution of the magnetization temporally is the Landau-Lifshitz-Gilbert equation,

$$\frac{\partial \underline{m}}{\partial t} = -\mu_0 \gamma \left(\underline{m} \times \underline{H}_{eff} \right) + \alpha \left(\underline{m} \times \frac{\partial \underline{m}}{\partial t} \right) \tag{1.16}$$

where γ and α are the gyromagnetic ratio and the damping coefficient, respectively. $\underline{H}_{eff}$ is the effective magnetic field. $\underline{H}_{eff}$ is achieved by differentiating the total magnetization density E_{tot} with respect to magnetization with the expression

$$\underline{H}_{eff} = -\frac{1}{\mu_0 M_s} \frac{\partial E_{tot}}{\partial \underline{m}} = \underline{H}_{ext} + \underline{H}_{ex} + \underline{H}_{anis} + \underline{H}_{demag} + \underline{H}_{me} \tag{1.17}$$

where $\underline{H}_d$ is shown in equation (1.6). The other terms of $\underline{H}_{eff}$ can be calculated as

$$\underline{H}_{ex} = \frac{2A_{ex}}{\mu_0 M_s} \Delta \underline{m} \tag{1.18}$$

$$H^i{}_{anis} = -\frac{2m_i}{\mu_0 M_s} \left[K_1 (m_j{}^2 + m_k{}^2) + K_2 (m_j{}^2 m_k{}^2) \right] \tag{1.19}$$

$$\underline{H}_{me} = -\frac{1}{\mu_0 M_s} \underline{\underline{\underline{C}}} \left(\underline{\underline{\varepsilon}} - \underline{\underline{\varepsilon}}^m (\underline{m}) \right) \cdot \frac{\partial \underline{\underline{\varepsilon}}^m (\underline{m})}{\partial \underline{m}} \tag{1.20}$$

Equations (1.7) and (1.15-20) and various parameters $\underline{u}$, ϕ and $\underline{m}$ are solved using the finite element method. Computational simulations for the work in this dissertation were performed based on a mathematical model implemented in a commercially available partial differential equation solver COMSOL (www.comsol.com). In general, initial conditions were first applied followed by a Newton iteration approach to converge for a given time step. Once converged, the time step is advanced and the process is repeated. The mathematical model described in this paper can be similarly implemented in other finite element or numerical analysis packages that provide platforms to solve partial differential equations. For all numerical

problems, convergence studies on mesh size and time step size were conducted to ensure accuracy. Ni properties used in simulation are M_s=4.8×10^5(A/m), A_{ex}=1.05×10^{-11}(J/m), λ_{100} =-46×10^{-6}, λ_{111}=-24×10^{-6}, c_{11}=2.5×10^{11}(N/m^2), c_{12}=1.6×10^{11}(N/m^2) and c_{44}=1.18×10^{11}(N/m^2). The Gilbert damping constant was set as α =0.5 to improve model stability.

1.4.Micro and Nano-fabrication

American physicist Richard Feynman commented in 1959 that “There's Plenty of Room at the Bottom” at the annual meeting of the American Physical Society. Since then, research in microelectromechanical systems (MEMS) and nanoelectromechanical systems (NEMS) has seen considerable progress. Over the last few decades, researchers can make smaller and smaller feature in MEMS and NEMS systems. The size of the first working transistor is close to the size of a basketball (developed by Lucent Technologies in 1947), on the order of a few decimeters. The current transistor is only 11nm wide, implemented by Intel in 2015 on its newest generation of processors. The current transistor is 10^7 times smaller than its ancestor, while maintaining the same function. This is an amazing achievement.

Engineering on the small scale is made possible by micro and nano-fabrication techniques. A micro and nanoscale device is fabricated using a series of processes, including lithography (optical lithography, extreme ultraviolet lithography, e-beam lithography, etc.), metallization (e-beam evaporation, thermal evaporation, sputtering deposition, atomic layer deposition, pulsed laser deposition, etc.) and etching (lift-off, sputtering etching, focused ion-beam etching, etc.). For the work in this dissertation, the process of optical/e-beam lithography, e-beam evaporation and lift-off is used for device fabrication. Figure 1.1 is the schematic for the process.

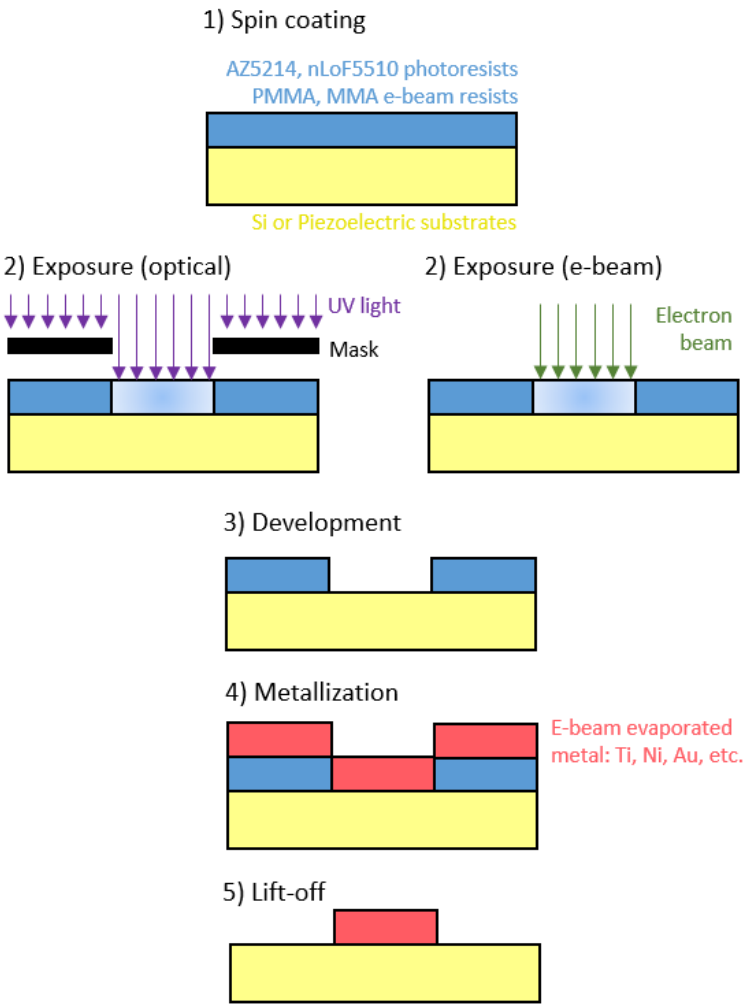

Figure 1.7. Fabrication process for micro and nanoscale structures based on optical/e-beam lithography, e-beam evaporation and lift-off techniques.

Optical lithography, i.e., photolithography, defines the shape of the microstructures being patterned on a substrate. It uses visible ultraviolet light to transfer a geometric pattern from a prepared mask to a layer of photoresist deposited on the substrate. Optical lithography is considered a cheap and convenient way (compared with e-beam lithography) of defining patterns down to a few microns in size. However, this technique is limited by light diffraction and fails once structures are smaller than 1 micron. Optical lithography usually requires five processing

steps, including substrate cleaning, photoresist spin coating, soft baking, exposure and development. AZ5214 and nLoF5510 are two types of photoresists being used in the work in this dissertation. The process recipe of AZ5214 was optimized and is shown in table 1.2. The thickness of AZ5214 photoresist after process is about 1 micron. This process is usually for the metallization of large Au electrodes thicker than 100nm, however the edge roughness is not ideal. For the best geometric shapes of exposed patterns, nLoF5510 photoresist is suggested with the recipe shown in table 1.3. The thickness of the nLoF5510 photoresist after the process is about 200-300nm. This recipe is ideal for metallization of thin (10-50nm) ferromagnetic materials like Ni. Both AZ5214 and nLoF5510 can be stripped away by acetone or AZ300T stripper during the lift-off process.

Table 1.2. AZ5214 photoresist (image reversal mode) recipe

Step	Process	Description
1	Substrate cleaning	Clean the substrate with Acetone, Methanol and Isopropyl alcohol (IPA). Rinse the sample with DI water and bake for 10min at 100°C. Leave the substrate in HMDS chamber for 10mins.
2	Photoresist spin coating	Set the substrate on a spin coater. Drop a few droplets of AZ5214 photoresist on the substrate. Set the program: step 1, spinning at 500rpm for 6s; step 2, spinning at 3000rpm for 40s; step 3, stop spinning. 500rpm is the ramp for the process.
3	Soft baking	Bake at 90°C for 1min.
4	Exposure	With mask, expose the sample using ultraviolet light with 66mJ/cm^2 as dose.
5	Post exposure baking	Bake at 115°C for 45s.
6	Flood exposure	Without mask, expose the sample using ultraviolet light with 200mJ/cm^2.
7	Development	Immerse the sample in (AZ400K):(DI water) = 1:4 solution for 45s.

Table 1.3. nLoF5510 photoresist recipe

Step	Process	Description
1	Substrate cleaning	Clean the substrate with Acetone, Methanol and Isopropyl alcohol (IPA). Rinse the sample with DI water and bake for 10min at 100°C. Leave the substrate in HMDS chamber for 10mins.
2	Photoresist spin coating	Set the substrate on a spin coater. Drop a few droplets of nLoF5510 photoresist on the substrate. Set the program: step 1, spin at 500rpm for 6s; step 2, spin at 3000rpm for 50s; step 3, stop spinning. 500rpm is the ramp for the process.
3	Soft baking	Bake at 90°C for 1min.
4	Exposure	With mask, expose the sample using ultraviolet light with 100-120mJ/cm^2 as dose.
5	Post exposure baking	Bake at 110°C for 60s.
6	Development	Immerse the sample in AZ300MIF developer for 60s.

E-beam lithography enables fabrication of sub-micron patterns with sub-10nm resolution. Similar to scanning electron microscopy (SEM), e-beam lithography uses a scanning focused electron beam to draw custom shapes on the e-beam resist deposited on a substrate. The electron beam changes the solubility of the resist and can make the exposed (or unexposed) area soluble to a specific solvent. The exposed (or unexposed) area can be removed by specific solvent, called developer, during the development process. E-beam lithography is a mask-less process. The e-beam writing pattern is customized in a computer program and the pattern layout can be changed after each lithography process. E-beam lithography outweighs optical lithography with much higher resolution and easy change of exposure patterns. However, e-beam lithography has very low throughput and also high cost. For the work in this dissertation, e-beam lithography is used for fabrication of nanoscale structures. E-beam lithography requires the use of double-layer

methyl methacrylate (MMA) EL6 and polymethyl methacrylate (PMMA) AZ950K e-beam resists. The recipe for this process is shown in table 1.4. The double-layer e-beam resists can be stripped away by AZ300T stripper at 80°C or N-Methyl-2-pyrrolidone (NMP) at 60°C for lift-off process. If the sample is thermal sensitive (e.g., piezoelectric substrate), acetone and NMP can be used at room temperature for lift-off with a longer stripping time (usually 24 hours). Leaving the sample upside down during lift-off process is suggested.

Table 1.4. Recipe for MMA/PMMA double-layer e-beam resist

Step	Process	Description
1	Substrate cleaning	Clean the substrate with Acetone, Methanol and Isopropyl alcohol (IPA).
2	E-beam resist spin coating (MMA EL6 layer)	Set the substrate on a spin coater. Drop a few droplets of EL6 e-beam resist on the substrate. Set the program: step 1, spin at 500rpm for 1s (ramp 500rpm); step 2, spin at 3000rpm for 45s (ramp 1000rpm); step 3, stop spinning (ramp 500rpm).
3	Soft baking	Bake at 170°C for 5min.
4	E-beam resist spin coating (PMMA AZ950K layer)	Set the substrate on a spin coater. Drop a few droplets of EL6 e-beam resist on the substrate. Set the program: step 1, spin at 500rpm for 1s (ramp 500rpm); step 2, spin at 3000rpm for 45s (ramp 1000rpm); step 3, stop spinning (ramp 500rpm).
5	Soft baking	Bake at 170°C for 5min.
6	Exposure	Exposure dose depends on material types. A dose test is recommended when fabrication structure on a new substrate.
7	Development	Immerse the sample in MIBK:IPA = 1:3 developer for 60s. Rinse with IPA and use N_2 to dry the sample.

The fabricated nanoscale structures in this dissertation are directly on top of piezoelectric materials. After e-beam exposure the electrons, as charged particles, accumulate at the exposed area on non-conductive dielectric materials (such as piezoelectrics). These accumulated electrons

charge the area negatively and deflect the e-beam when exposing the area immediately next to the charged area. This undesired charging issue may induced ill-defined pattern during e-beam lithography process. A method to mitigate this effect is to deposit a conductive layer on top of the double-layer e-beam resists before e-beam exposure. A thin gold layer (about 20nm) is prepared by sputtering deposition for the work in this dissertation. After e-beam exposure, this thin Au layer needs to be removed before development. A solvent with (TFA gold etchant):(DI water) = 1:3 can effectively remove such Au layer in 10s.

E-beam evaporation, i.e. electron beam physical vapor deposition, is a type of physical vapor deposition. In the deposition process, a target anode is bombarded with accelerated electron beam. The kinetic energy of electrons is transferred to the thermal energy of the target. This heats up the target, causing it to melt and producing vapor. The resulting vapor evaporates and re-solidifies as thin films on top of the sample. The sample is usually processed by either optical lithography or e-beam lithography before e-beam evaporation process. E-beam evaporation techniques can be used to deposit both metal (Ti, Al, Au, Pt, Ni, Cu, Fe, etc.) and oxides (SiO_2, Al_3N_4, etc.). The deposition rate controls the grain structure and surface topography of the deposited thin films. The deposition rate used for the work in this dissertation is shown in table 1.5.

Table 1.5. E-beam evaporation deposition rate

Material	Deposition rate
Titanium	0.5-1 Å/s
Nickel	0.5-1 Å/s
Aluminum	1-2 Å/s
Gold	>3 Å/s
Permalloy (NiFe)	1 Å/s
SiO_2	1-2 Å /s

1.5.Magnetic characterization

1.5.1. Magneto-optical Kerr effect

The magneto-optical Kerr effect (MOKE) was discovered by John Kerr in 1877. MOKE describes the changes to light reflected from a magnetized surface. The MOKE effect originates from the magnetic circular dichroism effect: exchange and spin-orbit coupling in a magnetic material lead to different absorption spectra for left-and right-circularly polarized light. In MOKE magnetometry, linearly polarized incident laser can become elliptically polarized when reflected from a magnetic material surface. The change in polarization is proportional to the magnetization component that is parallel to the reflection surface and parallel to the plane of incidence. By measuring this change in polarization, i.e., Kerr rotation (in arbitrary units), magnetization of the sample along certain directions can be qualitatively estimated. A MOKE magnetometry setup is shown in figure 1.8.

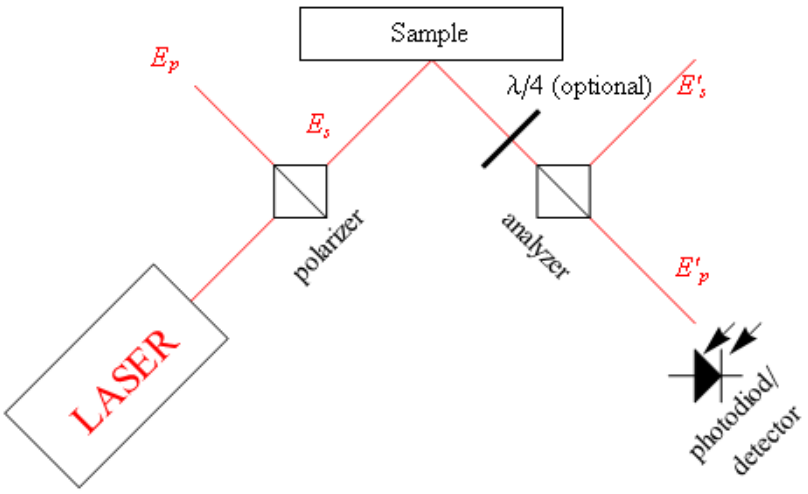

Figure 1.8. Schematic for MOKE magnetometry. (Figure from https://en.wikipedia.org/wiki/Magneto-optic_Kerr_effect)

MOKE measurement is typically performed along with applied magnetic field. By measuring the Kerr rotation while applying a bipolar magnetic field sweep, an M-H curve is generated. Figure 1.9 shows a MOKE measurement result of a 35nm thick Ni thin film. As illustrated in the figure, Kerr rotation changes relative to applied magnetic field (H-field). Once the H-field is high enough in magnitude (roughly beyond 200Oe), the Ni thin film is fully magnetized along the magnetic field direction showing maximized Kerr rotation. With a lower applied H-field, Kerr rotation represents a hysteresis loop. Because Kerr rotation is directly proportional to the net magnetization, the MOKE loop can be considered as net magnetization change in response to applied magnetic field along the field direction. Even though the absolute value of magnetization for this Ni film cannot be measured by this technique, MOKE focuses on the relative change of magnetization and dynamic magnetization behavior.

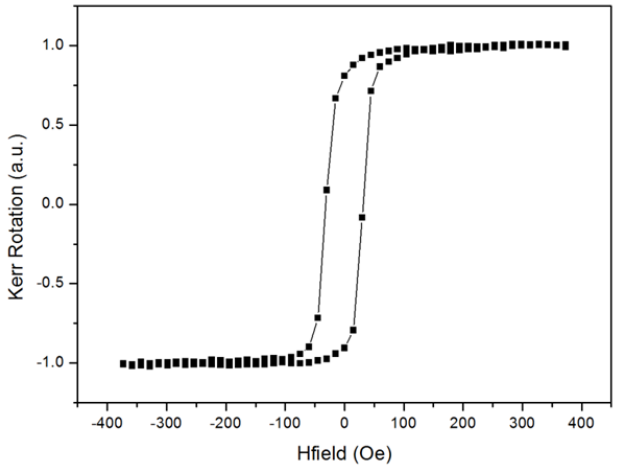

Figure 1.9. MOKE result of a 35nm thick Ni thin film.

Important information that can be extracted from this loop includes coercive field H_c (the H-field value when magnetization switches polarity, i.e., Kerr rotation switches sign), anisotropy field H_a (the H-field value when magnetization fully saturated, i.e., Kerr rotation approaches ±1) and remnant magnetization M_r (Kerr rotation value when H-field equals zero). These values are

critical to understand the magnetic anisotropy of the films. Magnetic anisotropy determines the degree to which the magnetization has a preferred direction, represented by magnetic easy axes and hard axes. When MOKE characterization along a direction yields high H_a and low M_r, this direction is considered as a hard axis. It requires a relatively large H-field to fully magnetize the sample (a high H_a) along this direction. Hence it is "hard" to magnetize the sample along this direction. Besides, low M_r indicates that without external applied magnetic field the net magnetization cannot spontaneously align with this hard axis. Hence it is "hard" for net magnetization to stay along this direction. When MOKE characterization along a direction yields M_r=1, this direction is considered an easy axis. This means that it is "easy" for net magnetization to stay along this direction in remnant. Comparing with two hard axes, the one with higher H_a is considered the "harder" axis. Comparing with two easy axes both with M_r=1, the one with higher H_c is considered as the "easier" axis. The work in this dissertation includes MOKE curve changes in response to piezoelectric strain applied to the Ni thin film. This is considered as strain-induced magnetoelastic anisotropy.

1.5.2. Magnetic force microscopy

Magnetic force microscopy (MFM) detects nanoscale magnetic domain patterns with 10-20nm resolution. Considered as an extension of conventional atomic force microscopy (AFM), MFM uses a sharp magnetized tip scanning across a magnetic sample surface. The tip acts as a detector of weak magnetic forces from sample surface through magnetic dipole-dipole interaction. The tip radius is as small as 10-50nm in diameter, hence the tip can sense the magnetic force within a highly localized area. Based on the repulsion and attraction sensed by

the magnetic tip, the domain wall patterns of the sample can be identified. The mechanism of MFM characterization is shown in figure 1.10.

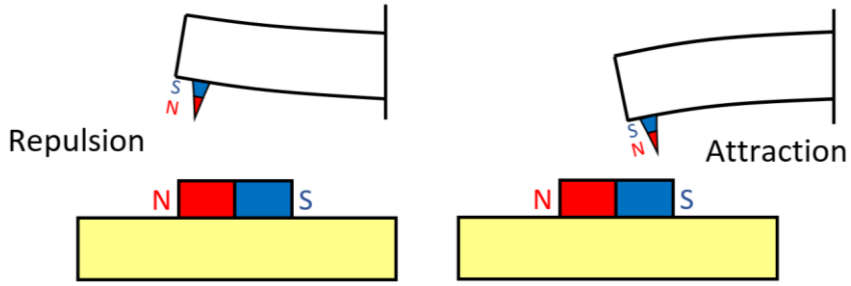

Figure 1.10. Schematic of the magnetic force microscopy.

The coating of MFM tips can be made by hard magnets like CoPt or soft magnets like Ni. The tips with hard magnet coating tends to provide stronger magnetic signal due to high saturation magnetization M_s. Likewise, the tips with soft magnet coating provide weaker magnetic signal due to low M_s. The work in this dissertation requires imaging the magnetic signal of soft magnetic structures made by Ni. Using a tip with hard magnet coating may re-magnetize the Ni nanostructure and alternate the magnetic domain patterns.[41] This effect is called tip-sample interaction and it is less likely to happen when using a tip with soft magnet coating. Only MFM images with minimum tip-sample interaction are valid. A method to check the validity of MFM images is to see if there is any clear discontinuity on the images. For a MFM image with continuous magnetic signals, there is no clear tip-sample interaction while taking the image; clear sudden magnetic signal changes indicates that the tip has alternated magnetic domain patterns. MFM images with signal discontinuities should be discarded. Figure 1.11 shows MFM images without and with tip-sample interactions. The MFM tips used for the work in this dissertation are MESP-LM (CoPt coating) from Bruker

(http://www.brukerafmprobes.com/), SC-20-LM (20nm thick Ni coating) and SC-35-LM (35nm thick Ni coating) from SmartTip (http://www.smarttip.nl/).

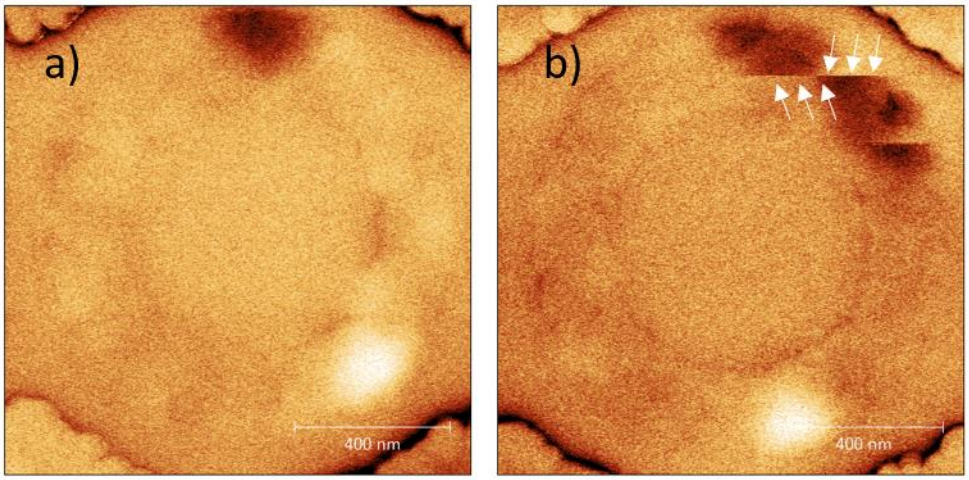

Figure 1.11. Magnetic force microscopy images (a) without tip-sample interaction and (b) with tip-sample interaction. Samples (a) and (b) are 1000nm outer-diameter, 700nm inner-diameter and 15nm thick Ni ring structures. The white arrows in (b) indicates that the magnetization of the ring structure has been moved by the MFM tip during imaging.

The magnitude of local stray field from the magnetic sample determines the strength of the MFM signal, because the measured MFM signal mainly comes from the dipole-dipole interaction between the tip magnet and the sample magnet. Hence, materials with higher M_s (saturation magnetization), and thicker magnetic structures typically yield stronger MFM signal. Comparing $Ni_{80}Fe_{20}$ permalloy (M_s=800emu/cm^3) with Ni (M_s=485emu/cm^3), $Ni_{80}Fe_{20}$ has higher M_s. In order to increase the contrast of MFM signals, a thin layer of $Ni_{80}Fe_{20}$ can be deposited on top of Ni to increase the magnitude of the local stray field. Figure 1.12 includes MFM images of various nanostructures made by 5nm $Ni_{80}Fe_{20}$ on top of 35nm thick Ni with high contrast, demonstrating complex magnetic domain distributions.

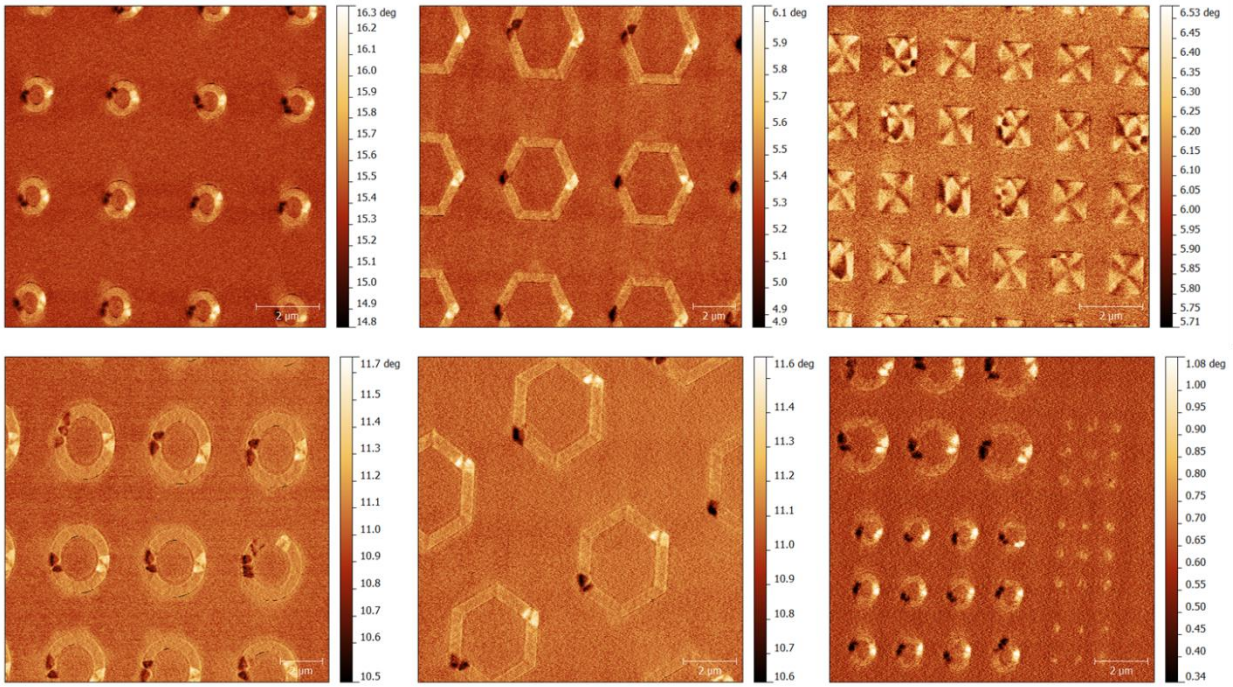

Figure 1.12. MFM images of 5nm $Ni_{80}Fe_{20}$/35nm Ni nano structures in various shapes.

MFM is particularly useful for imaging magnetization of nanoscale magnetic devices. MFM is also the only commercially available tool that can achieve 10-20nm magnetic imaging resolution. Other techniques that can achieve such high resolutions include photoemission electron microscopy (PEEM) and scanning electron microscopy with polarization analyzer (SEMPA), either requiring large scale infrastructure (synchrotron) or very expensive to use. Even though MFM has the disadvantage of tip-sample interaction, it is still considered the first choice for most nanoscale magnetization characterization needs.

Chapter 2. Controlling individual magnetic islands on bulk PZT

2.1.Literature review

Large strain-mediated magnetoelectric (ME) coupling can be obtained from composites comprised of piezoelectric and magnetostrictive constituents arranged with various connectivities.[3] The underlying mechanism is a coupling between the piezoelectric and magnetostrictive effects. When the magnetoelectric composite consists of laminated thin layers of piezoelectric and magnetostrictive materials with the magnetization in the plane of the magnetic layer, an in-plane tensile strain component and an orthogonal in-plane compressive strain component will drive in-plane magnetization rotation. This has been observed in thin film Ni.[24] This strain state can be produced by a piezoelectric ceramic actuator using the sign difference between the piezoelectric coefficients d_{33} and d_{31}, and by certain anisotropic [011] cut and poled rhombohedral relaxor ferroelectric single crystals.[42] The magnetization is maintained in the plane of the film by the shape anisotropy. This approach has been used to tune ferromagnetic resonance (FMR) [26], induce magnetic coercive field changes [43], and induce magnetization reorientation in magnetic thin film [24], [25], [27], [28] and in small magnetic islands [5], [29]. In the case of the islands, although the in-plane magnetization of the islands was rotated, all islands experienced the same strain and thus the magnetization of all islands rotated at once. Magnetic random access memory (MRAM) applications require a method to control individual magnetic islands [4], the subject of the following discussion.

2.2. Electrode pattern design

A linear piezoelectric finite element analysis (FEA) of small electrodes on the top surface of a thickness poled piezoelectric plate with the bottom side fully electroded was performed. The goal was to identify a geometry that overcomes the in-plane strain clamping effect that occurs when small electrodes are placed on a large piezoelectric plate or a thin piezoelectric film clamped by a substrate. The results indicate that when the electrode dimensions are comparable to the thickness of the piezoelectric plate, the out-of-plane (d_{33}) expansion and in-plane (d_{31}) contraction of the region beneath the electrodes produces a highly localized strain field. The strain fields interact when two such electrodes are separated by a distance of one to two times the plate thickness. This induces an in-plane bi-axial strain between the electrodes (tensile in one direction and contractile in the orthogonal direction). The piezoelectric coefficients and dimensions used in the simulations were d_{33}= 690 pCN^{-1} and d_{31}= -340 pCN^{-1}, electrode dimensions 0.6 × 0.6 mm^2, electrode separation distance 1.5 mm and 1.0 mm, plate thickness 0.5mm, and applied potential 1.5 kV (nominal electric field E_3=3 MVm^{-1} beneath the small surface electrodes with the entire bottom surface at zero potential). Figure 2.1 shows the simulated bi-axial strain difference ($\Delta\varepsilon = \varepsilon_{xx} - \varepsilon_{yy}$) produced between the electrodes by the two electrode separation distances. Additional finite element simulations that included the conducting lines connected to the electrodes indicated a negligible effect on the strain field between the electrodes (not shown). Comparing figure 2.1(a) and figure 2.1(b), the bi-axial strain response in the piezoelectric material between the electrodes increases significantly as the electrode spacing approaches the thickness of the piezoelectric layer (roughly 680 ppm for L= 1.5 mm and 1100 ppm for L=1.0 mm where L is the distance between the electrodes). Only a small region

surrounding the electrodes is strained, thus enabling application to arrays of indexed magnetic elements.

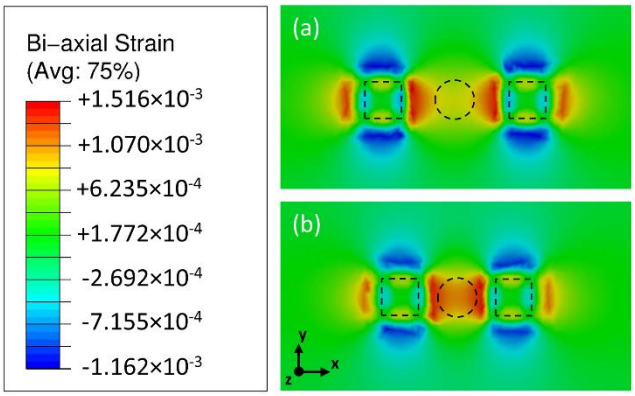

Figure 2.1. Top view of FEA simulations of 1.5kV applied to an electrode pair with the bottom surface at zero potential showing the bi-axial strain response (ε_{xx}-ε_{yy}) in the vicinity of an electrode pair with inter-pad spacing (a) L=1.5 mm and (b) L =1.0 mm. The dashed line squares and circle indicate the location of the electrode pads and the magnetic element, respectively.

2.3. Experiment result

Experiments were designed to verify that the localized strain field was generated between the electrodes. The experiments used a piezoelectric substrate with patterned electrodes arranged around a magnetostrictive island as shown in figure 2.2. Ni was chosen for the islands as its response to bi-axial strain has been well characterized. [5], [24], [27], [28] In this configuration, when a positive voltage is applied to one pair of top electrodes (either A-A or B-B) and the bottom surface is grounded as shown in figure 2.2(a), the piezoelectric material immediately under the electrodes expands out-of-plane (z-axis) and contracts in the x- and y-directions in-plane. Strain-displacement compatibility requires that the piezoelectric strain be compatible with the overall strain field. This induces a mechanical stretching of the material between the surface electrodes to accommodate the electric field induced in-plane contraction. When voltage is applied to electrodes A-A, the magnetic element is elongated along the x-direction ($\varepsilon_{xx} > 0$) and

is contracted in the y-direction ($\varepsilon_{yy} < 0$). This combined action of elongation and contraction represents a local bi-axial strain difference in the region between the electrode pair, i.e. $\varepsilon_{xx}-\varepsilon_{yy} > 0$. The bi-axial strain between the electrodes is rotated 90 degrees when voltage is applied to electrode pair B-B. This bi-axial strain difference $\Delta\varepsilon= \varepsilon_{xx}-\varepsilon_{yy}$ induces in-plane magnetoelastic anisotropy through the negative magnetostriction of Ni.

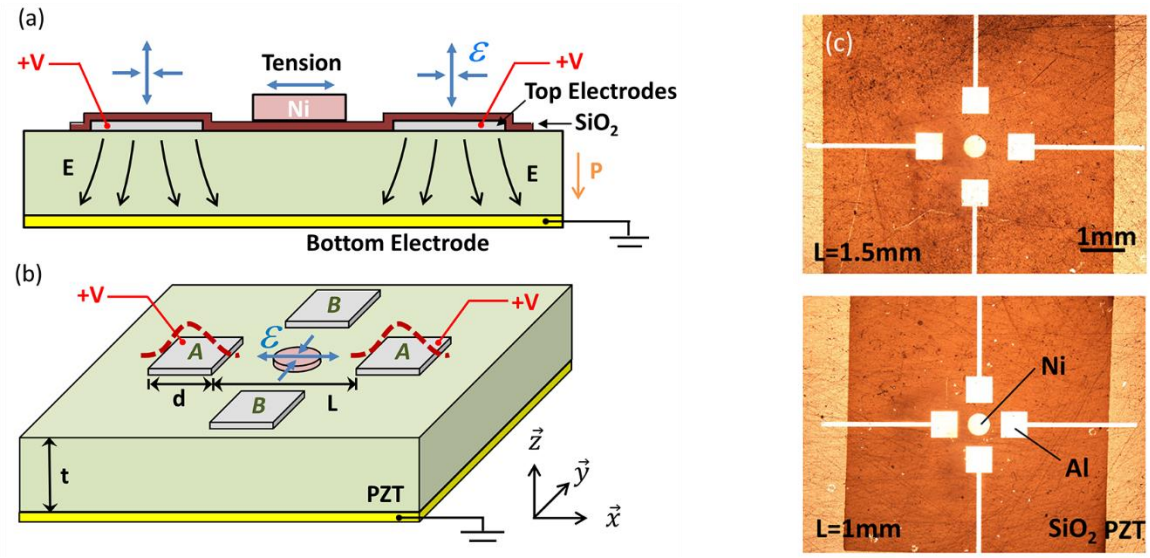

Figure 2.2. Schematic of a device structure that generates localized bi-axial surface strain that interacts with a magnetostrictive element. (a) Cross section and (b) isometric view. The dashed line in (b) illustrates the out-of-plane expansion under the electrodes that creates the bi-axial strain field ($\varepsilon_{xx}-\varepsilon_{yy} >0$) in the central Ni island. (c) Top views of fabricated patterned electrodes and Ni elements on PZT observed using an optical microscope.

The configuration shown in figure 2.2 was fabricated on a polycrystalline plate of $Pb[Zr_xTi_{1-x}]O_3$ (PZT) with x approximately 0.52. A commercially obtained plate designated PZT-5H of dimensions $10\times10\times0.5mm^3$ was mechanically polished with 3μm abrasive. The electrode patterns and magnetic Ni islands were deposited on the PZT plates using two-step optical mask lithography. As shown in figure 2.2(b) and (c), the electrode pads were $0.6\times0.6mm^2$ squares with inter-pad spacing of L=1.5mm or L=1.0mm. The small lines that connect to the pads were used for electric connection. Electrodes of 3nm Ti (adhesion layer) and 100nm Al

were deposited by e-beam evaporation (CHA Solutions). 50nm of SiO_2 was next evaporated to create an insulating layer to reduce the likelihood of electric breakdown between the pads. Finally, by the same technique a film of 3nm Ti/35nm Ni was deposited. The circular shape of the Ni was selected to minimize the effect of shape anisotropy in the multi-domain Ni that might directionally interfere with magnetization changes. The variation of the radius of the circular Ni element was less than 3% as measured from the optical micrographs. The uniformity of the Ni thickness was not measured. The SiO_2 insulation layer was used to screen charge, reducing the influence of any charge-induced ME effect on the measured magnetization change. [44], [45] Formation of a nickel oxide surface layer can be avoided by deposition of a capping layer. A capping layer was not used in this work. Ni has been studied as a capping layer for other magnetic thin films and it was found that it takes 300 hours in air to oxidize a 0.6 nm Ni layer.[46] The measurements reported here were performed within 300 hours of processing, and an oxidation layer of <0.6 nm on the Ni should have little or no effect on magnetization measurements performed on a 35nm Ni film. The Ni was e-beam evaporated and thus was not expected to have an initial easy axis such as that observed when Ni is magnetron sputtered; yet the experimental results indicate an initial bias in the M-H loops.

The electric field-induced magnetic anisotropy of the Ni was measured using longitudinal magneto-optical Kerr effect (MOKE) magnetometry. The magnetization of 35 nm thick Ni is in-plane due to the shape anisotropy. [24], [38] The measurement direction of the Kerr rotation (i.e. the direction of the laser beam) was parallel to the direction of the applied magnetic field. The laser beam diameter was 0.5mm the same as the diameter of the Ni disc, thus the MOKE results represent the average magnetic response of the Ni disc. Figure 2.3 shows the normalized Kerr rotation hysteresis curves (M-H) for the electrode spacing case of L=1.5 mm. Voltages of 0.5

kV, 1.0 kV, and 1.5 kV were applied to electrode pair A-A (ε_{xx}-ε_{yy} >0) and then B-B (ε_{xx}-ε_{yy} <0) during the MOKE measurement. For clarity, only the 1.5 kV case is shown.

Figure 2.3(a) shows the magnetic response with H parallel to the x-axis and figure 2.3(b) shows the magnetic response with H parallel to the y-axis. A comparison of the M-H loops prior to application of voltage to the electrodes (initial state) indicates the x-axis is a harder axis than the y-axis. Note the rounding of the M-H loop as the coercive field is approached in Figure 2.3(a). The same loop in figure 2.3(b) with H parallel to the y-axis displays similar rounding at the bottom side of the loop and a sharper transition at the top of the loop. This effect is still present after the voltage cycles. Comparing with initial state, the loops change considerably when voltage is applied to electrode pair A-A. This is anticipated from previous work on Ni films[2]. In this case the strain component ε_{xx} is tensile and component ε_{yy} is compressive. "A-A 1.5kV" in figure 2.3(a) indicates a hard axis is induced in the x-direction while "A-A 1.5kV" in figure 2.3(b) indicates an easy axis is induced in the y-direction. This is seen as the hysteresis loop becoming slanted to the right in figure 2.3(a) and requiring around 400 Oe to approach saturation, and as the hysteresis loop becoming much more square in figure 2.3(b). When the voltage is removed from electrode pair A-A as shown in "A-A 0V (Rem.)" in figure 2.3(a) and 2.3(b), there is a residual hard axis in the x-direction and easy axis in the y-direction. This is likely the result of a change in the remnant strain state of the ferroelectric, an effect that cannot be predicted using a linear finite element analysis. When voltage is applied to electrode pair B-B ("B-B 1.5kV" in figure 2.3(a) and (b)), the sign of the strain components is reversed and the easy and hard axes invert, with the x-axis becoming the new easy axis and the y-axis becoming the new hard axis. The direction of the voltage-induced magnetoelastic anisotropy has been rotated 90° by removing the voltage from A-A and applying voltage to B-B.

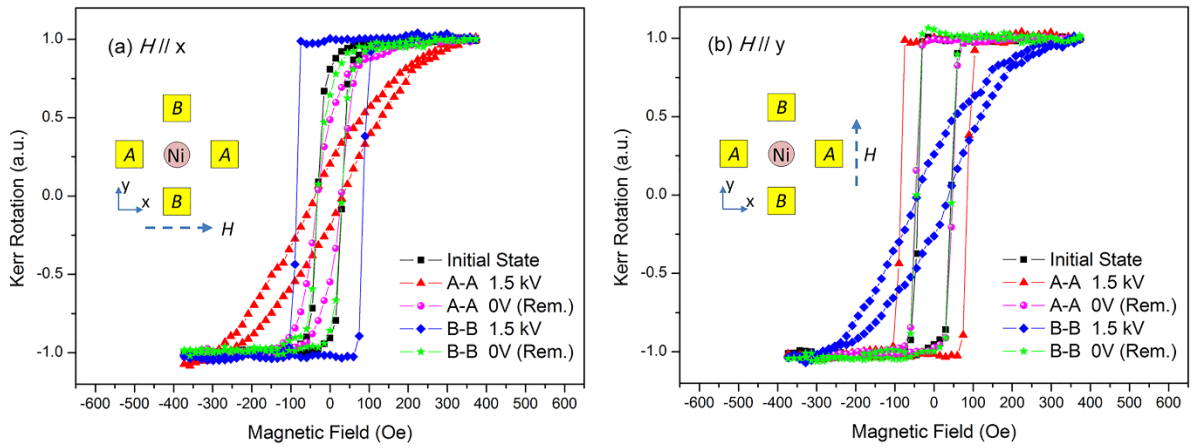

Figure 2.3. Normalized Kerr rotation hysteresis curves (M-H) for L=1.5 mm measured along (a) x-direction with magnetic field along the x-direction and (b) y-direction with magnetic field along the y-direction, with different voltages applied to different electrode pairs.

The experiments were repeated with the electrode spacing reduced to 1 mm. This is the arrangement that produced a larger strain difference in the simulations. The results are shown in figure 2.4. The initial state M-H curves, prior to application of voltage to the electrodes, display a slight asymmetry. When H is applied along the x-axis, there is slightly more rounding at the transition from negative to positive than at the transition from positive to negative. This suggests a preference for the magnetization to align in one direction over aligning 180 degrees from that direction. This effect becomes considerably more pronounced when voltage is applied to electrode pair A-A, shown as "A-A 1.5kV" in figure 2.4(a). When the electrodes are placed closer together, the magnetic field required to approach saturation in the hard axis direction is larger, around 600 Oe. The lack of symmetry in the M-H hysteresis loops is pronounced. Upon removal of the voltage from electrode pair A-A, there is a remnant hard axis in the x-direction and easy axis in the y-direction. The voltage sequence was switched from electrode pair A-A to pair B-B and the magnetic anisotropy was again rotated 90 degrees.

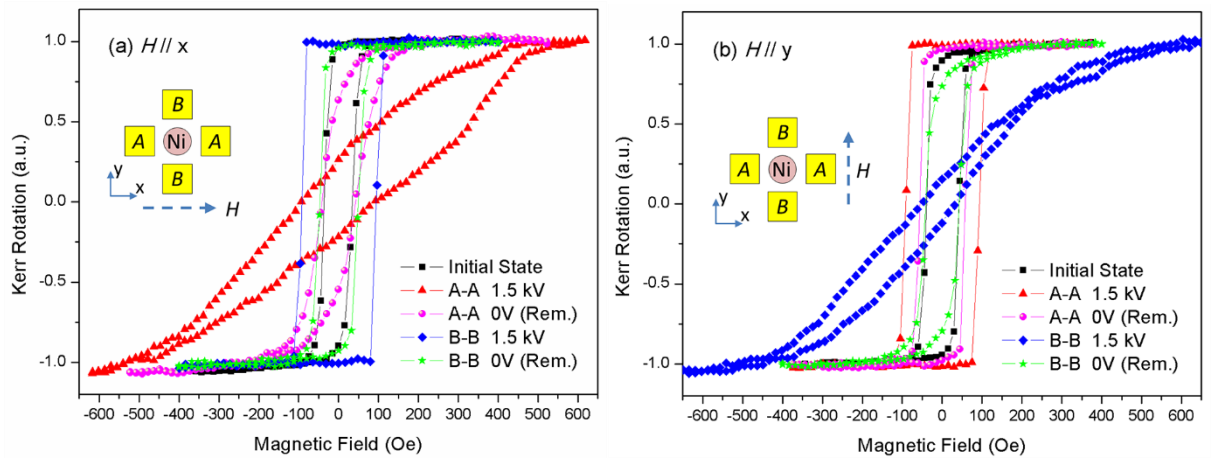

Figure 2.4. Normalized Kerr rotation hysteresis curves (M-H) for L=1 mm measured along (a) x direction with magnetic field along x direction and (b) y direction with magnetic field along y direction, under different applied voltages and for different electrode pairs.

Considering solely the L=1mm case in detail, the change of anisotropy field H_a can be alternated by applying different magnitude of voltage on the electrodes. Figure 2.5 shows the normalized Kerr rotation hysteresis curves (M-H) of the initial state (i.e. no voltage applied) and states with applied voltages on A-A electrodes. Comparing the initial state in figure 2.5(a) and figure 2.5(b), the saturation magnetic field levels were similar along the x and y axes, indicating a lack of preferred easy and hard axes before voltage was applied. The M-H curves for the initial state also showed a large remanent magnetization M_r/M_S =95% in both the x and y directions. When applying voltages of 0.5 kV, 1.0 kV and 1.5 kV on A-A electrodes successively along the x axis, the anisotropy field of the hysteresis curves was increased while the remanent magnetization was decreased, as shown in figure 2.5(a). With 1.5 kV applied, the Ni island displayed a large anisotropy field up to H_a=600 Oe and magnetic remanence as low as M_r/M_S=25%, a 70% decrease from the initial state. These indicate an induced hard axis along the x axis. The M-H curves along the y axis in figure 2.5(b) display an increased coercivity H_c with 100% zero field remanence, indicating an induced easy axis along the y axis. As described in

figure 2.1, applying voltages on A-A induces a bi-axial strain field of ε_{xx}-ε_{yy}>0 between electrodes. Due to the negative magnetostriction of nickel, the bi-axial strain field induces a hard axis along the x axis and an easy axis along y axis. The dependence of anisotropy field H_a and coercivity H_c on applied voltages was observed. Higher voltages (electric field) generated larger strain response on the Ni element, thus inducing increased H_a along x axis (hard axis) and H_c along y axis (easy axis).

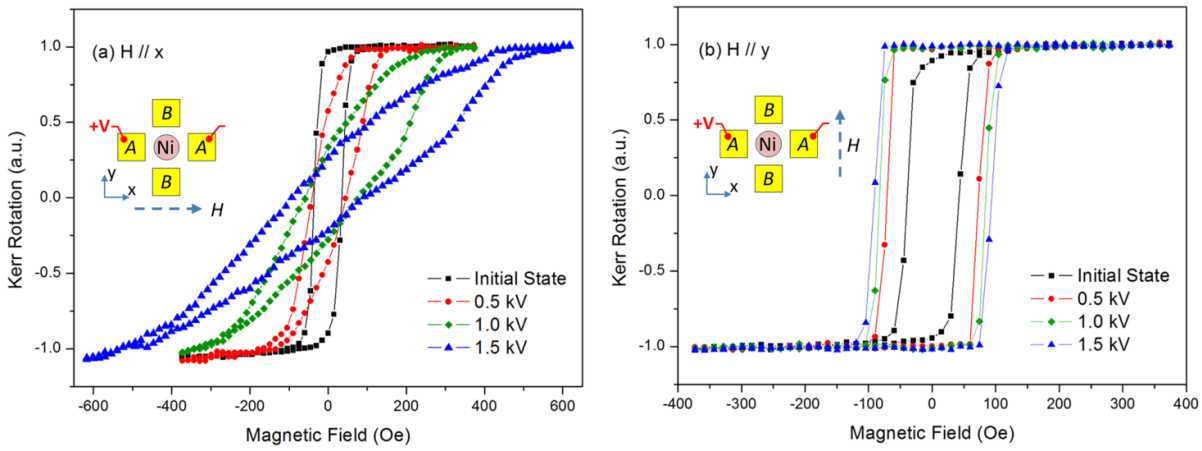

Figure 2.5. Normalized Kerr rotation hysteresis curves (M-H) measured under different applied voltages on A-A electrodes for L=1mm case. (a) M-H along x direction with magnetic field along x direction and (b) M-H along y direction with magnetic field along y direction.

Figure 2.6 shows the M-H curves when voltages are applied on B-B after applying voltages on A-A. In figure 2.6(b), the measured M-H curves between the activated electrodes, i.e. the y axis when applying voltages on B-B, showed an increased anisotropy field (H_a=600 Oe under 1.5 kV) and lowered remanent magnetization M_r/M_S =20% under 1.5 kV, a 75% decrease from the initial state. Higher coercive field H_c curves with 100% remanence were observed along the x axis as shown in figure 2.6(a). The results indicate the y axis became the hard axis and the x axis the easy axis, which is opposite to the A-A electrode case. That is to say, the direction of electric-field-induced magnetic anisotropy was rotated 90 degrees by application of voltage to B-

B instead of A-A. This is because the induced bi-axial strain is ε_{xx}-ε_{yy}<0 which is also rotated by 90 degrees comparing ε_{xx}-ε_{yy}>0 when the A-A electrodes were activated. A similar trend was observed for the voltage dependence of the anisotropy field and coercive field.

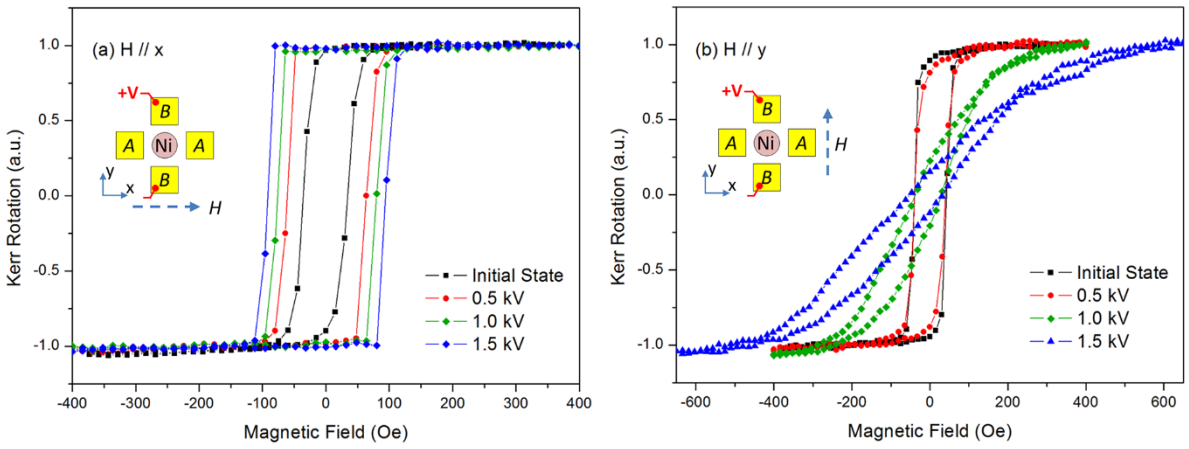

Figure 2.6. Normalized Kerr rotation hysteresis curves (M-H) measured under different applied voltages on B-B electrodes for L=1mm case. (a) M-H along x direction with magnetic field along x direction and (b) M-H along y direction with magnetic field along y direction.

A previous study measured the response of thin film polycrystalline Ni to bi-axial strain.[24] That study included a discussion of the uniaxial degeneracy of the free energy induced by strain that gives rise to symmetric M-H hysteresis loops. The authors of that study pointed out that, based on energy arguments, only the interaction of an applied magnetic field with the magnetization can break the symmetry of the M-H loops. In the experimental results presented above, the asymmetry of the M-H hysteresis loops suggests the presence of a bias magnetic field that was likely induced during processing. Several factors could be producing the initial easy axis, initial hard axis, and asymmetry in the M-H loops including magnetic domain pinning by the ferroelectric domains, irregularity in the shape of the circle, irregular edges in the circular pattern, strain gradients across the Ni, possibly thickness variations in the Ni film, and

possibly a residual magnetization in the Ni sufficiently large that the results represent minor hysteresis loops with a lack of saturation in one direction.

2.4. Discussion

The final goal of this work was to obtain an approximation of the strain from the observed changes in the M-H loops and a compare this to the strain predicted by the linear finite element simulation. To do this, the strain was approximated from the induced magnetic anisotropy. A measure of the anisotropy field H_a (the field needed to saturate the magnetization in the hard direction) was obtained using a linear fit to the slope of the M-H loops between -0.7 and 0.7. The average value of the slopes from each side of each hysteresis loop was extended from the origin to the saturation limit. Using the average reduced the effects of the asymmetry in the M-H loops. The intersection of this line and the $M/M_S=1$(Kerr rotation) line was used as the estimated value of H_a. The same method was used to determine the saturation field H_0 in the initial state to provide both an x-axis and y-axis reference. The measured values of H_a were used to estimate the strain difference based on the known relationship between strain-induced magnetic anisotropy and bi-axial strain.

The equilibrium magnetization can be found from a minimization of the free energy [38] $E_{tot}=E_{zm}+E_{demag}+E_{ex}+E_{mc}+E_{me}$ where E_{zm} is the Zeeman energy; E_{demag} is the demagnetization energy; E_{ex} is the exchange energy; E_{mc} is the magneto-crystalline energy, and E_{me} is the magnetoelastic energy that represents the strain-induced magnetic anisotropy. A first order approximation of the magnetoelastic energy for a cubic crystal structure gives

$$E_{me}(\alpha_i, \varepsilon_{ij}) = B_1[\varepsilon_{xx}(\alpha_1^2 - \frac{1}{3}) + \varepsilon_{yy}(\alpha_2^2 - \frac{1}{3}) + \varepsilon_{zz}(\alpha_3^2 - \frac{1}{3})] + B_2(\varepsilon_{xy}\alpha_1\alpha_2 + \varepsilon_{yz}\alpha_2\alpha_3 + \varepsilon_{xz}\alpha_1\alpha_3) \quad (2.1)$$

where α_i are the direction cosines of magnetization vector and ε_{ij} are the components of the magnetostrictive strain tensor; B_1 and B_2 represent magnetoelastic stress and are functions of magnetostriction constants $\lambda_{<100>}$ and $\lambda_{<111>}$. For Ni thin film, assuming negligible out-of-plane magnetization and shear strain (i.e., $\alpha_3=0$ and $\varepsilon_{xy}=0$) [12], the magnetoelastic energy is simplified to a uniaxial case as

$$E_{me} = K_{me}\alpha_1^2, \text{ where } K_{me} = B_1(\varepsilon_{xx} - \varepsilon_{yy}) \text{ for } \varepsilon_{xx} - \varepsilon_{yy} > 0 \tag{2.2}$$

$$\text{or} \quad E_{me} = K_{me}\alpha_2^2, \text{ where } K_{me} = B_1(\varepsilon_{yy} - \varepsilon_{xx}) \text{ for } \varepsilon_{xx} - \varepsilon_{yy} < 0 \tag{2.3}$$

where the constant terms that do not contribute to anisotropy were dropped. E_{me} is written in two forms for elongation along the x direction (ε_{xx}-ε_{yy}>0) and along y direction (ε_{xx}-ε_{yy}<0). In equations (2.2) and (2.3), B_1=-(3/2) λ_S (C_{11}-C_{22}) for polycrystalline Ni, C_{11}= E(1-ν)/[(1+ν)(1-2ν)] and C_{12}=Eν/[(1+ν)(1-2ν)] where λ_S is the magnetostriction constant [13]; E is the Young's modulus; and ν is Poission's ratio. From equation (2.2) for ε_{xx}-ε_{yy}>0 (tension along x direction)

$$K_{me} = -\frac{3}{2}\lambda_S \frac{E}{1+\upsilon}(\varepsilon_{xx} - \varepsilon_{yy}) \tag{2.4}$$

Normalized magnetization is m= $HM_S/2K_u^{eff}$, where K_u^{eff}= K_u+K_{me} is the effective uniaxial anisotropy constant and K_u is the original uniaxial anisotropy excluding magnetoelastic term[13]. Assuming $H/H_a=M/M_S$=m gives

$$H_a = \frac{2K_u^{eff}}{M_S} = \frac{2(K_u + K_{me})}{M_S} = H_{a0} + \frac{2K_{me}}{M_S} \tag{2.5}$$

where H_{a0} is the anisotropy field of the initial state before voltage was applied. Based on equations (2.4) and (2.5),

$$\Delta H_a = H_a - H_{a0} = \frac{2K_{me}}{M_S} = \frac{-3\lambda_S E(\varepsilon_{xx} - \varepsilon_{yy})}{M_S(1+\upsilon)} \quad , \text{or} \quad (\varepsilon_{xx} - \varepsilon_{yy}) = \frac{-\Delta H_a M_S(1+\upsilon)}{3\lambda_S E} \tag{2.6}$$

From similar derivations, equation (2.3) for ε_{xx}-ε_{yy} <0 (tension along y direction) leads to

$$(\varepsilon_{yy} - \varepsilon_{xx}) = \frac{-\Delta H_a M_S(1+\upsilon)}{3\lambda_S E}, \text{ or } (\varepsilon_{xx} - \varepsilon_{yy}) = \frac{\Delta H_a M_S(1+\upsilon)}{3\lambda_S E} \tag{2.7}$$

Equations (2.6) and (2.7) describe the relation between ΔH_a and bi-axial strain (ε_{xx}-ε_{yy}). The material constants for polycrystalline Ni used here are: E=200 GPa, ν=0.31, λ_S= -34×10^{-6} and M_S=485 emu/cc.

Figure 2.7 is a plot of the bi-axial strain under the Ni disc calculated using equations (2.6) and (2.7) based on the experimentally measured ΔH_a compared to the FEA results. For both electrode spacings the measured ΔH_a and the calculated strain increased with increasing applied voltage. The smaller electrode spacing always had a larger ΔH_a and strain response. Some hysteresis was observed in the strain response. When 1.5kV was applied to A-A for the larger spacing (L=1.5 mm), ΔH_a increased by 207 Oe (ε_{xx}-ε_{yy}=644 ppm). When 1.5 kV was applied to B-B directly after voltage was applied to A-A, the B-B bi-axial strain ε_{xx}-ε_{yy} =-548 ppm (ΔH_a =176.0 Oe) was smaller in magnitude than the previous strain response for A-A. A possible explanation is that the remnant strain from a previous voltage on (A-A) decreased the strain response of successive voltages on (B-B) because a small remnant strain associated with voltage on (A-A) must first be counteracted. The maximum ΔH_a of 414.1 Oe measured in the L=1.0 mm case for 1.5 kV corresponded to a calculated bi-axial strain of 1290 ppm. The linear FEA simulation closely approximates the strain response determined from ΔH_a. The good agreement between experimental measurements and simulations suggests that the assumptions in the FEA

model and the equation used to compute strain from ΔH_a were reasonably representative of the real material behavior.

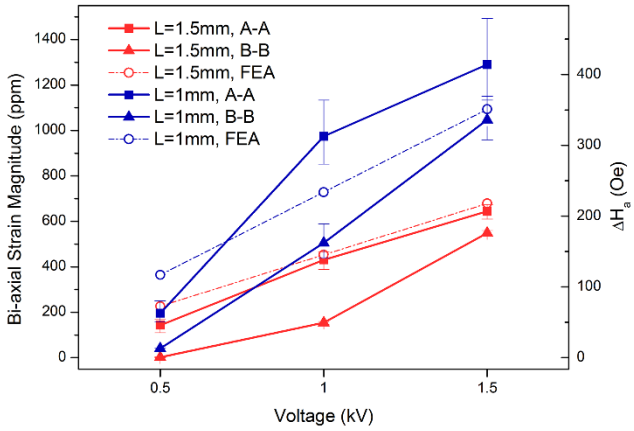

Figure 2.7. Magnitude of bi-axial strain response (left ordinate) and ΔH_a along the hard axis (right ordinate) as a function of applied voltage for various electrode pairs and spacings. FEA simulations are indicated by the dot-dashed lines.

2.5. Conclusion

A method was developed that uses patterned electrodes on a piezoelectric substrate to generate a localized strain in a piezoelectric plate. This strain was used to control magnetic anisotropy in a 35nm thick and 0.5 mm diameter Ni island. The bi-axial strain response was consistent with that predicted using linear piezoelectric FEA simulations. This method may be suitable for next generation MRAM devices with low writing energy and fast writing speed. This approach has the potential to be scaled down to the micro or nano-scale and used to achieve local in-plane strain on the surface of thin piezoelectric films subject to substrate clamping.

Chapter 3. Controlling individual micron-sized Ni rings on thin film PZT

3.1.Literature review

Manipulating magnetization at the micro- and nanoscale has been studied extensively for next-generation computer memory, nanoscale sensors, and spintronic devices.[1], [47] Magnetization can be controlled by magnetic field[38], spin-polarized current injection[48], exchange-bias[49], [50], interface-charge-driven magnetoelectric (ME) effect[51], [52], strain-mediated ME effect[4], [5], [27], and ferroelectric/ferromagnetic coupling in single phase multiferroics[50]. The use of strain-mediated approach to control magnetization is attracting increasing attention due to its promising low energy consumption, large coupling coefficient, and the wide availability of piezoelectric/magnetoelastic materials[3], [4]. Previous research has demonstrated magnetization manipulation of nanoscale ellipses[5], squares[53] and ring[29] structures using bulk piezoelectric substrates. Bulk piezoelectric substrates switch all elements at once[5], require high voltage, are semiconductor incompatible, and are rate limited by elastic wave velocities through the thickness; all of these challenges must be overcome for magnetoelectric device design.

Compared to bulk piezoelectrics, piezoelectric thin films require much smaller voltage to obtain similar magnitude of electric field ($E=V/d$, where V and d refers to applied voltage and thickness of piezoelectrics, respectively). The thickness mode response time becomes shorter as the thickness is decreased ($\tau=d/c$, where d is the film thickness and c is the bulk acoustic wave velocity; for a 1 micron thick film with c=4000 m/s the thickness mode response time is on the order of 0.25 ns). Thin film piezoelectrics have much smaller device volume, reducing the energy required to drive the combination of piezoelectric strain and magnetization reorientation

needed for nanoarchitected magnetoelectric devices. Furthermore, piezoelectric films are used in a range of MEMS devices.[54], [55] Few researchers have reported using thin film piezoelectrics to alter magnetization of nanoscale magnetic elements. Chung et al[32] reported magnetic domain evolution using a fully electroded lead zirconate titanate (PZT) thin film when voltage was applied. However, this approach did not offer the ability to control individual nanoarchitected magnetoelectric elements. To date, this capability has been lacking.

Achieving local control of individual magnetoelectric structures on a piezoelectric thin film is a challenging problem. Piezoelectric thin films are fully clamped in-plane by the substrate. This dramatically reduces the effective piezoelectric coefficient[56] and hence restricts its capability of generating enough strain for controlling magnetization. To reduce the clamping effect, researchers reported etching PZT film into discrete islands.[57], [58] However, this complicated fabrication process may limit its applications. We present a concept using electrode pattern design to control in-plane magnetoelastic anisotropy by creating a highly localized strain at the surface of a piezoelectric thin film subject to substrate clamping. Finite element simulations (FEA) were used to design the electrode pattern and the magnetic element. These devices were fabricated and the magnetic domain pattern in the Ni ring was shown to change in response to the induced localized strain.

3.2.Electrode pattern design

A conceptual schematic of the technique is presented in figure 3.1(a), derived from previous research by Cui et al.[59] The structure consists of a Si wafer substrate (not shown), a bottom electrode, a PZT thin film, and, in this case, three pairs of electrodes surrounding a middle magnetic element. When voltage is applied to one pair of top electrodes (A-A, B-B or C-

C) while the bottom electrode is grounded, the piezoelectric material underneath each electrode expands out-of-plane (d_{33} effect) and contracts in-plane (d_{31} effect), creating a highly localized strain field under each electrode and in their immediate vicinity. When two such electrodes are in close proximity, the strain fields surrounding the electrodes interact and an in-plane bi-axial strain field is induced between the electrodes (tensile along the axis connecting the electrodes and compressive in the orthogonal direction). Figures 1(b)-1(d) show the average principal strain field between electrodes when voltage is applied to the A-A, B-B and C-C electrodes, respectively. Considering Ni as an example (negative magnetostriction), this principal strain field induces magnetoelastic anisotropy with the easy axis aligned with the compressive strain direction[38]. Hence, in the conditions shown in figure 3.1(b)-(d), three different in-plane magnetoelastic anisotropy directions can be achieved by applying voltage to each of the three different pairs of electrodes (A-A, B-B or C-C). In this ideal case, the three pairs of electrodes spaced 60º apart are sufficient to deterministically manipulate magnetization of magnetic elements.

The magnitude of the induced bi-axial strain in the structure when voltage is applied was approximated using linear piezoelectric FEA simulations.[59] The piezoelectric coefficients and dimensions used in the simulations were d_{33}=70 pC/N, electrode dimension 0.6×0.6 μm^2, electrode separation distance 1.4 μm, PZT thin film thickness 1.0 μm, applied voltage 25 V. In the simulation the bottom surface of the PZT thin film was fixed to simulate the clamped substrate boundary condition. The simulations (results not shown) indicated that approximately 1200 ppm average biaxial strain (principal strain ε_x-ε_y>0) can be generated between the electrodes. A micromagnetic model[60] based on the Landau-Lifshitz-Gilbert (LLG) equation including magnetoelastic coupling implemented in a finite element framework was used to

design Ni ring elements with a domain structure that responds to this level of strain. Figure 3.1(e) shows the simulation results for a Ni ring with 1000 nm outer diameter, 700 nm inner diameter and 15 nm thickness. In the simulations, the Ni ring of this geometry formed the "onion" state[61] when magnetization was initialized at θ=-30º direction. The black and white regions on the ring are the position of two 180º head-to-head domain walls where there is an out-of-plane magnetization component. When the 1200 ppm biaxial strain was applied in the θ=30º direction (the direction of biaxial strain is defined by the direction of the compressive strain), the ring magnetization rotated counterclockwise by 60º and aligned with the compressive strain direction. When strain was unloaded, the magnetization stayed at the new position (θ=30º). Hence, if the Ni ring is initialized along θ=-30º direction, the application of 25 V to the A-A electrodes generates strain that rotates the magnetization from θ=-30º to θ=30º. Similarly, starting from the magnetization along θ=+30º and applying 25 V to the C-C electrodes as shown in figure 3.1(d), the simulation result indicate that the magnetization should rotate to the θ=+90º direction (along the compressive strain). Starting from the magnetization along θ=+30º and applying 25 V to the B-B electrodes as shown in figure 3.1(c), simulation results indicate that the magnetization rotated back to the θ=-30º direction. Hence it is possible to deterministically control the magnetization direction of the "onion" domain state in a 1000 nm diameter Ni ring.

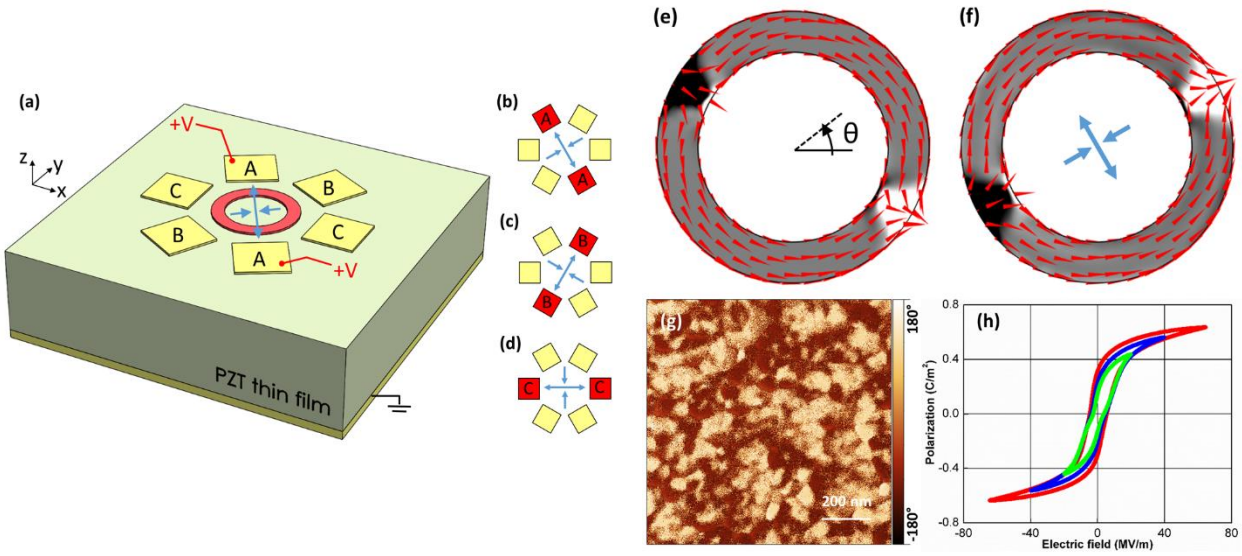

Figure 3.1. (a) Schematic of a device structure that can create magnetoelastic anisotropy on magnetic elements (a ring is shown as an example) in three directions by applying voltage on (b-d) A-A, B-B or C-C electrodes. Blue arrows illustrate the average principal strain direction between electrodes for each case with the outward pointing arrows indicating the tensile strain and inward pointing arrows indicating the compressive strain directions. (e) Results of a micromagnetic simulation of a 1000 nm outer diameter, 700 nm inner diameter and 15 nm thick Ni ring initialized along θ=-30º direction by an applied magnetic field. The red arrows indicate the local in-plane magnetization direction. Grayscale color indicates the local out-of-plane magnetization. (f) Results of a micromagnetic simulation of a Ni ring subject to a 1200 ppm biaxial strain with the tensile and compression direction indicated by blue arrows. (g) A piezoelectric force microscopy (PFM) phase image of the PZT thin film. (h) A polarization versus electric field (P-E) loop of the PZT thin film.

The resulting design was fabricated on a chemical solution deposited 1 µm thick $PbZr_{0.52}Ti_{0.48}O_3$ film on 100 nm Pt (bottom electrode)/40 nm ZnO/400 nm SiO_2/Si substrate. Details of the preparation process of this film are given in a previous publication.[62] The piezoelectric force microscopy (PFM) image in figure 3.1(g) shows a clear piezoelectric response, highlighting out-of-plane piezoelectric phase. An effective piezoelectric constant of the film of $d_{33,e}$= 49.2 pC/N was measured by PFM. Because $d_{33,e}$ is measured on a clamped film, it is lower than the actual piezoelectric constant d_{33} of the film.[56], [63] Hence in the piezoelectric FEA simulations, the stress free piezoelectric constant was estimated to be d_{33} = 70 pC/N (about

40% higher than $d_{33,e}$). The root-mean-squared surface roughness of the film was R_q = 1.35nm. The polarization versus electric field (P-E) hysteresis loop in figure 3.1(h) shows that the electrical coercive field is about 5 MV/m. The electric breakdown value of the film is about 70 MV/m. The electrode patterns and magnetic Ni ring structure were defined using a two-step e-beam lithography process. Electrodes of 5 nm Ti and 100 nm Au were deposited by e-beam evaporation. By the same technique, 3 nm Ti and 15 nm Ni were deposited, followed by 2 nm Al as a capping layer protecting the Ni from oxidation. The size of the electrodes, electrode separation distance and Ni ring geometry were identical to the parameters used in the FEA simulation.

3.3. Experiment result

Figure 3.2(a) is an atomic force microscopy (AFM) image of the fabricated device showing the Ni ring structure and three pairs of electrodes on the PZT thin film. Magnetic force microscopy (MFM) was used to determine the magnetization configuration of the Ni ring structure. It is challenging to image soft magnetic material (such as Ni) elements under MFM due to the tip stray field.[64] However, several previous studies have acquired MFM images on Ni micro- and nano-structures by carefully choosing tip coating, operation mode, and parameters[29], [65]. A low moment tip (MESP-LM, Bruker) was used and the tip lift height during the measurement was 40 nm. At least two images were recorded in the same condition with different scanning directions. If there was a clear difference between them (which came from undesired tip-sample interaction), the images were discarded. Figures 2(a) and 2(c) show AFM and MFM images of the as-fabricated device. The nickel ring displays the PZT surface roughness, i.e. humps and grooves of the PZT grain structure, as seen in figure 3.2(b). As MFM

measures the magnitude of out-of-plane magnetization, the “onion” state of the Ni ring can be identified as black and white spots in the MFM image as shown in figure 3.2(c). 25V was then applied to the B-B electrodes and held for 20 sec. After unloading the voltage, the MFM measurement was again conducted and the result is shown in figure 3.2(d).

The results show that the patterned electrode approach produces sufficient in-plane strain to interact with the magnetization. In MFM images some electrodes are darker than others. This is possibly due to accumulated charge sensed by the MFM tip through electrostatic force. This does not affect the magnetization measurement. There is a change of the domain wall structure seen by comparing figures 2(c) to 2(d). The white spot mostly stayed unchanged, while the black spot was broadened. The broadening direction agreed with the direction of compressive strain (and hence the easy axis of magnetoelastic anisotropy). The arrows in figure 3.2(b) indicate two notches that are physically on each side of the “white” magnetic domain wall. The two notches could be creating a deep energy well that pins the magnetic domains[66]. The observed domain wall broadening (black spot) could be due to the same mechanism, however the local spins further from the notch become aligned with the magnetoelastic anisotropy. Hence the combination of geometric imperfection and applied strain creates an overall effect of broadening the black magnetic domain wall.

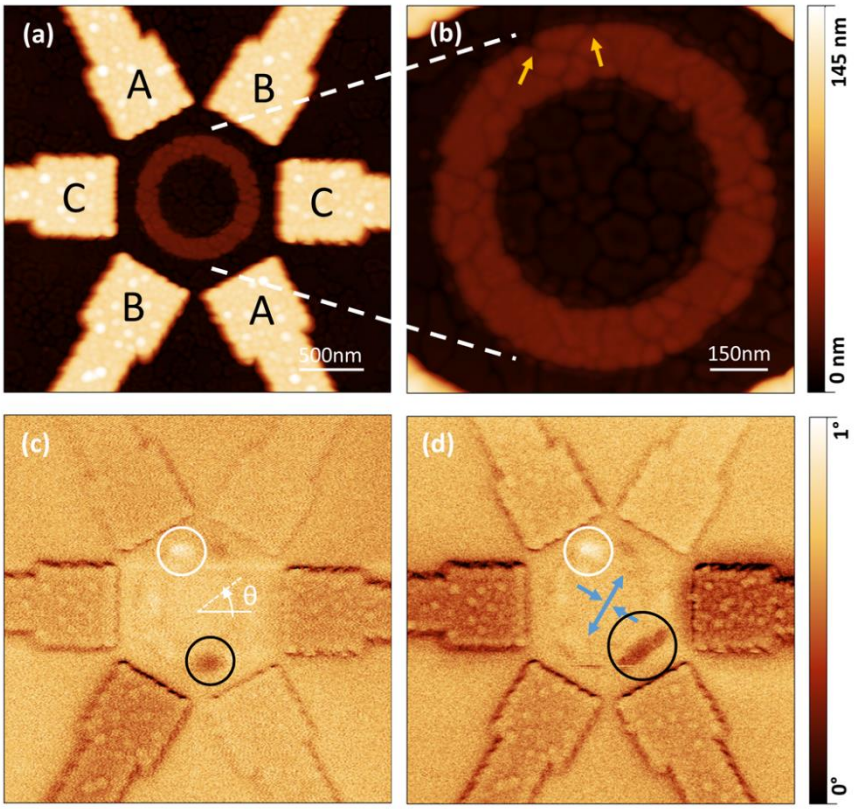

Figure 3.2. AFM and MFM images of the fabricated device with a micron-sized Ni ring surrounded by six electrodes. (a) An AFM picture of the fabricated device with a Ni ring surrounded by patterned electrodes; (b) expanded view of the Ni ring. The yellow arrows indicate the position of two observed notches. (c) An MFM image of the as-fabricated device initialized by an applied magnetic field with two "onion" state domain walls shown as black and white spots (circled); (d) after applying 25 V to the B-B electrodes one magnetic domain has moved and spread (black circle). The blue arrows indicate the direction of average principal strain induced by the applied voltage.

Figure 3.3(a) shows the as-fabricated AFM images of a second fabricated device. The black and white spots in the MFM image are not perfectly symmetric, suggesting the magnetic domain walls might be trapped in local energy wells associated with geometric imperfections. Figure 3.3(b) shows the surface profiles of a Ni ring structure (profiles 1 and 3) and PZT thin film (profiles 2 and 4). Surface profiles for both Ni and PZT have about 6nm peak-to-peak variation, showing that the Ni layer carried the topography from the PZT layer, which may affect the in-plane magnetization and induce magnetic domain wall pinning. Figure 3.3(c) is the MFM

image of the as-fabricated device. 25V was applied to electrode pair A-A and held for 20 seconds. After unloading the voltage, the MFM image shown in figure 3.3(d) was taken. The white domain wall (highlighted in the dashed circle) shows a counterclockwise rotation from $\theta \approx -30^{o}$ to $\theta \approx 0^{o}$, while the black domain wall displays no significant motion. We note that in concept the white domain should align with the compressive strain direction at $\theta \approx 30^{o}$ direction, yet does not move that far. The reduced rotation is attribute to a notch seen at $\theta \approx 0^{o}$ in the AFM image (see arrows in figure 3.3(a)). We then applied 25 V to the B-B electrodes and kept the voltage on for 20 seconds. Upon removal of the voltage the MFM image was taken and shown in figure 3.3(e). The white domain wall rotated clockwise back to $\theta \approx -30^{o}$ aligned with the compressive strain direction. As seen in figures 3(c)-3(e), the magnetic domain structure of a Ni ring was rotated forward and backward using patterned electrodes on a fully clamped PZT thin film.

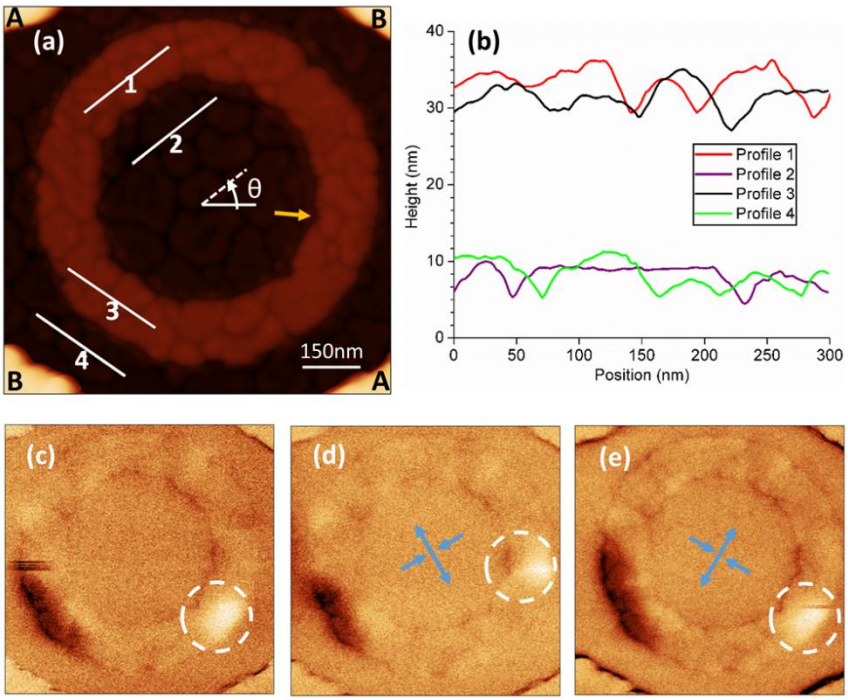

Figure 3.3. AFM and MFM images of the second fabricated device with a micron-sized Ni ring surrounded by six electrodes. (a) An AFM image of the second fabricated device. The yellow arrow indicates the position of an observed notch. (b) The height of the profiles corresponding to the four lines shown in (a). Note that the lines on the Ni ring are offset by the Ni thickness. (c) An MFM image of the as-fabricated Ni ring; (d) one domain wall (circled) has moved after applying 25 V to the A-A electrodes; (e) the same domain wall (circled) has moved back to its original position after applying 25 V to the B-B electrodes. The blue arrows indicate the direction of average principal strain induced by the applied voltage.

The observations above indicate that the domain walls become pinned by edge imperfections in the ring structure. These imperfections were the result of interaction of the lithography with the surface roughness of the columnar grain structured PZT thin film. Finite element based micromagnetic simulations were run to explore the interaction between the notches and a ring's domain structures. The notch was represented by a semi-ellipse with 50 nm major and 30 nm minor axes. This is about the size of the notch observed in figure 3.3(a). Figure 3.4(a) shows the geometry simulated with the notch on the inner diameter circled. When initialized along the θ=-30º direction, the Ni ring formed the "onion" state domain structure as

shown (two 180° domain walls). 1200 ppm biaxial strain with compressive strain along θ=30º direction was applied as illustrated by the blue arrows in figure 3.4(b). The black domain wall rotated clockwise by 60º and aligned with the compression direction, but the white domain wall stopped at the θ=0º direction, pinned by the notch. The simulation shows that the existence of the geometrical notch creates a local magnetic energy minimum that can pin the domain wall.

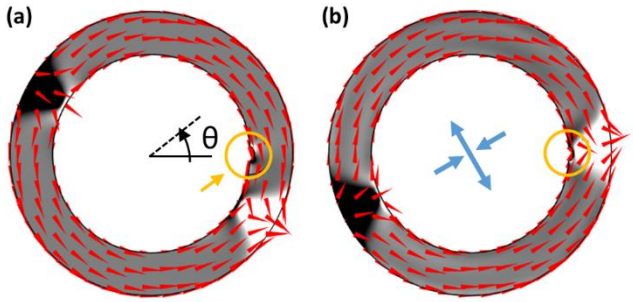

Figure 3.4. The results of a micromagnetic simulation of a 1000 nm outer-diameter, 700 nm inner-diameter and 15 nm thick Ni ring with a notch (semi-ellipse with 50 nm long axis and 30 nm short axis) at θ=0º position. The magnetization distribution is shown (a) when initialized along θ=-30º direction and (b) after applying 1200 ppm bi-axial strain with the strain direction shown as blue arrows. The magnetic domain wall (white spot) has been pinned by the notch. The red arrows indicate the in-plane magnetization direction. Grayscale color indicates the out-of-plane magnetization.

Two examples were presented from a large array of devices that were fabricated, all with same electrode pattern and Ni ring structure. In all cases the patterned electrodes on the clamped PZT film produced sufficient strain to change the magnetic domain pattern. The domain wall structures changed by the strain field are the result of minimization of the magnetoelastic anisotropy and the shape anisotropy contributions to the free energy.[38] In most cases only one magnetic domain wall (white or black spot in MFM image) moved in response to the applied voltage. Due to magnetic domain pinning, we were not able to achieve continuous 180° magnetization rotation by applying a voltages on A-A, B-B, C-C, consecutively. In an attempt to reduce the surface topography effect, 25nm thick Ni rings were produced with exact same

geometry (1000nm outer-diameter, 700nm inner-diameter) on the same batch of PZT film. In the 25nm thick Ni devices similar magnetic domain rotation was observed after voltage was applied and the pinning effect did not appear to be reduced. This suggests that the edge imperfections may be contributing more to the pinning than the surface roughness. The PZT topography is mostly from grain boundary grooving, which is intrinsic for sol-gel prepared films. Possible methods to smooth the film surface include liquid phase coatings that are smoothed by surface tension, or pulsed layer deposition (PLD) prepared epitaxial PZT films.

The experiment was repeated with the thickness of Ni ring element increased from 15nm to 25nm, while keeping all other experiment parameters unchanged. Since the peak-to-peak surface roughness value of the PZT thin film is 7-8nm, fabricating a thicker Ni ring structure may mitigate the magnetic pinning effect due to non-flat surface. Figure 3.5 shows the experiment result of a fabricated device. As seen in figure 3.5(a), clear geometric imperfections were still present, especially along the edge of the ring structure. Figure 3.5(b) and (c) shows the MFM characterization before and after applying voltage on electrode pair B-B. It is shown that only the white magnetic domain was moved towards the compressive strain direction. The black domain was pinned, possibly due to imperfect geometry. The device performance of this 25nm Ni ring structure in response to applied voltage is similar with the one with 15nm thick. This means that simply increasing the thickness of the Ni structure cannot effectively attenuate the undesired magnetic pinning effect.

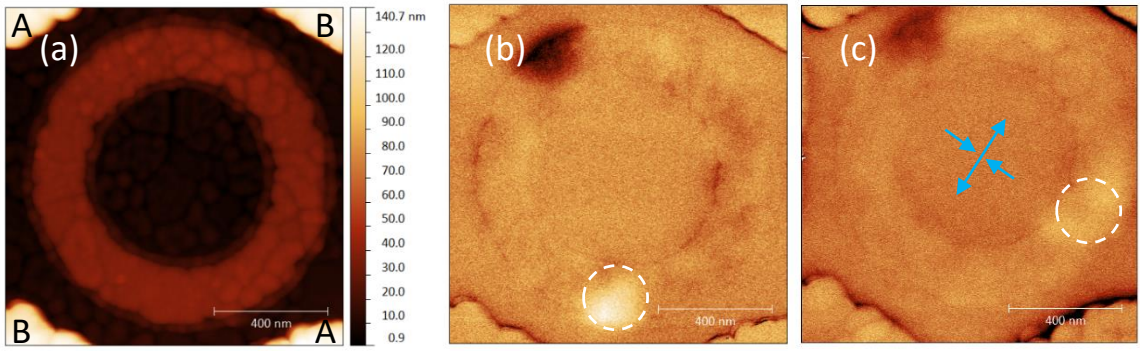

Figure 3.5. AFM and MFM images of a fabricated device with a 1um OD, 700nm ID and 25nm thick Ni ring structure. (a) AFM image of the fabricated device with 6 pattern electrodes (4 shown) with the middle Ni ring. MFM images of the Ni ring structure (b) as-fabricated, (c) after applying voltage on B-B electrodes. The blue arrows indicate the direction of average principal strain induced by the applied voltage.

A 1 micron thick epitaxial PZT thin film deposited by PLD was characterized by AFM and PFM for surface topography and piezoelectric response. This specimen was deposited on a simple crystal $SrTiO_3$ substrate with $SrRuO_3$ bottom electrode. The characterization results were shown in figure 3.6. The AFM image clearly shows the surface topography related to the crystalline orientation of the epitaxial thin film. This indicates that the PZT thin film is highly crystalized. Figure 3.6(c) demonstrates the height profile of the PZT thin film corresponding to the line drawn in figure 3.6(a). The peak-to-peak roughness value of this epitaxial PZT is still about 7-8nm in long range. The size of the piezoelectric domain structures is around 1um. Within each domain, the surface roughness peak-to-peak value is only about 1-2nm. Between different piezoelectric domains, there is a sharp change about 7-8nm on height due to different material crystalline orientations. If a Ni ring structure can be deposited on top of a single piezoelectric domain, avoiding the sharp height change from piezoelectric domain walls, the Ni structure will be landed on surface with optimized surface roughness. Figure 3.6(b) is the PFM image of the film. Piezoelectric domains in different shapes were present. This is possibly due to

the residual strain coming from the deposition process. The high contrast of the PFM image indicates the high piezoelectric response of the PZT thin film.

The material property of the PLD deposited PZT structure is not isotropic. Along different crystalline directions, the piezoelectric constant of the epitaxial film is different. This can be troublesome for electrode pattern designs. With anisotropic piezoelectric material property, by applying the same voltage on the electrode pairs along various directions, different strain fields can be produced. Sol-gel prepared PZT thin film is isotropic in-plane and does not have this issue. A detailed study is needed to simulate the strain field generated by patterned electrodes on this epitaxial PZT thin films.

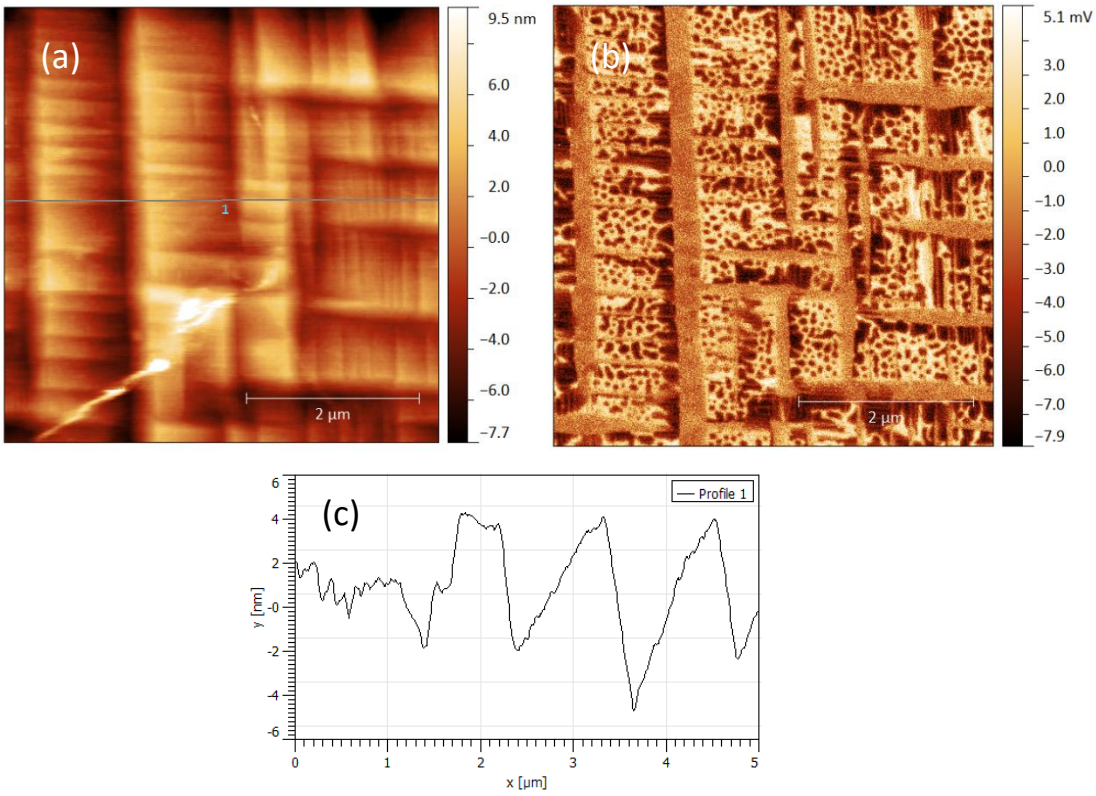

Figure 3.6. AFM, PFM and surface profile characterization for a 1 micron thick PZT thin film deposited by PLD. (a) AFM image showing clear crystalline structures from PZT. (b) PFM

images shows piezoelectric domain in different formats. (c) Height profile of the horizontal line in (a).

3.4. Conclusion

In this section it was demonstrated that the use of patterned electrodes can overcome the clamping effect of the substrate in PZT films grown on Si. The resulting in-plane strain was demonstrated to be sufficiently large to interact with the magnetization of Ni rings. The elements were designed using a finite element based micromagnetics code. Geometric imperfections arising from the PZT surface topography were observed to interact with the domain wall motion and pin the domain walls. The patterned approach is applicable to many nanoscale strain-mediated magnetoelectric devices. The electrodes can be in different shapes as long as one of the dimensions is comparable to the film thickness. The magnetic structures can be placed on top of square electrodes to obtain bi-axial compressive strain, on top of line electrodes to obtain uniaxial compressive strain, or between two line electrodes to obtain uniaxial tensile strain. The electrodes themselves can even be the magnetic material. This capability opens a design space for nanoarchitected magnetoelectric devices.

Chapter 4. Architecting the geometric shape of nanomagnets in strain-mediated multiferroic heterostructure

4.1. Literature review

In this chapter, we present shape anisotropy based designs of nanomagnets that can achieve 180° deterministic magnetization rotation driven by piezoelectric strain through the strain-mediated magnetoelectric (ME) effect, like magnetic ratchets. The design process led to two novel shapes, “peanut” and “cat-eye”, which are discussed in detail. The ME effect is attracting considerable research interest due to its low energy consumption and high coupling coefficient relative to other magnetization control methods such as applying magnetic field and spin-polarized current injection.[3], [4] ME driven nanomagnets (nanoscale magnetic elements) can store bit information without any standby power dissipation, offering unprecedented power efficiency, and thus have high potential for implementation in the next generation of spintronic devices.[47], [67] Magnetic anisotropy, an effect with multiple contributions including strain, shape and crystalline structure; determines the degree to which the magnetization direction produces a minimum free energy.[38] The geometric shape of nanomagnets influences the magnetization distribution through magnetic shape anisotropy. This effect can be used to create a controllable magnetic domain pattern that dominates the dynamic magnetic response.[68] Previous research has experimentally and computationally explored the magnetic shape anisotropy of nanomagnets in highly symmetric shapes, like circles, ellipses, polygons,[36] rings,[61], [69] and even some uncommon shapes like Reuleaux triangles[70]; with emphasis on their integration into device designs. For example, magnetic non-volatile memory and magnetic logic elements have used single domain nanomagnets with bi-stable magnetization states in

elliptical[5], [71], [72] and quadrilateral[4], [73] shapes with two-fold symmetry. Ferromagnetic rings with geometric center-symmetry have been used in studies of fundamental magnetization behavior such as domain wall trapping[74] and domain wall velocity[75], and have also been proposed for applications like computer memory[76] and nanoscale particle delivery systems[30], [77]. Optimizing the shape of nanomagnets provides an opportunity to significantly improve their functionality. Since magnetic shape anisotropy relates the geometric shape of the nanomagnets to their magnetic behavior, the shape can be tailored to obtain the magnetic anisotropy required for specific applications.

Manipulating magnetization through the strain-mediated ME effect presents challenges when the goal is to achieve 180° magnetization rotation. Magnetic field, a *directional* vector effect, can induce a 180° magnetization switching of a single domain nanomagnet, when applied opposite to the original magnetization direction. However, strain cannot easily induce such 180° full magnetization switching. Considering solely the strain-induced magnetic anisotropy, the strain, a *uniaxial* effect, can induce at most a 90° reorientation of the magnetization vector.[6] Achieving a full 180° magnetization rotation using strain has been considered a "fundamental challenge".[7] Previous researchers achieved strain-mediated electrically driven 180° magnetization switching in single domain nanomagnets on a piezoelectric substrate using magnetocrystalline anisotropy (MCA)[78], dynamic magnetization precession[79]–[81], a four-electrode design on a piezoelectric requiring application of two different stain fields[59], [82], a flower-shaped nanomagnet also requiring application of two different strain fields[7] and a square-shaped nanomagnet with a bias-field-induced uniaxial magnetic anisotropy[83]. A multi-electrode design creating localized strain in a piezoelectric is a possible method to force a 180° magnetization reorientation of a magnetic ring in the "onion" state with two head-to-head

domain walls.[84]–[86] All of these approaches involve breaking uniaxial symmetry using either special material properties, e.g. MCA from epitaxial magnetic materials; or complicated device design, e.g. applying piezostrain several times in different orientations to complete a full 180° rotation; and thus complicate the fabrication process.

The novel "peanut" and "cat-eye" architected geometric shapes offer the ability to produce 180° magnetization reorientation by applying *a single piezostrain pulse*. Applying the same strain field again induces a second 180° magnetization rotation, resulting in a complete 360° rotation. The design takes advantage of magnetic shape anisotropy and can be implemented using any magnetostrictive thin films. The "peanut" and "cat-eye" were designed as a simple two-terminal device with a voltage-controlled piezoelectric substrate. In both designs the magnetization only rotates clockwise (CW) and thus forms a magnetic ratchet. We present these two designs separately. In each case we begin with the shape architecting process. This is followed by strain coupled micromagnetics simulations that were used to characterize the magnetic behavior in response to piezoelectric strain.

4.2."Peanut" shaped nanomagnets

The "peanut" shaped nanomagnet was developed as a single domain magnetic element that can achieve deterministic 180° magnetization reorientation controlled by electric-field-induced strain on a piezoelectric substrate. For a typical uniaxial nanomagnet, like an ellipse, strain-mediated magnetization control is not deterministic. Polycrystalline Ni (with zero volume average MCA) is the magnetic material used in the design unless noted otherwise. A thin-film magnetic element with all three dimensions on a nanometer length scale (about <300nm in lateral size and <50nm in thickness for Ni) forms an in-plane single domain in ground state.[5], [87] A

single domain circular nanomagnets does not have in-plane shape anisotropy because all in-plane magnetization directions are geometrically identical.[88] For an elliptical shaped nanomagnet, the magnetic easy axis (EA) and hard axis (HA) are perpendicular to each other, aligning with the geometric major axis and minor axis, respectively.[38] This is due to the magnetic shape anisotropy: the demagnetization field is much larger along the minor axis than along the major axis. Applying a piezoelectric biaxial strain field to the ellipse, compressive strain along one direction and tensile strain in the perpendicular in-plane direction, we can induce a new EA through the magnetoelastic effect.[38] For a material like Ni with negative magnetostriction, the strain-induced EA aligns with the compressive strain direction. If sufficient compressive strain is applied along the original HA direction (geometric minor axis), the magnetization is forced to rotate by 90° from its original EA to this new strain-induced EA (geometric minor axis). When the piezoelectric strain is released, the magnetization rotates back to its original EA (geometric major axis). There is an equal probability of the magnetization rotating toward the original direction or in the opposite direction due to the symmetry. This leads to a total of 0° or 180° magnetization switching, respectively.[5] Hence, for geometric shapes like an ellipse, with the EA and HA perpendicular to each other, the strain-mediated electrically driven magnetization switching process is not deterministic.

Magnetic anisotropy can be induced resulting in a non-perpendicular EA and HA relative orientation. This enables 180° deterministic magnetization rotation in response to piezoelectric biaxial strain.[83] The mechanism is described with reference to figure 4.1. Before applying piezostrain, the magnetization aligns with the EA shown as the solid red arrow along the blue EA as shown in figure 4.1(a). When sufficient piezoelectric biaxial strain is applied (green arrows), the strain-induced new EA and HA are aligned with the compressive strain and tensile strain

direction, respectively. Hence the magnetization will rotate CW away from the tensile strain direction towards the compressive strain direction, as the dashed red arrow in figure 4.1(a) shows. After the piezostrain is released, the magnetization reorientation is governed by the original EA and HA, causing the magnetization to rotate away from the original HA and align with the EA, as shown in figure 4.1(b). Hence with this type of magnetic anisotropy, applying and releasing piezoelectric biaxial strain can induce a 180° deterministic CW magnetization rotation. Similarly, starting from figure 4.1(b), applying the same strain field will result in the magnetization again rotating CW with the magnetization aligned with the compressive strain direction, as shown in figure 4.1(c). Releasing the applied piezostrain, the magnetization rotates CW again towards its original EA, moving back to its original direction. This is a second 180° CW magnetization rotation, and in total a 360° CW magnetization rotation can be achieved by applying the same piezoelectric strain field twice. Note that the magnetization can never rotate counterclockwise (CCW) in response to piezostrain with this geometry. A nanomagnet with such magnetic anisotropy has the ability of achieving strain-mediated electrically driven deterministic 180° magnetization rotation.

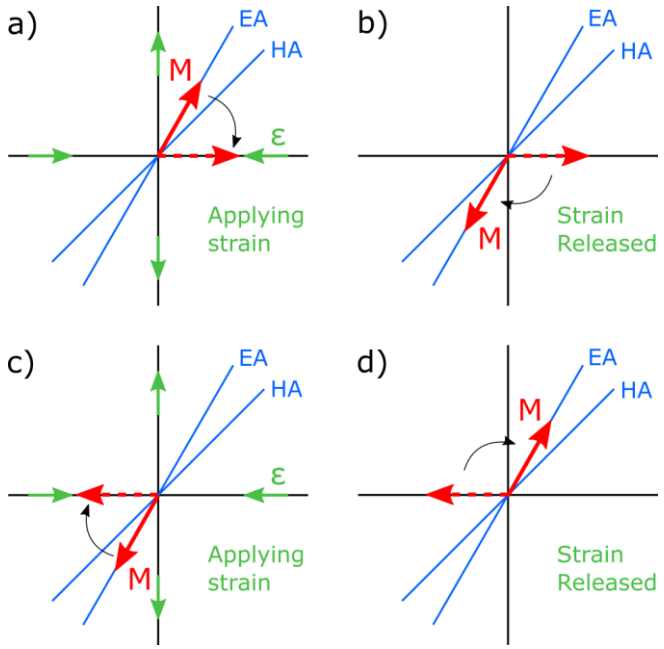

Figure 4.1. The target magnetic anisotropy with the ability of achieving 180° strain-mediated magnetization rotation under a single piezostrain actuation. (a and c) Magnetization (red arrow) rotates away from the EA towards compressive strain direction in response to piezoelectric biaxial strain, crossing over the HA. (b and d) Magnetization rotates to the new direction along EA when the strain is released. From (a) to (b) and from (c) to (d), magnetization is rotated 180° CW by applying piezostrain once. From (a) to (d), magnetization is rotated 360° CW in total by applying the same strain field twice.

The "peanut" shaped nanomagnet was engineered with the magnetic anisotropy described above. The mechanism bridging geometric shape of an ellipse and its magnetic anisotropy is: magnetic EA and HA follow geometric major and minor axes, respectively. In figure 4.2(a), the ellipse is divided into four quadrants separated by major and minor axes, colored according to quadrant. Starting with an ellipse, we then rotated the major and minor axes to change the angle between the magnetic EA and HA. This produced the shape shown in figure 4.2(b). The four parts of the outer boundary separating major and minor axes corresponds to the four quadrants with same color in figure 4.2(a). This new shape is referred to as "peanut" due to geometric similarity. Figure 4.2(c) demonstrates the layout of a strain-mediated ME device incorporating the "peanut" shaped nanomagnet. Single crystal <011> cut $[Pb(Mg_{1/3}Nb_{2/3})O_3]_{0.66}$-$[PbTiO_3]_{0.34}$

(PMN-PT) is used as piezoelectric substrate. Applying voltage across the substrate thickness induces compressive strain and tensile strain along the [100] and [$01\bar{1}$] directions respectively, providing biaxial strain.[27] Experiments have shown that piezoelectric biaxial strain ε_{xx}-ε_{yy} of up to 4000ppm in magnitude can be generated using a PMN-PT substrate with this composition and cut.[30]

Micromagnetics simulations were run to validate the EA and HA locations of the "peanut" shaped nanomagnet. This finite element based model uses the Landau-Lifshitz-Gilbert (LLG) equation with magnetoelastic coupling and shape demagnetization effects to simulate device behavior.[60] During the design of the "peanut" shape, five parameters were modified that to achieve the desired magnetic behavior: length of major axis L_{major}, length of minor axis L_{minor}, angle of major axis θ_{major}, angle of minor axis θ_{minor} and magnetic element thickness d. In the micromagnetics simulations presented, these parameters were set as L_{major} = 111nm, L_{minor} = 90nm, θ_{major} = 60°, θ_{minor} = 45°and d = 10nm. The energy profile of the "peanut" shape is shown in figure 4.3, with the EA along θ_{ea} = 82.6° and HA along θ_{ha} = 5.1°. The EA and HA have been rotated CW and CCW respectively, compared to the energy profile of a standard ellipse shown in figure 4.4 with θ_{ea} = 90° and θ_{ha} = 0°. We note that for the "peanut" shape θ_{ea} and θ_{ha} do not exactly align with θ_{major} and θ_{minor}. This can be better understood in terms of the energy profile of the device structure. The EA and HA of a system correspond to the magnetic energy minimum and maximum respectively. Further, the EA and HA are determined by the direction of the net magnetic moment and the energy associated with a magnetic structure that has a net magnetization slightly off the EA or HA will still have an energy close to that of the extremum. So in reality the energy of a magnetic structure varies continuously and relatively smoothly as a "function" of the angle of magnetization. In the energy profile, valley floors and hill tops

represent the EA and HA respectively. For this example the major axis and minor axis are 15 degrees apart. This places a local minimum very close to a local maximum with the effect being that these two features distort each other, the net result being that the EA and HA determined by micromagnetics simulations are further apart than predicted from the geometry alone, i.e. at 82.6° and 5.1° respectively. The energy barrier between two stable magnetization states along EA is $263k_bT$, satisfying the suggested thermal stability requirement of non-volatile magnetic memory bit design ($>40k_bT$)[89].

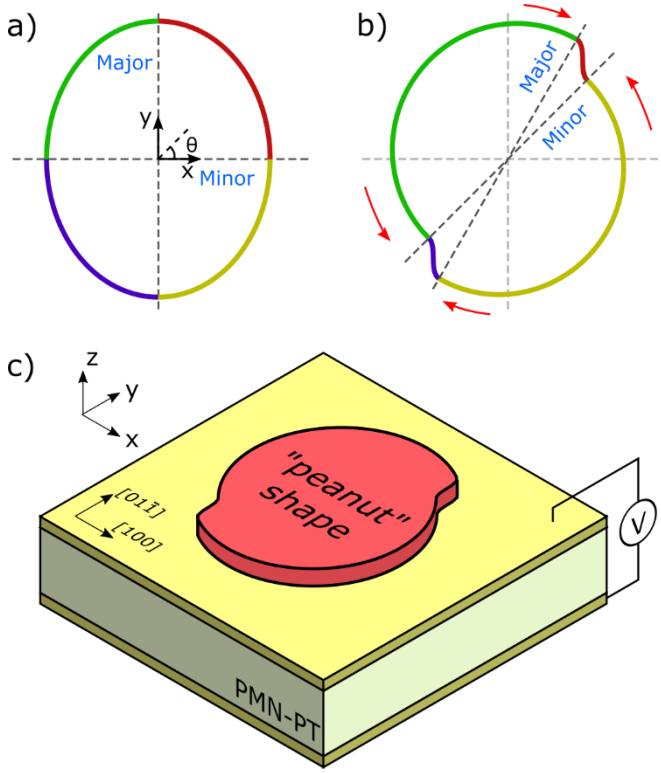

Figure 4.2. The design process of a "peanut" shaped nanomagnet. (a) The shape of a standard ellipse, with EA and HA coincident with major axis along y-axis and minor axis along x-axis, respectively. (b) Moving the location of geometric major axis CW and minor axis CCW, aiming to rotate magnetic EA and HA accordingly and to produce non-perpendicular EA and HA. The shape in (b) is named "peanut" shape due to geometric similarity. The four parts of the "peanut" shape in (b) labeled in different color, are corresponding to the parts with same color in four quadrants in the ellipse in (a). (e) The isometric view of the strain-mediated ME device with the "peanut" shaped nanomagnet and a PMN-PT substrate.

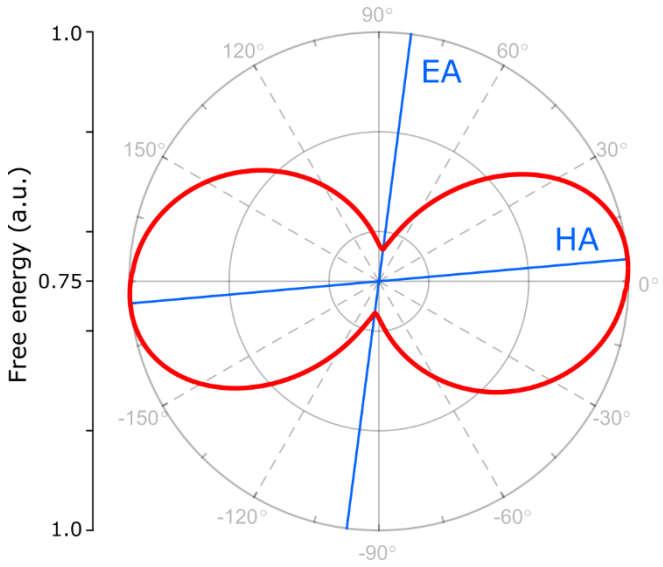

Figure 4.3. Energy profile for a "peanut" shaped nanomagnet with parameters L_{major} = 111nm, L_{minor} = 90nm, θ_{major} = 60°, θ_{minor} = 45°and d = 10nm. Free energy includes the demagnetization energy E_{demag} and the exchange energy E_{ex}. The easy axis (lowest free energy) is along θ_{ea} = 82.6° and the hard axis (highest free energy) is along θ_{ha} = 5.1°.

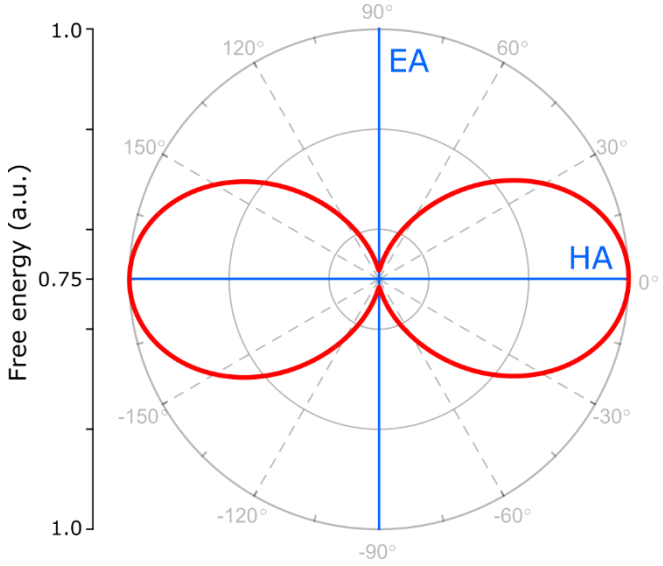

Figure 4.4. Energy profile for a standard elliptical shaped nanomagnet with length of major axis = 111nm, minor axis 90nm and thickness 10nm, oriented with minor axis along horizontal direction and major axis along vertical direction. Free energy includes the demagnetization energy E_{demag} and the exchange energy E_{ex}. The easy axis (lowest free energy) is along θ_{ea} = 90° and the hard axis (highest free energy) is along θ_{ha} = 0°.

Figure 4.5(a) shows micromagnetics simulation results of the "peanut" nanomagnet in response to the electric-field-induced strain on the piezoelectric substrate. The red arrows indicate the local in-plane magnetization direction. Background rainbow colors indicate the magnitude of out-of-plane magnetization. The magnetization of the "peanut" nanomagnet was initialized along the θ_{major} direction at time t=0. State I shows the magnetization distribution at time t=1ns when the magnetization stabilized and formed a single domain state aligned with the EA at $\theta_{ea} = 82.6°$. Piezoelectric biaxial strain of ε_{xx}-ε_{yy}=-4000ppm was applied right after 1ns at 1ns<t≤3.5ns. State II shows the magnetization at t = 3.5ns before piezostrain was released. The magnetization of the "peanut" shape rotated CW towards the compressive strain direction (green arrows) and stabilized on average along θ=-1.9°. The piezoelectric strain field was then released at 3.5ns<t≤6ns. State III shows the magnetization at t=6ns. Relative to the state II with applied piezostrain, the magnetization rotated CW and stabilized on average in the direction of θ=-97.4° aligning with the EA. From state I to state III, the magnetization rotated CW 180° in total by applying and then releasing -4000ppm piezoelectric biaxial strain. Similarly, the same strain field was again applied at 6ns<t≤8.5ns and was released at 8.5ns<t≤11ns. State IV demonstrated the magnetization distribution at t = 8.5ns. At t=11ns the magnetization distribution was the identical as the one in state I. This shows that the magnetization rotated back to the original state. The whole process of magnetization components m_1, m_2 and m_3 changing relative to time is illustrated in figure 4.5(b). During the 11ns of the simulation, a 360° deterministic CW magnetization rotation (two sequential 180° rotations) was achieved by applying the same piezoelectric biaxial strain field twice. The micromagnetics simulations demonstrate the function of the ME device with the engineered "peanut" nanomagnet.

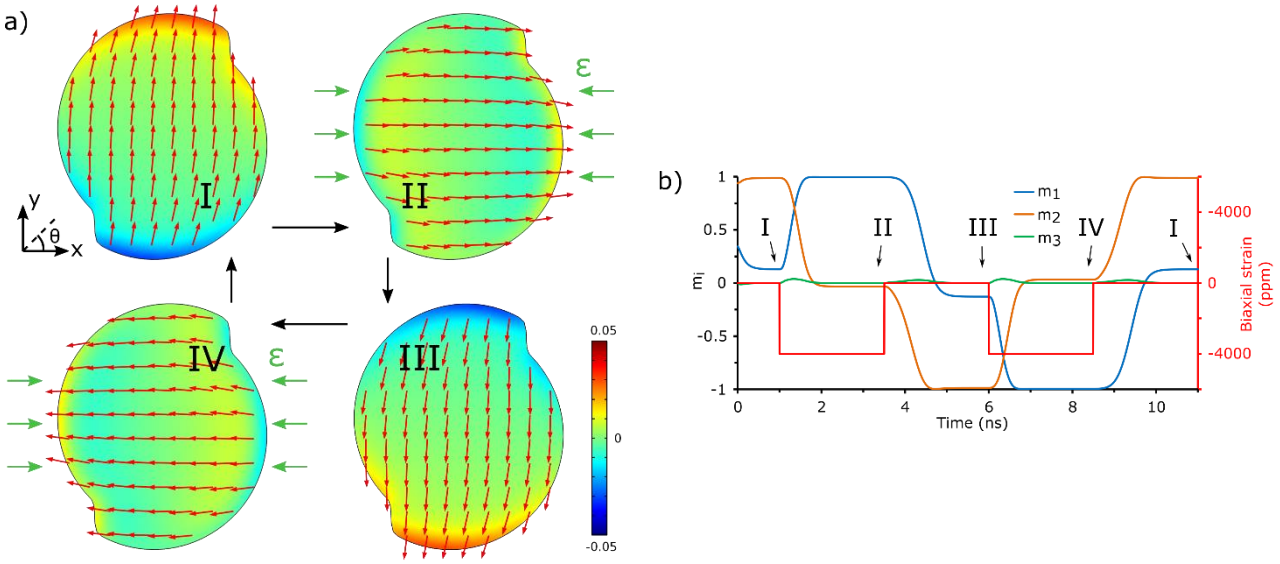

Figure 4.5. The micromagnetic simulation results of a "peanut" shaped nanomagnet controlled by the electric-field-induced strain on the PMN-PT substrate. (a) Magnetization distribution in four states, I (before piezostrain was applied at t= 1ns, and after piezostrain was applied twice at t=11ns), II (after piezostrain was applied at t=3.5ns), III (after piezostrain was released at t=6ns) and IV (after piezostrain was applied again at t=6ns). The red arrows represent the local in-plane magnetization direction. The rainbow background color indicates the out-of-plane component of local magnetization. Green arrows indicate the compressive strain direction of applied piezoelectric biaxial strain. (b) The magnetization components change in response to the applied piezoelectric biaxial strain. m_1, m_2 and m_3 denote the averaged magnetization component along x, y and z axis, respectively. The solid red line indicates the applied biaxial strain loading as a function of time.

A parametric study of the "peanut" shape magnetic element was performed. Several design parameters were manipulated in the design process for the "peanut" shaped nanomagnets. There are five parameters related to the shape that affect its magnetic behavior: length of major axis L_{major}, length of minor axis L_{minor}, angle of major axis θ_{major}, angle of minor axis θ_{minor} and magnetic element thickness d. A parametric study of these parameters was performed to obtain a relation between geometric shape and magnetic behavior and to improve device functionality.

For the "peanut" shaped nanomagnets, several cases with the same L_{major}, L_{minor} and d but different θ_{major} and θ_{minor} were studied. As seen in figure 4.6, changing the geometric shape

parameters θ_{major} and θ_{minor}, can change the angles of magnetic easy axis (EA) θ_{ea} and hard axis (HA) θ_{ha}. Comparing case 1 with case 2, rotating geometric minor axis CCW (increasing θ_{minor}) correspondingly rotated CCW the magnetic HA, since according to the concept of a ellipse the HA aligns with the minor axis. However, the EA also rotated CCW, even though the angle of major axis θ_{major} stayed unchanged. The EA/HA are the directions of net magnetization along which the free energy profile is at its minimum/maximum. Manipulating one shape design parameter, like θ_{minor}, can change the whole free energy profile and hence change both the directions of EA and HA. Hence rotating the minor axis CCW can "push" CCW both EA and HA. Similarly, rotating the major axis CW can also "push" both EA and HA CW. Comparing case 2 with case 3, when rotating the major axis CW and minor axis CCW at the same time, the resultant is that the EA rotated CW and the HA also rotated CW. Even though the minor axis rotating CCW can possibly rotate the EA and HA CCW, this effect cannot compete with the major axis rotating CW that can rotate the EA and HA CW. Comparing case 3 with case 4 can give similar solution. These cases show the possibility of manipulating the direction of magnetic EA and HA by changing the direction of geometric major and minor axes.

A certain amount of piezostrain is needed for the "peanut" shaped nanomagnet to trigger the 180° magnetization rotation. Figure 4.7(a) shows the magnetic behavior of a "peanut" shape with L_{major} = 100nm, L_{minor} = 85nm, θ_{major} = 75°, θ_{minor} = 15° and d = 15nm in response to piezoelectric biaxial strain in various magnitude. As seen in this figure, the magnetization can rotate 180° with application of -4000ppm biaxial strain, which is not achievable by a strain with magnitude -1500, -2000 or -3000ppm. This is to say, for a "peanut" shape design with specific design parameters, there is an energy barrier between EA and HA that requires a sufficient amount of piezostrain to overcome to complete the 180° magnetization rotation. The minimum

required amount of piezostrain can be tuned by adjusting L_{major}, L_{minor} and d, as shown in Figure 4.7(b). The figure shows a parametric study for a "peanut" shape with same $\theta_{major} = 75°$, $\theta_{minor} = 15°$ but different L_{major}, L_{minor} and d. Comparing with the case with L_{major}=100nm, L_{minor}=85nm and d=15nm (red line) and the case with L_{major}=100nm, L_{minor}=85nm and d=10nm (grey line), decreasing the thickness from 15nm to 10nm reduces the required magnitude of piezostrain from 4000ppm to 2000ppm. Comparing with the case with L_{major}=100nm, L_{minor}=85nm and d=10nm (grey line) and the case with L_{major}=100nm, L_{minor}=90nm and d=10nm (purple line), increasing the aspect ratio L_{minor}/L_{major} from 0.85 to 0.9 reduces the magnitude of required piezostrain from 2000 ppm to 1500ppm. This indicates that the amount of piezostrain needed to achieve 180° magnetization reorientation can be effectively lowered by adjusting the shape parameters. Manipulating the five design parameters can effectively tune the magnetic behavior of the "peanut" shaped nanomagnets. The parameters can be further tuned to optimize the functionality of the device tailoring it to a particular application.

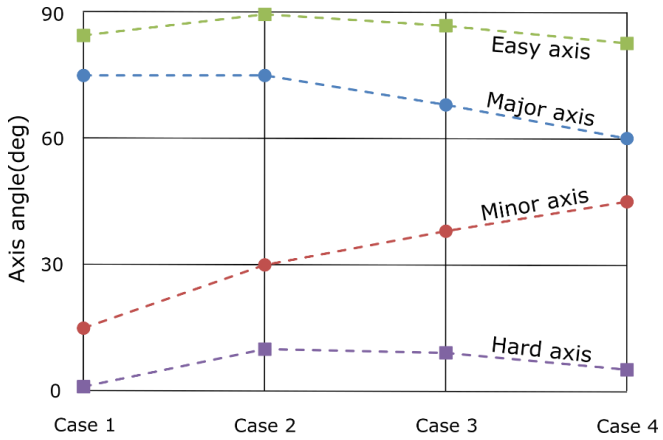

Figure 4.6. A parametric study of θ_{major} and θ_{minor} for the "peanut" shaped nanomagnets with L_{major} = 111nm, L_{minor} = 90nm and d = 10nm. Case 1, $\theta_{major} = 75°$ and $\theta_{minor} = 15°$; case 2, $\theta_{major} = 75°$ and $\theta_{minor} = 30°$; case 3, $\theta_{major} = 68°$ and $\theta_{minor} = 38°$; case 4, $\theta_{major} = 60°$ and $\theta_{minor} = 45°$. For each case, the directions of geometric major axis, minor axis, magnetic easy axis and hard axis are plotted, respectively.

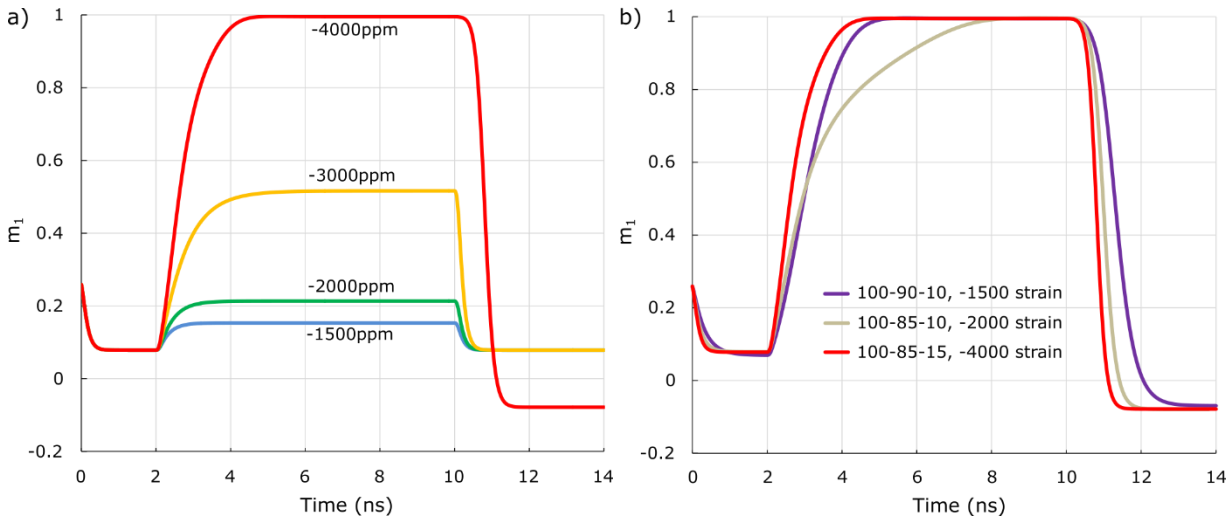

Figure 4.7. (a) Magnetization change of a "peanut" shaped nanomagnet with L_{major} = 100nm, L_{minor} = 85nm, θ_{major} = 75°, θ_{minor} = 15° and d = 15nm in response to piezoelectric biaxial strain in various magnitude. m_1 is the averaged magnetization along x axis. The piezostrain field was applied at 2ns<t≤10ns. Only for the case with -4000ppm piezostrain, this "peanut" shape managed to achieve 180° degree magnetization rotation. (b) Magnetization change of "peanut" shaped nanomagnets with θ_{major} = 75°, θ_{minor} = 15°and various L_{major}, L_{minor} and d. For the case with L_{major}=100nm, L_{minor}=85nm and d=15nm (red line), -4000ppm piezostrain is needed for a complete 180° magnetization rotation; for the case with L_{major}=100nm, L_{minor}=85nm and d=10nm (grey line), -2000ppm is needed; for the case with L_{major}=100nm, L_{minor}=90nm and d=10nm (purple line), -1500ppm is needed.

4.3. "Cat-eye" shaped nanomagnets

The "cat-eye" shaped nanomagnet was developed as an annular structure that can achieve deterministic strain-mediated electrically driven 180° magnetization reorientation on a piezoelectric substrate. For a typical symmetric ring nanomagnet, strain-mediated magnetization control is not deterministic and limited by 90° rotation. A narrow thin-film magnetic ring structure can form into an "onion" domain state with two head-to-head domain walls.[30], [61] Due to its geometric center-symmetry composed of two concentric circles, a ring nanomagnet in the "onion" state has no in-plane EA or HA, i.e., no preferred magnetization direction. Previous

research has demonstrated that the magnetization of a ring structure can be rotated by 90° by electric-field-induced strain on a PMN-PT substrate, however the rotational direction is not deterministic.[29] Once applying the piezoelectric biaxial strain field to a ring nanomagnet with compressive strain direction orthogonal to the original magnetization direction, the magnetization has equal probability of rotating CW and CCW by 90°. When the piezostrain is released, the magnetization stays in this new orientation. A method for deterministic magnetization control in ring structures is required for device applications.

We start with introducing EA and HA into ring structures. A recent study by Richter *et al* experimentally demonstrated shape driven domain wall motion in an asymmetric Permalloy ring structure (composed by two off-centered circles) from the geometric widest part to the narrowest part.[90] As a first step in taking advantage of this phenomenon, we performed micromagnetics simulations on a ring structure with the circular outer shape and elliptical inner shape shown in figure 4.8(a-b). Note that in this geometry, there are two widest parts along the x-axis and two narrowest parts along the y-axis. Once the magnetization was initialized along the x-axis, the magnetization formed into the "onion" state (see figure 4.8(a)) and automatically rotated to the two narrowest parts along the y-axis as shown in figure 4.8(b). The energy plot of this process (see Figure 4.9) indicates that this results in minimization of the combined demagnetization energy and exchange energy. Since the magnetization direction tends towards the geometric narrowest parts (y-axis) and away from the widest parts (x-axis), the x-axis can be considered a magnetic HA and the y-axis an EA for this outer-circular and inner-elliptical ring structure. Comparing with the symmetric ring structure composed of two concentric circles, we induced an EA and HA into the ring structure by modifying the inner shape from a circle to an ellipse. Note for this shape the EA and HA are perpendicular to each other.

We further modified the inner shape of the ring structure to achieve magnetic anisotropy with EA and HA non-perpendicular to each other (used also in “peanut” shape design) to achieve the function of deterministic 180° magnetization rotation with a single piezostrain actuation. The mechanism bridging geometric shape and magnetic behavior is the shape driven domain wall motion away from geometric widest part (magnetic HA) and towards narrowest part (EA). Starting from the shape shown in figure 4.8(c), we moved the location of geometric widest parts CCW and narrowest parts CW, aiming to rotate the magnetic EA and HA. This produced a new shape as shown in figure 4.8(d). The four quadrants of the original inner elliptical shape correspond to the four parts with same color of the modified shape. This new shape is referred to as “cat-eye” due to geometric similarity. Figure 4.8(e) shows the resultant design of the strain-mediated ME device on PMN-PT substrate. The PMN-PT substrate provides the required biaxial strain along its crystalline directions (compressive strain along [100] and tensile strain along $[01\bar{1}]$).

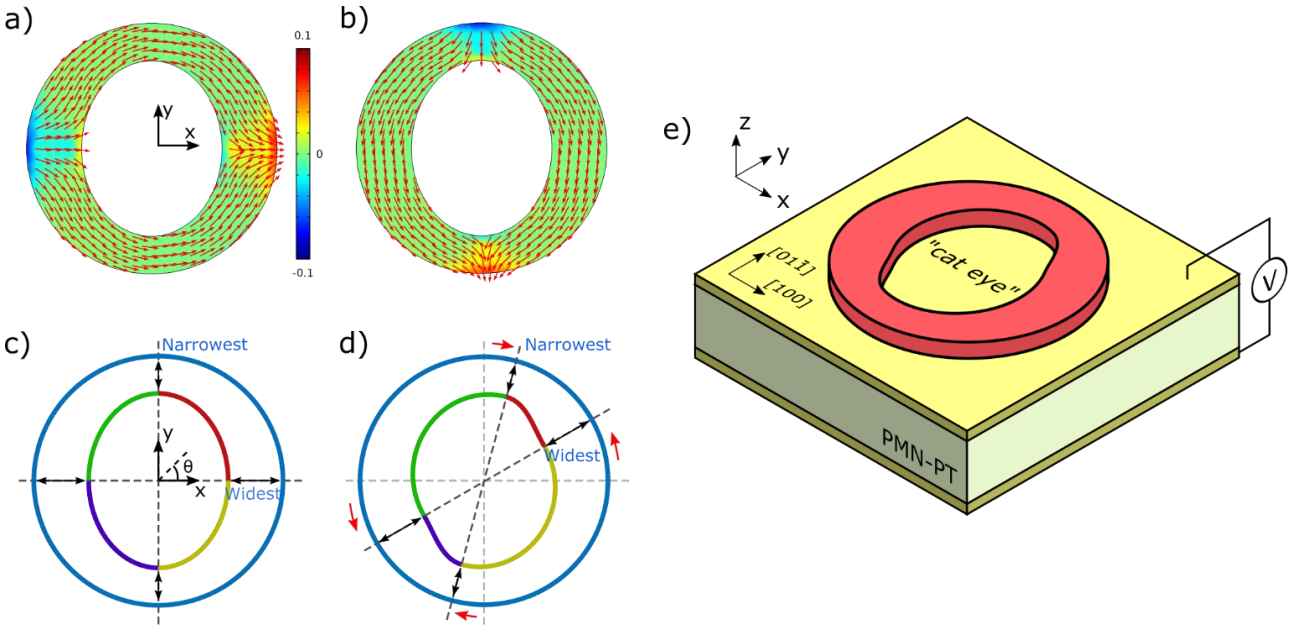

Figure 4.8. The design process of a "cat-eye" shape magnetic element. (a) Micromagnetics simulation result of an asymmetric ring with circular outer shape (500nm diameter) and elliptical inner shape (major axis 350nm, minor axis 280nm), initialized along x direction and formed "onion" state. The red arrows represent local in-plane magnetization direction. The rainbow background color indicates the out-of-plane component of local magnetization. (b) Micromagnetics simulation result when magnetization fully relaxed and moved to lowest energy state. (c) The shape of an asymmetric ring with circular outer shape and elliptical inner shape. (d) Moving the location of two narrowest parts CW and two widest parts CCW in a ring structure, aiming to rotate magnetic EA and HA to produce non-perpendicular EA and HA. The four parts of the inner shape labeled in different color, are corresponding to the parts with same color in four quadrants in the inner ellipse in (c). (e) The isometric view of the strain-mediated ME device with the "cat-eye" shaped nanomagnet on a PMN-PT substrate.

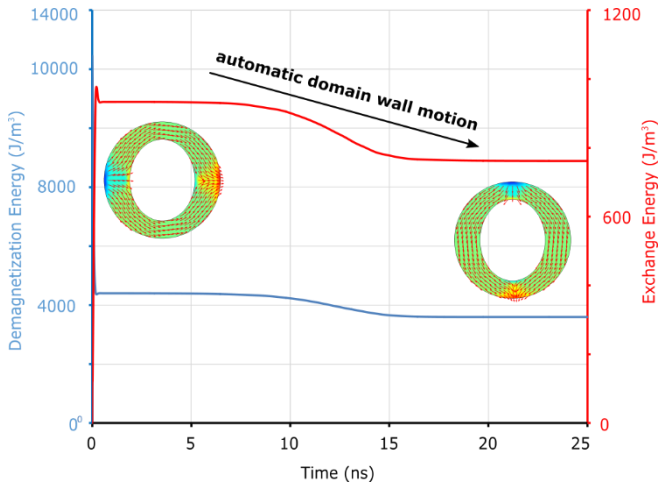

Figure 4.9. The energy plot of an asymmetric ring shaped nanomagnet with circular outer shape (500nm diameter) and elliptical inner shape (length of major axis 350nm, length of minor axis 280nm), with magnetization initialized along the horizontal direction at t=0s. The magnetization rotated to the vertical direction with two domain walls sitting at the narrowest part of the asymmetric ring at t =25ns. It is shown that this automatic domain wall movement is an energy minimization process of the demagnetization energy E_{demag} and the exchange energy E_{ex}.

Micromagnetics simulations were performed to validate the "cat-eye" shape design in response to the electric-field-induced strain on the PMN-PT substrate, shown in figure 4.10. There are six parameters that define the shape and affect the magnetic behavior of the "cat-eye" shape element: length of outer shape diameter L_{outer}, width of the narrowest part of the ring $L_{narrowest}$, width of the widest part of the ring L_{widest}, angle of the narrowest part $\theta_{narrowest}$, angle of widest part θ_{widest} and magnetic structure thickness d. In this simulation, L_{outer}=500nm, $L_{narrowest}$=75nm, L_{widest}=120nm, $\theta_{narrowest}$=75°, θ_{widest}=30° and d = 15nm. After magnetization is initialized along the $\theta_{narrowest}$ direction at t=0ns, the magnetization formed into "onion" state and stabilized at t=0.5ns. Two head-to-head domain walls formed at θ=75° and -105° position respectively, see state I in figure 4.10(a). A piezoelectric biaxial strain of ε_{xx}-ε_{yy}=-4000ppm was applied at 0.5ns<t≤23ns. State II shows the magnetization distribution at t=23ns. After application of piezostrain, it can be seen that the domain walls align with the compressive strain

(green arrows) direction at θ=0°. From 23ns<t≤50ns, the piezostrain was released and state III shows the resultant magnetization distribution at t=50ns. It is shown that the magnetization continued to rotate CW until stopping at the position 180° from the initial condition in state I. This is due to an energy minimization process involving demagnetization energy and exchange energy. An energy plot for this process is shown in figure 4.11. From time t=0 to t=50ns, the magnetization of the "cat-eye" shape rotated CW by 180° with a single application of piezostrain. The same biaxial strain was applied at 50ns<t≤73ns and released at 73ns<t≤100ns. State IV shows the magnetization distribution at t=73ns. At t=100ns the magnetization went back to its original state I before any strain was applied. This confirms that the second application of piezostrain deterministically drove the magnetization through a second 180° CW rotation. Overall, a 360° magnetization rotation was achieved from t=0ns to 100ns during which the piezostrain was applied twice. The magnetization components m_1, m_2 and m_3 in response to piezoelectric biaxial strain are plotted in figure 4.10(b). During the 100ns of simulation, a 360° deterministic CW magnetization rotation was achieved from two subsequent 180° rotations, each induced by application of the same piezoelectric strain field. The micromagnetics simulations demonstrate the function of the ME device with the engineered "cat-eye" nanomagnet.

The design parameters L_{outer}, $L_{narrowest}$, L_{widest}, $\theta_{narrowest}$, θ_{widest} and d can be changed and optimized according to target device function. The "cat-eye" shape has a wide range of scalability, since the "onion" state exists among magnetic rings with outer diameter from a few hundred nanometers up to a few microns. By changing the strain rate of the applied load, the speed of domain wall motion can be controlled. The relative positions of the two widest/narrowest ring sections do not have to be center-symmetric for a functioning device. The

wide availability of the design parameters increases the applicability of the “cat-eye” shape nanomagnets for various spintronic devices.

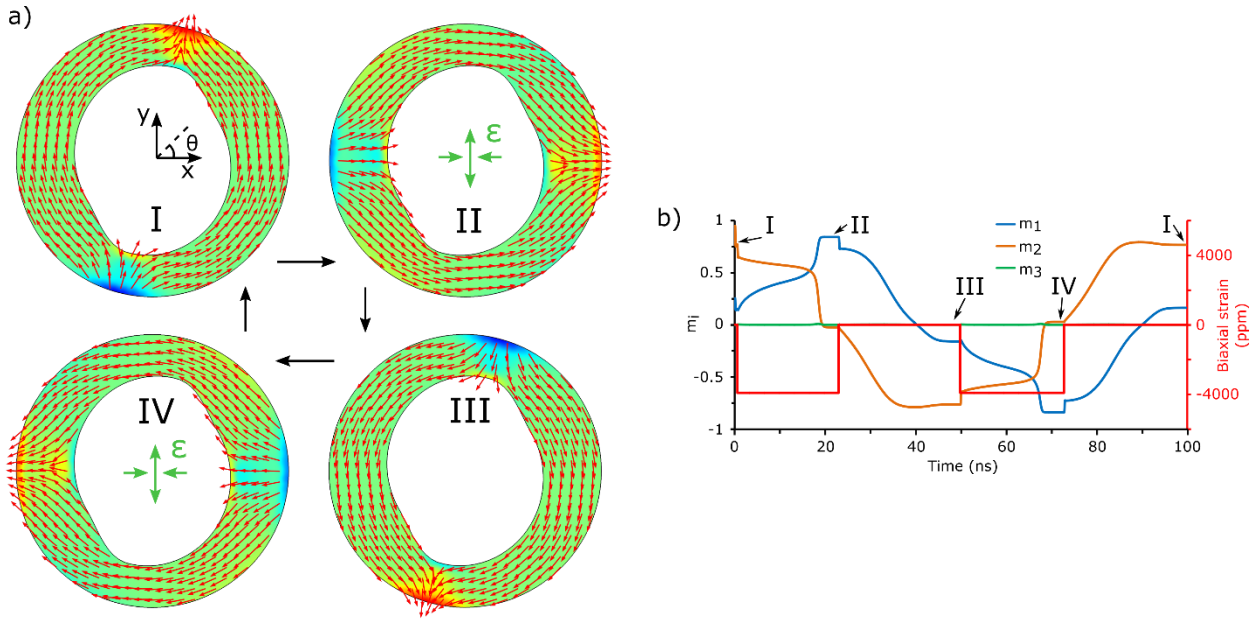

Figure 4.10. The micromagnetics simulation results of the “cat-eye” shaped nanomagnet controlled by electric-field-induced strain on the PMN-PT substrate. (a) Magnetization distribution in four states, I (before piezostrain was applied at t=0.5ns, and after piezostrain was applied twice at t=100ns), II (after piezostrain was applied at t=23ns), III (after piezostrain was released at t=50ns) and IV (after piezostrain was applied again at t=73ns). The red arrows represent the local in-plane magnetization direction. The rainbow background color indicates the out-of-plane component of local magnetization. Green arrows indicate the applied piezoelectric biaxial strain. (e) The magnetization components change in response to the applied piezoelectric biaxial strain. m_1, m_2 and m_3 denote the averaged magnetization component along x, y and z-axis, respectively. The solid red line indicates the applied biaxial strain loading as a function of time.

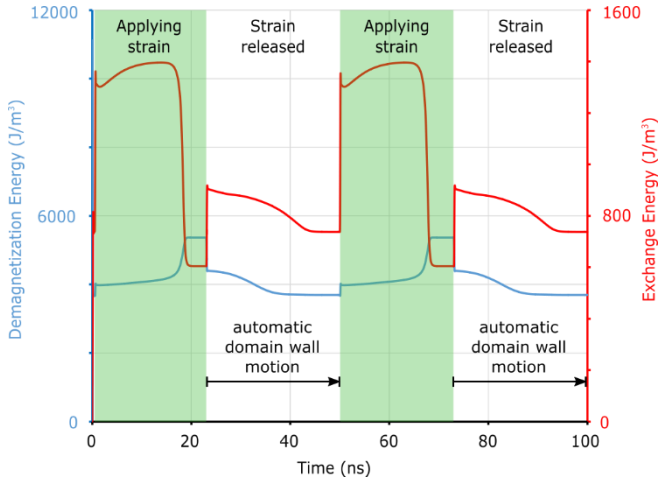

Figure 4.11. The energy plot of a "cat-eye" shaped nanomagnet with L_{outer}=500nm, $L_{narrowest}$ = 75nm, L_{widest}=120nm, $\theta_{narrowest}$ = 75°, θ_{widest}=30° and d = 15nm, with magnetization initialized along $\theta_{narrowest}$ direction at t=0s. When applying, the sum of demagnetization energy and exchange energy $E_{demag}+E_{ex}$ increased, with magnetization rotating clockwise toward the compressive strain direction; when piezostrain was released, during the automatic domain wall motion process, E_{demag} and E_{ex} minimized.

4.4. Discussion

The engineering principles we followed in designing the "peanut" and "cat-eye" shapes are summarized. The conventional approach for nanomagnetic device research is: (1) bring up a nanomagnet in a certain shape; (2) investigate its magnetic anisotropy; and (3) design a device with this nanomagnet for a certain function. We adopted a reversed approach: (1) design a nanomagnetic device with a certain function (180° magnetization switching in response to a single piezostrain pulse); (2) determine the desired magnetic anisotropy (EA and HA not perpendicular to each other) that leads to this type of functionality; and (3) architect the shape of the nanomagnet to obtain this magnetic anisotropy (through the mechanism bridging geometric shape and magnetic behavior). Since the new approach provides a guideline for engineering novel shapes for a targeted device function, only a few micromagnetics simulations are needed to fine tune the design and produce a shape with the desired functionality.

This idea of engineering nanomagnets in novel shapes could be implemented with computer-assisted topological optimization techniques. The “peanut” shape parametric study has demonstrated that varying the geometric shape parameters (L_{major}, L_{minor}, θ_{major}, θ_{minor} and d) can affect the function of the device. These shape parameters can be optimized. The optimization rules can be set as tailored magnetic anisotropy, thermal stability requirement (>40k_bT), certain amount of applied magnetic field/piezostrain/spin-polarized current and magnetization switching time, etc. After the topological optimization process, engineers can find improved nanomagnet designs with optimized device performance.

4.5. Conclusion

In this chapter, we architected the shape of nanomagnets with tailored magnetization behavior. We presented novel “peanut” and “cat-eye” shaped nanomagnets, both demonstrating the ability to accomplish strain-mediated CW 180° magnetization rotation like magnetic ratchets. Magnetic anisotropy with non-perpendicular EA and HA can achieve deterministic 180° magnetization switching in response to piezoelectric biaxial strain. In order to incorporate this type of magnetic anisotropy in nanomagnets, we modified the geometric shape based on the mechanism bridging geometry and magnetic behavior. The “peanut” and “cat-eye” shapes were then produced. A strain-mediated ME device was designed with the “peanut” and “cat-eye” shaped nanomagnets and a PMN-PT piezoelectric substrate. Micromagnetics simulations were employed and the results demonstrated the performance of the device, achieving deterministic CW 180° magnetization rotation upon a single piezostrain pulse, and a total of 360° magnetization rotation by applying the same strain field twice. The “peanut” and “cat-eye” shaped nanomagnets provide a simple and effective design for developing future spintronic

devices, e.g. non-volatile memory bits. The engineering principle implemented in this work starts from a target device function down to nanomagnets in novel shapes. This method may be coupled with topology optimization techniques to achieve optimized nanomagnet shapes. This approach opens a broad design space for next generation spintronic devices with nanomagnets in novel shapes taking advantage of magnetic shape anisotropy.

Chapter 5. Summary and Conclusions

This dissertation has described novel approaches for deterministic control of individual nanomagnets in strain-mediated multiferroic heterostructures. Controlling magnetism by piezoelectric strain in strain-mediated multiferroic heterostructures is considered the most energy efficient approach for non-volatile memory devices. Though providing evidence for strain manipulation of magnetization, prior work has offered no ability for individual element control of arrays of nanomagnets on a substrate nor has it offered a method for deterministic control of magnetization in nanomagnets. A literature review that identified these issues for strain-mediated multiferroic heterostructures was provided in chapter 1.

In the present work, electrode patterns were designed on a piezoelectric to produce localized strain, offering the ability to control individual nanomagnet elements in arrays of strain-mediated multiferroic heterostructures. Finite element simulations were performed for optimizing the electrode pattern. A proof-of-concept experiment was conducted on a Ni thin film/bulk PZT multiferroic heterostructure. MOKE magnetometry characterization validated the concept. Further experiments were conducted to demonstrate that this approach was also valid for heterostructures consisting of a micron-sized Ni ring structure surrounded by electrode patterns fabricated on top of a micron scale thin film PZT on a Si substrate. By selectively applying voltage on different electrode pairs, various localized strain configurations were generated. MFM characterization showed that deterministic magnetization reorientation was possible for individual Ni ring structures in response to the electric field induced strain. The work on electrode pattern design on Ni thin film/bulk PZT and nanoscale Ni ring/thin film PZT heterostructures was presented in chapters 2 and 3, respectively.

Architecting the geometric shape of nanomagnets can be used to tailor the magnetic anisotropy for deterministic strain-mediated magnetization control. This concept is to tune the magnetic shape anisotropy, which relates the geometric shape of the nanomagnets to their magnetic behavior. Strain is a uniaxial effect and, unlike directional magnetic field, cannot induce a full 180° reorientation of the magnetization vector when acting alone. Novel “peanut” and “cat-eye” shaped nanomagnets were engineered demonstrating 180° clockwise magnetization reorientation in response to a single piezoelectric strain trigger. The results were validated using micromagnetics simulations. The work on the shape engineering of nanomagnets was presented in chapter 4.

The novel concepts presented enable deterministic control of individual nanomagnets in strain-mediated multiferroic heterostructures. This is a critical step toward the implementation of next generation magnetoelectric non-volatile memory applications. The present work contributes to future spintronic devices featuring ultra-low power consumption.

List of references

[1] S. S. P. Parkin, M. Hayashi, and L. Thomas, "Magnetic Domain-Wall Racetrack Memory," *Science*, vol. 320, pp. 190–194, 2008.

[2] R. Ramesh and N. A. Spaldin, "Multiferroics : progress and prospects in thin fi lms," *Nat. Mater.*, vol. 3, pp. 21–29, 2007.

[3] C. W. Nan, M. I. Bichurin, S. Dong, D. Viehland, and G. Srinivasan, "Multiferroic magnetoelectric composites: Historical perspective, status, and future directions," *J. Appl. Phys.*, vol. 103, no. 2008, p. 031101, 2008.

[4] J.-M. Hu, Z. Li, L.-Q. Chen, and C.-W. Nan, "High-density magnetoresistive random access memory operating at ultralow voltage at room temperature," *Nat. Commun.*, vol. 2, p. 553, 2011.

[5] M. Buzzi, R. V. Chopdekar, J. L. Hockel, A. Bur, T. Wu, N. Pilet, P. Warnicke, G. P. Carman, L. J. Heyderman, and F. Nolting, "Single Domain Spin Manipulation by Electric Fields in Strain Coupled Artificial Multiferroic Nanostructures," *Phys. Rev. Lett.*, vol. 111, no. 2, p. 027204, 2013.

[6] J. M. Hu and C. W. Nan, "Electric-field-induced magnetic easy-axis reorientation in ferromagnetic/ferroelectric layered heterostructures," *Phys. Rev. B - Condens. Matter Mater. Phys.*, vol. 80, no. 22, p. 224416, 2009.

[7] J. J. Wang, J. M. Hu, J. Ma, J. X. Zhang, L. Q. Chen, and C. W. Nan, "Full 180° Magnetization Reversal with Electric Fields," *Sci. Rep.*, vol. 4, p. 7507, 2014.

[8] N. A. Spaldin and M. Fiebig, "The Renaissance of Magnetoelectric Multiferroics," *Science*, vol. 309, no. 5733, pp. 391–392, 2005.

[9] P. Curie, "Sur la symmetric dans phenomenes physiques," *J. Phys.*, vol. 3, p. 393, 1894.

[10] L. D. Landau and E. M. Lifshitz, *Electrodynamics of Continuous Media*. Pergamon Press, 1960.

[11] I. E. Dzyaloshinskii, "On The Magneto-Electrical Effect In Antiferromagnetics," *Sov. Phys. Jetp-Ussr*, vol. 10, pp. 628–629, 1960.

[12] D. N. Astrov, "The Magnetoelectric Effect In Antiferromagnetics," *Sov. Phys. Jetp-Ussr*, vol. 11, pp. 708–709, 1960.

[13] N. A. Hill, "Why Are There so Few Magnetic Ferroelectrics ?," *J. Phys. Chem. B*, vol. 104, no. 29, pp. 6694–6709, 2000.

[14] T. Kimura, T. Goto, H. Shintani, K. Ishizaka, T. Arima, and Y. Tokura, "Magnetic control of ferroelectric polarization," *Nature*, vol. 426, pp. 55–58, 2003.

[15] J. Wang, J. B. Neaton, H. Zheng, V. Nagarajan, S. B. Ogale, B. Liu, D. Viehland, V. Vaithyanathan, D. G. Schlom, U. V Waghmare, N. A. Spaldin, K. M. Rabe, M. Wuttig, and R. Ramesh, "Epitaxial BiFeO3 Multiferroic Thin Film Heterostructures," *Science*, vol. 299, no. 5613, pp. 1719–1722, 2003.

[16] T. Lottermoser, T. Lonkai, U. Amann, and M. Fiebig, "Magnetic phase control by an electric field," *Nature*, vol. 430, no. 6999, pp. 541–544, 2004.

[17] J. van Suchtelen, "PRODUCT PROPERTIES - NEW APPLICATION OF COMPOSITE-MATERIALS," *Philips Res. Reports*, vol. 27, no. 1, p. 28, 1972.

[18] A. M. J. G. Van Run, D. R. Terrell, and J. H. Scholing, "An in situ grown eutectic magnetoelectric composite material - Part 1 Composition and unidirectional solidification," *J. Mater. Sci.*, vol. 9, no. 10, pp. 1710–1714, 1974.

[19] J. Van Den Boomgaard, D. R. Terrell, R. A. J. Born, and H. F. J. I. Giller, “An in situ grown eutectic magnetoelectric composite material - Part 2 Physical properties,” *J. Mater. Sci.*, vol. 9, no. 10, pp. 1705–1709, 1974.
[20] J. Ryu, S. Priya, A. V. Carazo, K. Uchino, and H.-E. Kim, “Effect of the Magnetostrictive Layer on Magnetoelectric Properties in Lead Zirconate Titanate/Terfenol-D Laminate Composites,” *J. Am. Ceram. Soc.*, vol. 84, pp. 2905–2908, 2001.
[21] J. Ryu, A. Carazo, K. Uchino, and H. Kim, “Magnetoelectric Properties in Piezoelectric and Magnetostrictive Laminate Composites,” *Jpn. J. Appl. Phys.*, vol. 40, pp. 4948–4951, 2001.
[22] S. Dong, J. Li, and D. Viehland, “Ultrahigh magnetic field sensitivity in laminates of TERFENOL-D and Pb (Mg 1 / 3 Nb 2 / 3) O 3 – PbTiO 3 crystals Ultrahigh magnetic field sensitivity in laminates of TERFENOL-D,” *Appl. Phys. Lett.*, vol. 83, p. 2265, 2003.
[23] W. Eerenstein, M. Wiora, J. L. Prieto, J. F. Scott, and N. D. Mathur, “Giant sharp and persistent converse magnetoelectric effects in multiferroic epitaxial heterostructures,” *Nat. Mater.*, vol. 6, p. 348, 2007.
[24] M. Weiler, A. Brandlmaier, S. Geprägs, M. Althammer, M. Opel, C. Bihler, H. Huebl, M. S. Brandt, R. Gross, and S. T. B. Goennenwein, “Voltage controlled inversion of magnetic anisotropy in a ferromagnetic thin film at room temperature,” *New J. Phys.*, vol. 11, no. 1, p. 13021, 2009.
[25] J. J. Yang, Y. G. Zhao, H. F. Tian, L. B. Luo, H. Y. Zhang, Y. J. He, and H. S. Luo, “Electric field manipulation of magnetization at room temperature in multiferroic CoFe2O4/Pb(Mg1/3Nb2/3)0.7Ti0.3O3 heterostructures,” *Appl. Phys. Lett.*, vol. 94, no. 21, p. 212504, 2009.
[26] M. Liu, O. Obi, J. Lou, Y. Chen, Z. Cai, S. Stoute, M. Espanol, M. Lew, X. Situ, K. S. Ziemer, V. G. Harris, and N. X. Sun, “Giant electric field tuning of magnetic properties in multiferroic ferrite/ferroelectric heterostructures,” *Adv. Funct. Mater.*, vol. 19, no. 11, pp. 1826–1831, 2009.
[27] T. Wu, A. Bur, P. Zhao, K. P. Mohanchandra, K. Wong, K. L. Wang, C. S. Lynch, and G. P. Carman, “Giant electric-field-induced reversible and permanent magnetization reorientation on magnetoelectric Ni/(011) [Pb (Mg1/3 Nb 2/3) O3](1-x) - [PbTiO3] x heterostructure,” *Appl. Phys. Lett.*, vol. 98, no. 011, p. 012504, 2011.
[28] T. Wu, A. Bur, K. Wong, P. Zhao, C. S. Lynch, P. K. Amiri, K. L. Wang, and G. P. Carman, “Electrical control of reversible and permanent magnetization reorientation for magnetoelectric memory devices Electrical control of reversible and permanent magnetization reorientation for magnetoelectric memory devices,” *Appl. Phys. Lett.*, vol. 98, p. 262504, 2011.
[29] J. L. Hockel, A. Bur, T. Wu, K. P. Wetzlar, and G. P. Carman, “Electric field induced magnetization rotation in patterned Ni ring/Pb(Mg1/3Nb2/3)O3](1−0.32)-[PbTiO3]0.32 heterostructures,” *Appl. Phys. Lett.*, vol. 100, p. 022401, 2012.
[30] H. Sohn, M. E. Nowakowski, C. Liang, J. L. Hockel, K. Wetzlar, S. Keller, B. M. Mclellan, M. A. Marcus, A. Doran, A. Young, M. Kla, G. P. Carman, J. Bokor, and R. N. Candler, “Wall Rotation in Multiferroic Heterostructures to Manipulate Suspended On-Chip Magnetic Particles,” *ACS Nano*, vol. 9, no. 5, pp. 4814–4826, 2015.
[31] T.-K. Chung, G. P. Carman, and K. P. Mohanchandra, “Reversible magnetic domain-wall motion under an electric field in a magnetoelectric thin film,” *Appl. Phys. Lett.*, vol. 92, no. 11, p. 112509, 2008.

[32] T.-K. Chung, S. Keller, and G. P. Carman, “Electric-field-induced reversible magnetic single-domain evolution in a magnetoelectric thin film,” *Appl. Phys. Lett.*, vol. 94, no. 13, p. 132501, 2009.
[33] D. Damjanovic, “Ferroelectric, dielectric and piezoelectric properties of ferroelectric thin films and ceramics,” *Reports Prog. Phys.*, vol. 61, no. 9, p. 1267, 1998.
[34] Y. Bastani, T. Schmitz-Kempen, A. Roelofs, and N. Bassiri-Gharb, “Critical thickness for extrinsic contributions to the dielectric and piezoelectric response in lead zirconate titanate ultrathin films,” *J. Appl. Phys.*, vol. 109, no. 1, p. 014115, 2011.
[35] H. K. D. Kim, L. T. Schelhas, S. Keller, J. L. Hockel, S. H. Tolbert, and G. P. Carman, “Magnetoelectric control of superparamagnetism,” *Nano Lett.*, vol. 13, no. 3, pp. 884–888, 2013.
[36] R. P. Cowburn, “Property variation with shape in magnetic nanoelements,” *J. Phys. D. Appl. Phys.*, vol. 33, no. 1, pp. R1–R16, 1999.
[37] T. L. Gilbert, “A Phenomenological Theory of Damping in Ferromagnetic Materials,” *IEEE Trans. Magn.*, vol. 40, no. 6, pp. 3443–3449, 2004.
[38] R. C. O’handley, *Modern magnetic materials: principles and applications*. New York: Wiley, 2000.
[39] D. R. Fredkin and T. R. Koehler, “Hybrid method for computing demagnetizing fields,” *IEEE Trans. Magn.*, vol. 26, no. 2, pp. 415–417, 1990.
[40] Y. C. Shu, M. P. Lin, and K. C. Wu, “Micromagnetic modeling of magnetostrictive materials under intrinsic stress,” *Mech. Mater.*, vol. 36, no. 10, pp. 975–997, 2004.
[41] X. Zhu, P. Grütter, V. Metlushko, and B. Ilic, “Magnetic force microscopy study of electron-beam-patterned soft permalloy particles: Technique and magnetization behavior,” *Phys. Rev. B*, vol. 66, pp. 1–7, 2002.
[42] T. Liu and C. S. Lynch, “Ferroelectric properties of [110], [001] and [111] poled relaxor single crystals: Measurements and modeling,” *Acta Mater.*, vol. 51, no. 2, pp. 407–416, 2003.
[43] J. Wang, J. Ma, Z. Li, Y. Shen, Y. Lin, and C. W. Nan, “Switchable voltage control of the magnetic coercive field via magnetoelectric effect,” *J. Appl. Phys.*, vol. 110, no. 4, p. 043919, 2011.
[44] J. M. Hu, C. W. Nan, and L. Q. Chen, “Size-dependent electric voltage controlled magnetic anisotropy in multiferroic heterostructures: Interface-charge and strain comediated magnetoelectric coupling,” *Phys. Rev. B - Condens. Matter Mater. Phys.*, vol. 83, p. 134408, 2011.
[45] Z. Li, J. Hu, L. Shu, Y. Gao, Y. Shen, Y. Lin, and C. W. Nan, “Thickness-dependent converse magnetoelectric coupling in bi-layered Ni/PZT thin films,” *J. Appl. Phys.*, vol. 111, no. 3, p. 033918, 2012.
[46] L. Gan, R. D. Gomez, C. J. Powell, R. D. McMichael, P. J. Chen, and W. F. Egelhoff, “Thin Al, Au, Cu, Ni, Fe, and Ta films as oxidation barriers for Co in air,” *J. Appl. Phys.*, vol. 93, no. 10 3, pp. 8731–8733, 2003.
[47] S. A. Wolf, D. D. Awschalom, R. A. Buhrman, J. M. Daughton, S. von Molnár, M. L. Roukes, a Y. Chtchelkanova, and D. M. Treger, “Spintronics: a spin-based electronics vision for the future.,” *Science*, vol. 294, pp. 1488–1495, 2001.
[48] J.-E. Wegrowe, D. Kelly, P. Guittienne, and J.-P. Ansermet, “Magnetization reversal triggered by spin injection in magnetic nanowires,” *Europhys. Lett.*, vol. 56, p. 748, 2001.
[49] P. Borisov, A. Hochstrat, X. Chen, W. Kleemann, and C. Binek, “Magnetoelectric

switching of exchange bias," *Phys. Rev. Lett.*, vol. 94, p. 117203, 2005.
[50] Y.-H. Chu, L. W. Martin, M. B. Holcomb, M. Gajek, S.-J. Han, Q. He, N. Balke, C.-H. Yang, D. Lee, W. Hu, Q. Zhan, P.-L. Yang, A. Fraile-Rodríguez, A. Scholl, S. X. Wang, and R. Ramesh, "Electric-field control of local ferromagnetism using a magnetoelectric multiferroic.," *Nat. Mater.*, vol. 7, pp. 478–482, 2008.
[51] H. J. A. Molegraaf, J. Hoffman, C. A. F. Vaz, S. Gariglio, D. Van Der Morel, C. H. Ahn, and J. M. Triscone, "Magnetoelectric effects in complex oxides with competing ground states," *Adv. Mater.*, vol. 21, p. 3470, 2009.
[52] C. A. F. Vaz, J. Hoffman, Y. Segal, J. W. Reiner, R. D. Grober, Z. Zhang, C. H. Ahn, and F. J. Walker, "Origin of the magnetoelectric coupling effect in Pb(Zr0.2Ti0.8)O{3}/La{0.8}Sr{0.2}MnO{3} Multiferroic heterostructures.," *Phys. Rev. Lett.*, vol. 104, p. 127202, 2010.
[53] S. Finizio, M. Foerster, M. Buzzi, B. Krüger, M. Jourdan, C. A. F. Vaz, J. Hockel, T. Miyawaki, A. Tkach, S. Valencia, F. Kronast, G. P. Carman, F. Nolting, and M. Kläui, "Magnetic Anisotropy Engineering in Thin Film Ni Nanostructures by Magnetoelastic Coupling," *Phys. Rev. Appl.*, vol. 1, p. 021001, 2014.
[54] S. Trolier-McKinstry and P. Muralt, "Thin Film Piezoelectrics for MEMS," *J. Electroceramics*, vol. 12, no. 1–2, pp. 7–17, 2004.
[55] S. Tadigadapa and K. Mateti, "Piezoelectric MEMS sensors: state-of-the-art and perspectives," *Meas. Sci. Technol.*, vol. 20, no. 9, p. 092001, 2009.
[56] R. N. Torah, S. P. Beeby, and N. M. White, "Experimental investigation into the effect of substrate clamping on the piezoelectric behaviour of thick-film PZT elements," *J. Phys. D. Appl. Phys.*, vol. 37, pp. 1074–1078, 2004.
[57] V. Nagarajan, a Roytburd, a Stanishevsky, S. Prasertchoung, T. Zhao, L. Chen, J. Melngailis, O. Auciello, and R. Ramesh, "Dynamics of ferroelastic domains in ferroelectric thin films.," *Nat. Mater.*, vol. 2, no. 1, pp. 43–7, Jan. 2003.
[58] V. Nagarajan, "Scaling of the piezoelectric response in ferroelectric nanostructures: An effective clamping stress model," *Appl. Phys. Lett.*, vol. 87, p. 242905, 2005.
[59] J. Cui, J. L. Hockel, P. K. Nordeen, D. M. Pisani, C. Liang, G. P. Carman, and C. S. Lynch, "A method to control magnetism in individual strain-mediated magnetoelectric islands," *Appl. Phys. Lett.*, vol. 103, no. 23, p. 232905, 2013.
[60] C.-Y. Liang, S. M. Keller, A. E. Sepulveda, A. Bur, W.-Y. Sun, K. Wetzlar, and G. P. Carman, "Modeling of magnetoelastic nanostructures with a fully coupled mechanical-micromagnetic model," *Nanotechnology*, vol. 25, p. 435701, 2014.
[61] M. Kläui, C. A. F. Vaz, L. Lopez-Diaz, and J. A. C. Bland, "Vortex formation in narrow ferromagnetic rings," *J. Phys. Condens. Matter*, vol. 15, p. R985, 2003.
[62] C. T. Shelton, P. G. Kotula, G. L. Brennecka, P. G. Lam, K. E. Meyer, J.-P. Maria, B. J. Gibbons, and J. F. Ihlefeld, "Chemically Homogeneous Complex Oxide Thin Films Via Improved Substrate Metallization," *Adv. Funct. Mater.*, vol. 22, no. 11, pp. 2295–2302, Jun. 2012.
[63] R. Steinhausen, T. Hauke, W. Seifert, V. Mueller, H. Beige, S. Seifert, and P. Lobmann, "Clamping of piezoelectric thin films on metallic substrates: influence on the effective piezoelectric modulus d33," in *Proceedings of the 11th IEEE International Symposium on Applications of Ferroelectrics 98*, 1998, p. 93.
[64] X. Zhu, P. Grütter, V. Metlushko, and B. Ilic, "Systematic study of magnetic tip induced magnetization reversal of e-beam patterned permalloy particles," *J. Appl. Phys.*, vol. 91,

pp. 7340–7342, 2002.
[65] X. Zhu, P. Grütter, V. Metlushko, and B. Ilic, “Control of domain patterns in square shaped nickel rings,” *J. Appl. Phys.*, vol. 93, pp. 7059–7061, 2003.
[66] M. Kläui, “Head-to-head domain walls in magnetic nanostructures,” *J. Phys. Condens. Matter*, vol. 20, p. 313001, 2008.
[67] J. Atulasimha and S. Bandyopadhyay, “Introduction to Spintronic and Nanomagnetic Computing Devices,” in *Nanomagnetic and Spintronic Devices for Energy-Efficient Memory and Computing*, John Wiley & Sons, Ltd, 2016, pp. 1–8.
[68] M. Hehn, K. Ounadjela, J. Bucher, F. Rousseaux, D. Decanini, B. Bartenlian, and C. Chappert, “Nanoscale Magnetic Domains in Mesoscopic Magnets,” *Science (80-.).*, vol. 272, pp. 1782–5, 1996.
[69] J. Rothman, M. Kläui, L. Lopez-Diaz, C. A. F. Vaz, A. Bleloch, J. A. C. Bland, Z. Cui, and R. Speaks, “Observation of a Bi-domain state and nucleation free switching in mesoscopic ring magnets,” *Phys. Rev. Lett.*, vol. 86, no. 6, pp. 1098–1101, 2001.
[70] E. Muñoz-Sandoval, J. J. Torres-Heredia, and F. López-Urías, “Micromagnetic simulations of hysteresis loops in ferromagnetic Reuleaux’s triangles,” *J. Appl. Phys.*, vol. 97, no. 10, pp. 80–83, 2005.
[71] A. Imre, G. Csaba, L. Ji, A. Orlov, G. H. Bernstein, and W. Porod, “Majority Logic Gate for Magnetic Quantum-Dot Cellular Automata,” *Science (80-.).*, vol. 311, no. 5758, pp. 205–208, Jan. 2006.
[72] B. Lambson, D. Carlton, and J. Bokor, “Exploring the thermodynamic limits of computation in integrated systems: Magnetic memory, nanomagnetic logic, and the landauer limit,” *Phys. Rev. Lett.*, vol. 107, p. 010604, 2011.
[73] D. B. Carlton, N. C. Emley, E. Tuchfeld, and J. Bokor, “Simulation studies of nanomagnet-based logic architecture,” *Nano Lett.*, vol. 8, no. 12, pp. 4173–4178, 2008.
[74] M. Kläui, C. a F. Vaz, J. a C. Bland, W. Wernsdorfer, G. Faini, and E. Cambril, “Domain wall pinning and controlled magnetic switching in narrow ferromagnetic ring structures with notches (invited),” *J. Appl. Phys.*, vol. 93, no. 2003, pp. 7885–7890, 2003.
[75] A. Bisig, M. Stärk, M.-A. Mawass, C. Moutafis, J. Rhensius, J. Heidler, F. Büttner, M. Noske, M. Weigand, S. Eisebitt, T. Tyliszczak, B. Van Waeyenberge, H. Stoll, G. Schütz, and M. Kläui, “Correlation between spin structure oscillations and domain wall velocities.,” *Nat. Commun.*, vol. 4, p. 2328, 2013.
[76] J.-G. Zhu, Y. Zheng, and G. A. Prinz, “Ultrahigh density vertical magnetoresistive random access memory (invited),” *J. Appl. Phys.*, vol. 87, no. 9, p. 6668, 2000.
[77] E. Rapoport and G. S. D. Beach, “Dynamics of superparamagnetic microbead transport along magnetic nanotracks by magnetic domain walls,” *Appl. Phys. Lett.*, vol. 100, p. 082401, 2012.
[78] Y. Iwasaki, “Stress-driven magnetization reversal in magnetostrictive films with in-plane magnetocrystalline anisotropy,” *J. Magn. Magn. Mater.*, vol. 240, no. 1–3, pp. 395–397, 2002.
[79] K. Roy, S. Bandyopadhyay, and J. Atulasimha, “Binary switching in a ‘symmetric’ potential landscape.,” *Sci. Rep.*, vol. 3, p. 3038, 2013.
[80] J. Hu, T. Yang, J. Wang, H. Huang, J. Zhang, L. Chen, and C. Nan, “Purely Electric-Field-Driven Perpendicular Magnetization Reversal,” *Nano Lett.*, vol. 15, pp. 616–622, 2015.
[81] X. Li, D. Carka, C. Liang, A. E. Sepulveda, S. M. Keller, P. K. Amiri, G. P. Carman, and

C. S. Lynch, “Strain-mediated 180° perpendicular magnetization switching of a single domain multiferroic structure,” *J. Appl. Phys.*, vol. 118, no. 1, p. 014101, 2015.
[82] C.-Y. Liang, S. M. Keller, A. E. Sepulveda, W.-Y. Sun, J. Cui, C. S. Lynch, and G. P. Carman, “Electrical control of a single magnetoelastic domain structure on a clamped piezoelectric thin film—analysis,” *J. Appl. Phys.*, vol. 116, no. 12, p. 123909, 2014.
[83] R.-C. Peng, J. J. Wang, J.-M. Hu, L.-Q. Chen, and C.-W. Nan, “Electric-field-driven magnetization reversal in square-shaped nanomagnet-based multiferroic heterostructure,” *Appl. Phys. Lett.*, vol. 106, no. 14, p. 142901, 2015.
[84] J. Cui, C.-Y. Liang, E. a. Paisley, A. Sepulveda, J. F. Ihlefeld, G. P. Carman, and C. S. Lynch, “Generation of localized strain in a thin film piezoelectric to control individual magnetoelectric heterostructures,” *Appl. Phys. Lett.*, vol. 107, no. 9, p. 092903, 2015.
[85] C.-Y. Liang, A. E. Sepulveda, D. Hoff, S. M. Keller, and G. P. Carman, “Strain-mediated deterministic control of 360° domain wall motion in magnetoelastic nanorings,” *J. Appl. Phys.*, vol. 118, no. 17, p. 174101, 2015.
[86] J.-M. Hu, T. Yang, K. Momeni, X. Cheng, L. Chen, S. Lei, S. Zhang, S. Trolier-McKinstry, V. Gopalan, G. P. Carman, C.-W. Nan, and L.-Q. Chen, “Fast Magnetic Domain-Wall Motion in a Ring-Shaped Nanowire Driven by a Voltage,” *Nano Lett.*, vol. 16, no. 4, pp. 2341–2348, 2016.
[87] C. A. Ross, S. Haratani, F. J. Castaño, Y. Hao, M. Hwang, M. Shima, J. Y. Cheng, B. Vögeli, M. Farhoud, M. Walsh, and H. I. Smith, “Magnetic behavior of lithographically patterned particle arrays (invited),” *J. Appl. Phys.*, vol. 91, no. 10, p. 6848, 2002.
[88] R. P. Cowburn, D. K. Koltsov, A. O. Adeyeye, and M. E. Welland, “Single-Domain Circular Nanomagnets,” *Phys. Rev. Lett.*, vol. 83, no. 5, pp. 1042–1045, Aug. 1999.
[89] J.-G. Zhu, “Magnetoresistive random access memory: The path to competitiveness and scalability,” *Proc. IEEE*, vol. 96, no. 11, pp. 1786–1798, 2008.
[90] K. Richter, M. Mawass, A. Krone, B. Kruger, M. Weigand, G. Schutz, H. Stoll, and M. Klaeui, “Automotive domain wall propagation in ferromagnetic rings,” *Magnetics Conference (INTERMAG), 2015 IEEE*. p. 1, 2015.